POLITECNICO DI MILANO
Facoltà di Ingegneria Indutriale
Laurea Magistrale in Ingegneria Meccanica

ESTIMATION OF DEPENDANCE OF UPPER LIMB'S BIOMECHANICAL IMPEDANCE ON MUSCULAR ACTIVATION USING INVERSE DYNAMICS

Relatori: Prof. Federico Cheli
Prof. Pierangelo Masarati

Tesi di laurea di:
Andrea Zanoni Matr. 740339

Anno Accademico 2010/2011

ABSTRACT

In this work a biomechanical multibody model of the human upper limb has been developed, aimed at the identification of the passive impedance characteristics of a generic human controller.

The model comprehends 4 rigid bodies, representing the major anatomical elements of the limb, together with 25 viscoelastic, non linear elements that model the muscles fascicula, and accounts for 7 degrees of freedom.

It is thus a cinematically redundant mechanism, and the inversion of its kinematics is an under-constrained problem. However, the solution of this problem is preliminar to the inversion of the dynamics of the system, and thus to the determination of joint torques needed to perform a task, or follow an imposed trajectory.

Both general and specific methodologies have been implemented and developed to solve this indeterminacy.

The system is redundant also upon another aspect: 25 muscles act together to produce 7 components of joint torque, and therefore an optimization algorithm has to be used to identify the single muscle's activation level.

A specific methodology aimed at the determination of the arm intrinsic impedance in *frozen* dynamicsl conditions has also been developed and implemented, and its results analyzed on the basis of experimental data.

A further analysis has been carried out to evaluate the contribution of linear combinations of muscular activations that does not produce a variation in joint torque, but alter the limb's impedance. Such linear combinations has been called Torque Less Activation Modes.

ABSTRACT

Nel presente lavoro di tesi è stato sviluppato un modello multibody biomeccanico dell'arto superiore umano, mirato alla identificazione delle caratteristiche di impedenza passiva di un generico controllore umano.

Il modello comprende 4 corpi rigidi, rappresentanti i maggiori elementi anatomici dell'arto, e 25 elementi viscoelastici non lineari rappresentanti i muscoli, e possiede 7 gradi di libertà.

Risulta quindi un meccanismo cinematicamente ridondante, e l'inversione della sua cinematica risulta un problema sottodeterminato, ma preliminare all'inversione della dinamica e quindi alla determinazione delle coppie di giunto necessarie a garantire una determinata traiettoria imposta.

Metodologie sia generali che specifiche sono state sviluppate per risolvere questa indeterminazione e giungere all'identificazione delle coppie di giunto.

Il sistema è ridondante anche sotto un altro aspetto: 25 gruppi muscolari agiscono insieme per generare 7 componenti di coppia ai giunti: un algoritmo di ottimizzazione deve quindi essere utilizzato per ripartire corretamente le forze ai singoli fasci mucolari.

E' stato inoltre implementata una metodologia specifica per la determinazione dell'impedenza in condizioni di dinamica del sistema *congelata*. I risultati forniti da questa metodologia sono poi analizzati sulla base di dati sperimentali.

All'analisi dei dati è stata aggiunta la valutazione di combinazioni lineari di coefficienti di attivazione che non producono variazione di coppia ai giunti, chiamate Torque Less Activation Modes, per valutare in modo critico e quantitiativo la loro importanza relativa ai fini dell'identificazione dell'impedenza equivalente del braccio del pilota.

TESI - ESTRATTO

INDICE

Tesi - Estratto iii

1 INTRODUZIONE 1
- 1.1 Modellazione del controllore umano 2
- 1.2 Rotorcraft Pilot Coupling 4
- 1.3 Modello multibody del braccio umano 4
- 1.4 Stato dell'arte 7
- 1.5 Vincoli e geometria del modello multibody 9
  - 1.5.1 Vincoli algebrici 11
- 1.6 Modelli di muscolo 14
  - 1.6.1 Strutture e microstrutture dei muscoli schelestrici 14
  - 1.6.2 Proprietà viscoelastiche del tessuto muscolare 16
  - 1.6.3 I modelli di muscolo di Hill 18
  - 1.6.4 Approssimazioni dovute a Zajac 19

2 DINAMICA INVERSA E FORZE MUSCOLARI 25
- 2.1 Inversione della cinematica 25
  - 2.1.1 Meccanismi ridondanti 25
- 2.2 Inversione cinematica completa di un sistema ridondante 26
  - 2.2.1 Posizioni 26
  - 2.2.2 Velocità 27
  - 2.2.3 Accelerazioni 28
- 2.3 Inversione della dinamica e identificazione delle forze muscolari 29
- 2.4 Validazione del modello: dinamica inversa 30
- 2.5 Validazione del modello 30
  - 2.5.1 Massimi momenti articolari 30
  - 2.5.2 Attivazione muscolare 37

3 IMPEDENZA EQUIVALENTE DELL'ARTO SUPERIORE 41
- 3.1 Metodologia 41
- 3.2 Torque - less modes of activation 43
- 3.3 Rotorcraft pilot's arm impedance identification 44
  - 3.3.1 PAO testing at University of Liverpool 44

3.3.2 Effetto dei Torque Less Activation Modes 45
4 CONCLUSIONI E SVILUPPI FUTURI 49
4.1 Sviluppi Futuri 50
BIBLIOGRAFIA 53

ELENCO DELLE FIGURE

Figura 1 Schema generale dei sistemi di riferimento adottati. Nell'epifisi prossimale di ogni osso (o gruppo di ossi, nel caso della mano) è stato posto un sistema di riferimento orientato nel modo mostrato. Non è riportato il sistema di riferimento dell'ulna per motivi di chiarezza grafica. 9

Figura 2 Le miofibrille sono lunghe catene di sarcomeri. Più sotto, schema per la contrazione del singolo sarcomero. In rosso, le molecole di actina, mentre in nero sono rappresentate le molecole di miosina. Quando il sarcomero è attivato, le miosine si piegano all'indietro, causando uno slittamento dei gusci di actina e un accorciamento del sarcomero. 15

Figura 3 Relazione sforzo-deformazione del singolo sarcomero. I punti sono riportati da [13] 17

Figura 4 Relazione forza - velocità di deformazione per il singolo sarcomero. 17

Figura 5 Schema del modello di Hill per la dinamica della contrazione muscolare. La forza muscolare F è prodotta dagli effetti di un elemento contrattile CE, in parallelo con un primo elemento elastico PEE e in serie con un altro elemento elastico SEE, dal momento che la rigidezza dei tendini è generalmente dominante SEE può essere trascurato. 18

Figura 6 Schematizzazione semplificata del modello di Hill utilizzato. L'angolo di pennazione è trascurato come l'elasticità dei cross-bridge. L'elasticità dei muscoli e tendini è inclusa nell'elemento elastico in parallelo PEE. 20

Figura 7 Forza muscolare adimensionalizzata, funzionde della lunghezza adimensionale e della velocità di contrazione adimensionalizzata. 21

Figura 8 Componente attiva della forza nel sarcomero per differenti livelli di attivazione a velocità di contrazione nulla. La curva inferiore corrisponde ad $a = 0.2$ mentre la più alta ad $a = 1$, con passo di 0.2. 22

Figura 9 Componente attiva della forza nel sarcomero per differenti livelli di attivazione. La lunghezza del sarcomero è costante a l_0. La curva inferiore corrisponde a $a = 0.2$ mentre quella più alta ad $a = 1$, con passo 0.2. 22

Figura 10 Massimo momento di abduzione della spalla in condizioni isometriche. Il risultato del modello è messo a confronto con risultati pubblicati da Holzbaur [18], Garner and Pandy [10] e Otis [30]. L'angolo di abduzione è considerato 0° quando il braccio è in posizione di riposo, lungo il corpo, mentre vale 90° quando il braccio è completamente abdotto. 31

Figura 11 Momenti di flessione in condizioni isometriche della spalla calcolati dal modello, a confronto con dati da Holzbaur [18], Garner and Pandy [10] and Otis [30] and Winters [36]. Un angolo di 0° in figura corrisponde alla posizione di braccio disteso lungo il corpo, e un angolo di 90° alla completa flessione 33

Figura 12 Momento di flessione del gomito in condizioni isometriche stimato dal modello, a confronto con dati provenienti da Holzbaur [18], Amis [2] and Buchanan [4]. Un angolo di flessione di 0° corrisponde all'avambraccio completamente esteso, mentre la massima flessione è raggiunta ad un angolo pari a 140° 34

Figura 13 Momento isometrico di supinazione stimato, a confronto con dati da Holzbaur [18] and Garner [10]. Angoli positivi corrispondo ad avambraccio pronato. 35

Figura 14 Momenti massimi in condizioni isometriche di flessione del polso stimati dal modello, a confronto con dati pubblicati da Holzbaur [18] and Delp [6]. Angoli positivi corrispondono a condizioni di estensione del polso. 37
Figura 15 Massimi momenti di deviazione del polso stimati dal modello, messi a confronto con risultati sperimentali e numerici pubblicati da Holzbaur [18] e Delp [6]. Angoli positivi corrispondono alla flessione del gomito. 38
Figura 16 Dati EMG di Huang e altri [20], rilevati in un ciclo di *stepper* 39
Figura 17 Coefficienti di attivazione calcolati dal modello, in una simulazione che ripete l'esperimento di [20]. 40
Figura 18 Storia temporale del comando del collettivo usata per imporre il moto nel modello multibody 44
Figura 19 Parametri di attivazione dei gruppi muscolari della spalla durante la manovra. Sono mostrati solo i gruppi muscolari più attivi. E' facile notare come i gruppi corretti sono effettivamente attivati. 46
Figura 20 Impedenza intrinseca dell'arto superiore, calcolata ogni 5 s a partire da t = 2.5 s 47
Figura 21 Effetto dei modi di attivazione a coppia nulla (TLAM) sull'impedenza equivalente del sistema biomeccanico 48

ELENCO DELLE TABELLE

Tabella 1 Parametri di alcuni muscoli dell'arto superiore. Fonte: [11] 5
Tabella 2 Differenti tipi di articolazioni sinoviali e relative approssimazioni algebriche 11

Tabella 3 Proprietà inerziali del corpi rigidi nel modello.Tutte le masse e i momenti di inerzia comprendono sia il singolo osso che i fasci muscolari ad esso collegati. 13
Tabella 4 Proprietà geometriche del modello. Tutte le dimensioni sono espresse in millimetri e si riferiscono al sistema di riferimento del corpo a sono collegate. 13
Tabella 5 Parametri del modello di muscolo per i fasci muscolari presenti nel modello. Forze massime isometriche e lunghezze di ottimo sono desunte da [18], angoli di pennazione da [23, 18, 24]. 23
Tabella 6 Parametri del modello di muscolo per i fasci muscolari presenti nel modello – continuazione. 24
Tabella 7 Muscoli attivi per l'abduzione e l'adduzione della spalla 32
Tabella 8 Muscoli attivi per la flessione e l'estensione della spalla. 34
Tabella 9 Muscoli attivi per la flessione e l'estensione dell'avambraccio. 35
Tabella 10 Muscoli attivi per la pronazione e la supinazione dell'avambraccio 36
Tabella 11 Muscoli attivi per la flessione e l'estensione del polso 37
Tabella 12 Muscoli attivi per la deviazione del polso. 38

1 INTRODUZIONE

Nella moderna progettazione dei veicoli l'attenzione posta alla modellazione del pilota e più precisamente l'interazione tra il controllo umano e il veicolo è in continuo aumento.
La modellazione matematica del comportamento del pilota e delle sue interazioni con il veicolo, è un'operazione che coinvolge una moltitudine di campi diversi dell'ingegneria che non possono essere, in generale, considerati separatamente.

Pilota e veicolo interagiscono in svariati modi e non è possibile considerarli come sistemi separati, anzi devono essere concepiti come un'unica entità. Il comportamento del veicolo dipende dagli input ricevuti dal pilota, e rispettivamente il pilota è condizionato dallo scambio di reazioni tra lui e il sistema meccanico.

Spesso, l'ultimo tipo di relazioni dipende dagli stimoli percettivi e psicologici del pilota: per es. Il pilota affronterà una manovra con bruschi cambi di direzione a velocità più sostenuta, quando non è soggetto al feedback del veicolo rispetto al caso in cui si trovi in un simulatore in grado di restituire le azioni che provenissero dal veicolo durante una manovra reale [35].

In alcuni casi, però, è osservabile un'interazione più puramente meccanica: le vibrazioni della struttura del veicolo possono agire sul pilota in maniera tale da provocare azioni involontarie, determinate dalla risposta meccanica del corpo del pilota. Entrambe le azioni biomeccaniche, attive e passive, del corpo umano, in particolare del braccio del pilota, giocano un ruolo fondamentale nel manifestarsi di oscillazioni auto-sostenute che possono creare condizioni pericolose in differenti interazioni uomo-macchina.

Nel campo dei veicoli terrestri, la più forte interazione tra uomo e veicolo si trova nel controllo di veicoli a due ruote, dove l'inerzia e l'impedenza meccanica del pilota contribuiscono notevolmente al comportamento dinamico del sistema accoppiato in termini di stabilità. Per esempio, l'azione del pilota sul manubrio può significativamente alterare la frequenza associata al modo di vibrare wobble [32].

1.1 MODELLAZIONE DEL CONTROLLORE UMANO

I processi di modellazione dei veicoli terrestri, velivoli ed elicotteri sono diventati sempre più sofisticati mentre, allo stesso tempo, la tendenza dei costruttori è di eliminare o ridurre, ove possibile, la necessità di effettuare sperimentazioni dirette su prototipi, per diminuire i costi di produzione. Da questa tendenza deriva il forte aumento, negli ultimi anni, dell'utilizzo di modellazioni numeriche del pilota.

MacAdams ha proposto nel 2003 [25] ha sintetizzato le caratteristiche che un modello per un conducente di autoveicolo, che con alcune modifiche minori, può essere generalizzato per ogni tipo di controllore umano.

1. modellazione corretta del ritardo di fase
2. capacità di prevedere le azioni di controllo necessarie nei prossimi istanti di tempo
3. capacità di adattamento in relazione alla dinamica del veicolo controllato e alle condizioni operative
4. esibizione di un modello lineare di tipo crossover nelle immediate vicinanze della frequenza di crossover
5. presenza di un modello di veicolo o similare all'interno del modello di pilota, per essere in grado di prevedere le reazioni del veicolo controllato nei successivi istanti di tempo
6. capacità di modificare e pianificare la traiettoria futura
7. capacità di modificare e pianificare la traiettoria in modo differente al variare delle caratteristiche di abilità
8. modellazione del processo neurologico che trasforma gli input cognitivi in output di controllo
9. effetto di filtraggio da parte del sistema neuromuscolare degli output

La modellazione del pilota, in particolare nel settore dei veicoli terrestri, si è concentrata principalmente sui primi sei punti, soprattutto a causa delle vibrazioni dalla struttura del veicolo meno soggette a produrre

una reazione, da parte di strutture del pilota, abbastanza significative da essere ritrasferite attraverso i comandi, perché l'amplificazione dell'azione del pilota è minore rispetto a quanto succeda in campo aeronautico.

Inoltre, le frequenze associate alla dinamica del propulsore e alle vibrazioni strutturali della cassa di un veicolo terrestre sono generalmente fuori dal campo interessato dalla risposta biomeccanica. Non considerando i veicoli dedicati all'uso agonistico, le reazioni a causa del moto rigido del telaio consentito dal sistema di sospensione non sono termini rilevanti per la vibrazione del corpo del conducente.

Grandi sforzi sono riposti nel determinare quali siano gli input che il cervello umano seleziona in quanto più significativi, e quali siano le tecniche di controllo che possono meglio approssimare le trasformazioni a cui questi parametri sono soggetti prima di divenire segnali neurali, con quali ritardi essi vengono inviati, quali siano le componenti in frequenza rilevanti e quali i limiti posti ai segnali stessi.

Nonostante ciò è diventato fondamentale,in vari aspetti, nell'ambito della progettazione di veicoli essere in grado di modellare in modo efficace e sufficientemente preciso le forze che il controllore umano è in grado di applicare al sistema meccanico con il quale interagisce. Chiari esempi sono l'ergonomia e il design della postazione di controllo, specialmente se progettati per conducenti diversamente abili.

Un altro interessante esempio è rappresentato dal APC (Aircraft Pilot Coupling) e dal RPC (Rotorcraft Pilot Coupling). I due fenomeni sono relazionati l'uno all'altro in quanto il comportamento di vibrazione aeroelastica degli aeromobili interagisce con le caratteristiche biomeccaniche del pilota e produce vibrazioni indesiderate, involontarie e possibili oscillazioni auto-sostenute del sistema uomo-velivolo.

In campo elicotteristico i fenomeni RPC rappresentano un caso critico per la sicurezza in volo e i test hanno evidenziato i problemi sopra indicati in quanto le frequenze relative al motore e alle dinamiche della trasmissione (primo modo torsionale), la dinamica del sistema di controllo del volo, le rigidezze del rotore e la dinamica del telaio, sono tutte nel campo di risposta biomeccanica del pilota.

1.2 ROTORCRAFT PILOT COUPLING

I moderni sistemi di controllo del volo, in alcuni casi, possono portare a inaspettate e inattese oscillazioni o divergenze dinamiche tra pilota e sistema elicottero che causano pericolosi, a volte disastrosi, incidenti [28, 15, 3]. Sono noti due tipi di instabilità in cui il pilota può essere causa o partecipante:

- PIO: Pilot - Induced Oscillations
- PAO: Pilot - Assisted Oscillations

Nel primo caso di oscillazioni si manifestano quando il pilota introduce un ritardo di fase o muove i comandi nella direzione sbagliata, ma non influiscono sulla sicurezza del volo. É necessaria una partecipazione attiva del pilota nell'anello di controllo: se egli rilasca i comandi o modifica le sue azioni di controllo le oscillazioni cessano.

Nel secondo caso, sono il risultato involontario del pilota nell'anello di controllo e sono strettamente relazionate alla biomeccanica, biodinamica, tipo di corporatura, esperienze e caratteristiche neuromuscolari dello stesso [26, 14].

Convenzionalmente l'approccio per la modellazione di questo tipo di risposte è la misurazione degli spostamenti dei controlli mentre il pilota è soggetto a vibrazioni note, imposte attraverso un tavolo vibrante o un dispositivo similare, per ricostruire la sua funzione di trasferimento e le sue caratteristiche di impedenza meccanica.

Un modo più sofisticato è quello di misurare il comportamento del pilota all'interno di un simulatore di volo. Ovviamente, questo approccio ha molti limiti: i più importanti derivano dal fatto che le funzioni di trasferimento che si ottengono dipendono in modo sostanziale dalla geometria dei comandi e dalle proprietà dinamiche e non sono adatte all'estrapolazione.

1.3 MODELLO MULTIBODY DEL BRACCIO UMANO

Le limitazioni che possono essere attribuite tramite le funzioni di trasferimento delle caratteristiche biomeccaniche umane derivano da una grande variabilità dei parametri da cui dipendono

Tabella 1: Parametri di alcuni muscoli dell'arto superiore. Fonte: [11]

Muscoli	G&P[a] (2003)	Wood (1989)	Veeger (1991)	Bassett (1990)	Winters (1988)	An (1981)	Veeger (1997)
Volume [cm^3]							
Tricipite	619.99	298.24	99.70	152.00	283.02	152.60	397.00
Bicipite	365.84	108.15	111.20	128.00	113.21	64.20	128.00
Physiological Cross Section Area (PCSA) [cm^2]							
Tricipite	76.30	11.40	6.84	4.61	–	18.80	13.81
Bicipite	25.90	3.39	6.29	4.80	–	4.60	5.34

a Garner & Pandy

- la corporatura del pilota (altezza e peso)
- rapporto tra dimensioni del pilota e geometria dei comandi
- attitudini soggettive
- obiettivo della missione
- carico di lavoro a cui è soggetto il pilota

Considerando che la capacità di generazione di forza del corpo umano è fortemente dipendente dalle caratteristiche dell'ambiente in cui opera, i parametri dei test non possono essere estesi al di fuori del dominio in cui sono stati generati. Qui, 'configurazione ambientale' è intesa in senso molto ampio: può essere la disposizione geometrica dei controlli e della cabina di guida rispetto alla posizione del pilota, le caratteristiche di feedback dei controlli, il comportamento di vibrazione della struttura, etc.

In secondo luogo, la varianza dei parametri biomeccanici associati ai differenti individui si riflette sulla variabilità della funzione di trasferimento. Nella tabella 1 sono mostrati i risultati di un lavoro pubblicato in [11]. Parametri relativi ai fasci muscolari dell'arto superiore pubblicati in letteratura e stimati da Garner e Pandy sono messi a confronto.

Esaminando i dati, è evidente, come questi parametri possono variare in modo importante da un individuo ad un altro. Ogni tentativo di generalizzazione di questo approccio basato sulla risposta in frequenza

di un campione necessariamente limitato di individui, deve fare i conti con questa variabilità, tale da provocare scarsa correlazione dei dati [19].

L'approccio multibody si presenta come un'alternativa valida a questo tipo di ricerca, offrendo una potente e flessibile modalità di analisi. Utilizzando un'analisi multibody è possibile , e in modo semplice, descrivere le specifiche proprietà delle geometrie, delle vibrazioni, delle risposte e, in linea di principio, anche delle caratteristiche biomeccaniche del pilota.

Nella fase di progettazione, quando differenti configurazioni delle strutture del veicolo con varie disposizioni e dinamiche di controllo sono valutate e testate, la possibilità di ottenere un buon risultato senza investire molte risorse e tempo in specifici test è un obiettivo che ogni produttore vorrebbe ottenere. Questo può essere raggiunto devolvendo ad una simulazione numerica una vasta gamma di test preliminari e lasciando a un prototipo fisico il compito di validazione un ristretto numero di risultati.

La modellazione multibody offre un ulteriore vantaggio, in quanto ha la possibilità di riprodurre una serie completa di quantità fisiche legate alla dinamica del sistema esaminato, proprietà che la distingue in modo marcato dai test sperimentali in cui, per ovvie ragioni, la raccolta di dati è limitata pochi segnali rappresentativi e pre-determinati.
Pertanto con una simulazione multibody è generalmente possibile ottenere una migliore compressione del comportamento fisico dei sistemi interessati.

La scelta di concentrarsi sulla modellazione del braccio è giustificata dal fatto che l'arto superiore rappresenta l'elemento più complesso del corpo umano ed è attivamente coinvolto nella generazione di un input di controllo se al controllore viene considerato parte passiva nell'anello di controllo, nel caso attivo l'elemento principale è il sistema neurologico. Mentre il resto del corpo può essere ben approssimato da un singolo elemento a parametri concentrati, il braccio necessita di una trattazione separata; in quanto esso può modificare la sua configurazione geometrica e dinamica in maniera superiore al resto del corpo.

1.4 STATO DELL'ARTE

Ad oggi, sono stati fatti diversi tentativi di modellare l'arto superiore attraverso tecniche multibody, soprattutto per intenti puramente biomeccanici, atti a riprodurre informazioni accurate da un punto di vista fisiologico e medico [22, 1, 33, 23]. Il livello di dettaglio richiesto è ottenuto attraverso una dettagliata descrizione di ogni giunto articolare, a volte modellato con elementi elastici e con asse di rotazione migrante [12], un set esteso di elementi rappresentanti il comportamento dei muscoli, con dinamiche di attivazione indipendenti, e sono generalmente modelli atti all'inversione dinamica e alla ricostruzione delle dinamiche di attivazione, mediante l'imposizione della cinematica di ogni giunto, spesso acquisita da prove sperimentali.

La modellazione multibody del corpo è applicata soprattutto nel settore dei veicoli terrestri volta allo studio del confort del pilota. I modelli umani tendono ad essere descritti con elementi a parametri concentrati, in quanto non comprendono la modellazione dei singoli muscoli ma solo elementi che rappresentano l'impedenza meccanica della corrispondente parte del corpo (es. l'avambraccio).

Nel campo dell'ingegneria aeronautica sono stati fatti diversi studi per modellare le proprietà biomeccaniche dell'accoppiamento dinamico pilota-aeromobile e pilota-elicottero [19, 14, 34]. In molti casi, attraverso un equivalente meccanico del corpo umano, utilizzando parametri ottenuti in modo statico o con specifici test sono state definite specifiche funzioni di trasferimento lineari. Una generica procedura, mirata ad ottenere informazioni sull'impedenza meccanica da principi primi, senza necessariamente fare riferimento ad una condizione specifica, è stata delineata in [7], sviluppata nell'ambito dell'organizzazione *GARTEUR*[1].

Un modello numerico dell'arto superiore è stato usato per per calcolare le dinamiche di attivazione corrispondenti ad un movimento imposto della mano, e l'impedenza di ogni articolazione è stimata in termini di relazione fra coppia di giunto e movimento del giunto stesso.

Due tipi di ridondanza aumentano le dimensioni del problema: il primo collegato alla cinematica in quanto il braccio umano è generalmente considerato un sistema a 7 gradi di libertà e alla mano possono essere imposti un massimo di 6 gradi di libertà.

1 Group for Aeronautical Research and Tecnology in EURope: www.garteur.eu

Il secondo relativo alla generazione della coppia di giunto: dato che i fasci muscolari non sono in grado di generare forze di compressione, essi possono generare coppia attorno ad un giunto solo lavorando in coppie antagoniste; inoltre generalmente sono attivati più di una coppia per volta per produrre momento sullo stesso asse rendendo così il sistema ulteriormente ridondante.

La procedura seguita può essere delineata in quattro fasi

1. cinemantica inversa, necessaria per stimare i movimenti dei giunti articolari dovuti a movimenti imposti alla mano, considerata alla stregua dell'end-effector di un robot manipolatore

2. dinamica inversa mirata al calcolo della coppia di giunti

3. ottimizzazione della procedura applicata per l'attivazione dei muscoli, per il ritrovamento delle forze muscolari che sono in grado di generare le coppie richieste

4. calcolo dei parametri di impendenza di ogni singola articolazione

I punti 1 e 3 necessitano di un algoritmo per risolvere le ridondanze, o una forma di chiusura, per essere portati a compimento. Il lavoro presentato in questa tesi prende le origini da questo approccio, rappresentando la sua implementazione e il suo ulteriore sviluppo.

Deve essere sottolinato, tuttavia, che a causa delle sopracitate fonti di variabilità, il metodo proposto non pretende di definire deterministicamente la relazione pilota-veicolo, o la funzione di trasferimento biomeccanica del pilota, ma mira a diventare uno strumento di verifica e valutazione delle cause legate a questa variabilità.

Attraverso questa procedura, viene ricercata una stima della importanza relativa delle cause di scarsa correlazione fra i dati correntemente riscontrata, per rendere possibile la specializzazione della ricerca sui parametri che possono essere identificati come più problematici. Una migliore comprensione dei fenomeni coinvolti nella interazione uomo veicolo o, più in generale, uomo-macchina, è inoltre una delle motivazioni più importanti che hanno spinto a intraprendere l'implementazione di questa procedura.

1.5 VINCOLI E GEOMETRIA DEL MODELLO MULTIBODY

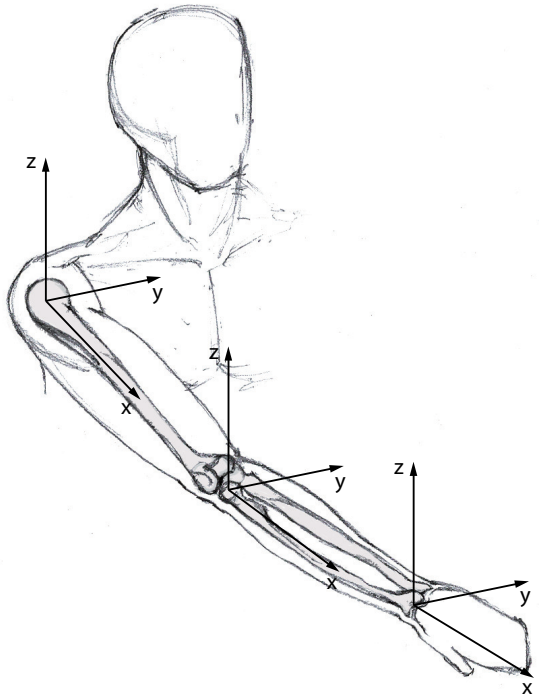

Figura 1: Schema generale dei sistemi di riferimento adottati. Nell'epifisi prossimale di ogni osso (o gruppo di ossi, nel caso della mano) è stato posto un sistema di riferimento orientato nel modo mostrato. Non è riportato il sistema di riferimento dell'ulna per motivi di chiarezza grafica.

Tradurre la struttura anatomica e le sue relazioni sopra descritte in un modello multibody è un processo che, per sua natura, non offre un'unica soluzione. Il livello di dettaglio, come in un generico modello matematico di un sistema fisico, dipende dalla precisione desiderata, dagli aspetti fisici del sistema che si ritengono importanti per il fenomeno investigato.

Nel caso presentato, l'oggetto della simulazione è riprodurre il comportamento passivo del braccio umano rispetto alla generazione di impedenza meccanica in mansioni di manipolazione, in cui tipicamente

la mano è in una configurazione in cui afferra un comando. (per es. le leve del controllo ciclico o collettivo in un elicottero, il manubrio nel caso di una motocicletta, ect.)

É da sottolineare che che la riproduzione molto precisa del movimento dell'apparato scheletrico dell'arto superiore non è richiesta, quindi l'assunzione che durante il movimento di prono-supinazione l'ulna sia fissa e il radio ruoti attorno ad essa, è giustificata. Inoltre, movimenti che richiedono un'importante pronazione o supinazione della mano sono generalmente di poca importanza nel controllo di un veicolo o di un elicottero.

Un'altra semplificazione che è possibile fare, in luce a quanto detto in precedenza, consiste nel trascurare le azioni interne della mano mirate al controllo del movimento delle dita, e perciò considerare la mano un solo corpo rigido. Per questa ragione la mano è considerata come un unico corpo rigido.

Anche il moto del complesso della spalla è trascurato, in quanto la spalla stessa e il busto sono assunti in posizione di riposo durante le simulazioni effettuate, per assicurare che il modello rimanga, in questa fase preliminare, il più semplice possibile.

Nella figura 1 è rappresentata la localizzazione dei nodi usati per il modello cinematico dell'arto superiore sovrapposti allo scheletro. Ogni osso con i muscoli relativi è considerato un corpo rigido, i giunti sono applicati ai condili. La lunghezza che può essere intesa come la distanza tra il condilo, di un generico osso, lungo il suo *asse meccanico*, ovvero l'asse che connete i baricentri dei condili stessi.

Il modello comprende 4 corpi rigidi: l'omero, l'ulna, il radio e la mano. Ogni sistema di riferimento di ogni singolo osso è situato nel baricentro del condilo prossimale con l'asse x lungo l'asse meccanico del osso, l'asse y diretto verso il piano mediale e l'asse z diretto superiormente per formare un sistema di riferimento destrorso.

Dal momento che nel modello sono presenti quattro nodi, aventi 6 gradi di libertà ciascuno, un totale di 24 gradi di libertà devono essere considerati. Per ragioni pratiche un quinto nodo, fisso, è usato per modellare il sistema di riferimento globale.

Tabella 2: Differenti tipi di articolazioni sinoviali e relative approssimazioni algebriche

Articolazione sinoviale	Vincolo algebrici	Esempio
artrodia	giunto di complanarità	articolazione acromioclavicolare
trocoide	giunto cilindrico	articolzione radioulnare prossimale
ginglimo	giunto di rivoluzione	articolazione omeroulnare
enartrosi	giunto sferico	articolazione gleno-omerale
condiloartrosi	giunto Cardanico	articolazione radiocarpale
a sella	giunto Cardanico	articolazione sternoclavicolare

1.5.1 *Vincoli algebrici*

Le articolazioni sinoviali possono essere approssimate con un equivalente vincolo algebrico. Nella Tabella 2 si visualizzano i differenti tipi di giunti sinoviali e i vincoli algebrici ad essi correlati.

Risulta così evidente che la modellazione di un giunto con vincoli algebrici diviene sensata solo se non è richiesta è un'accurata riproduzione dei movimenti dei giunti, per la ragione che l'articolazione reale presenta una vasta gamma si caratteristiche che la rendono difficile da modellare precisamente [5, 29, 8].

Praticamente tutti i giunti che richiedono una rotazione nella quale prendono parte le ossa, l'asse (o gli assi) di rotazione non è (sono) fisso e raramente è (sono) perfettamente ortogonale all'asse meccanico dell'osso relativo.

Ciononostante, la migrazione degli assi e il corretto vincolo geometrico non sono praticamente mai implementate in un modello multibody che non mira a una estrema precisione nel ricostruire il moto di un arto superiore (con qualche eccezione, vedi [12]) da questo approccio ne derivano due svantaggi: il modello risulta meno maneggevole ed efficiente e ancora più importante sarebbe estremamente specifico per il soggetto modellato. Tenendo presente la possibilità di estendere il modello e di generalizzarlo il più possibile è una priorità utilizzare dei vincoli algebrici ideali.

Il complesso della spalla può essere rappresentato da un giunto sferico, situato nel centro del condilo prossimale dell'omero e nel centro della fossa glenoidea. Avendo trascurato il movimento della spalla, il

giunto sferico con l'omero è vincolato a terra.

Al capo distale dell'omero, due giunti lo connettono con il radio e l'ulna: l'articolazione omeroulnare è approssimata da un giunto di rivoluzione, che permette solo la rotazione dell'ulna rispetto all'omero sull'asse y, centrato nella troclea. Il giunto omeroulnare è modellato come un giunto sferico, vincolato al centro del capitulum corrispondente ad un punto leggermente all'esterno della terminazione prossimale del radio. Per lo scopo di questo studio è stato identificato con la terminazione prossimale del corpo rigido che rappresenta il radio.

Il giunto radioulnare, prossimale e distale, può essere semplificato e condensato in un singolo elemento guida tra il punto P e l'asse meccanico dell'ulna. Il punto P ha un offset dal radio in direzione y tale per cui i due ossi nella posizione di riposo della fig. 1 sono mantenuti paralleli l'uno all'altro.

Per riassumere:

- i giunti sferici eliminano 3 gradi di libertà ciascuno
- I giunti di rivoluzione eliminano 5 gradi di libertà
- il giunto guida elimina 2 gradi di libertà
- i giunti Cardanici eliminano 4 gradi di libertà

Quindi il sistema aveva $24–17 = 7$ gradi di libertà. Quando tutti i movimenti dei 6 gradi di libertà della mano sono prescritti, l'arto superiore ha 1 grado di libertà ridondante.

Nella Tabella 3 sono visualizzate le proprietà inerziali che vengono attribuite ai corpi rigidi associati all'omero, radio, ulna e mano condensando il contributo delle ossa e dei muscoli.

Un'altra importante quantità geometrica è presentata nella Tabella 4. Tutte le lunghezze delle sezioni delle ossa sono parametrizzate rispetto alla loro lunghezza. In tabella sono rispettati i valori di riferimento dell'omero, radio ed ulna, mano rispettivamente di 300 mm, 250 mm e 100 mm.

ll modello è completato dagli elementi che rappresentano i muscoli, usando elementi viscoelastici, monodimensionali, che possono esercitare una forza tra i loro punti di attacco proporzionale al loro stato di deformazione e al loro livello di attivazione.

Tabella 3: Proprietà inerziali del corpi rigidi nel modello.Tutte le masse e i momenti di inerzia comprendono sia il singolo osso che i fasci muscolari ad esso collegati.

Corpo rigido	Massa [kg]	J_{xx} [kg mm^2]	J_{yy} [kg mm^2]	J_{zz} [kg mm^2]
Omero	1.89	1890	14592	14592
Radio	0.498	540	3122	3122
Ulna	0.752	300	4170	4170
Mano	0.81	2200	3769	3769

E' quindi essenziale esaminare attentamente il comportamento viscoelastico dei muscoli, per attribuire una legge costitutiva sufficientemente precisa agli elementi monodimensionali che connettono i loro punti di attacco nel modello.

Tabella 4: Proprietà geometriche del modello. Tutte le dimensioni sono espresse in millimetri e si riferiscono al sistema di riferimento del corpo a sono collegate.

Body	Pos. epicondilo prossimale			Pos. epicondilo distale		
	x	y	z	x	y	z
Omero	0	0	0	300	0	0
Radio	0	-16	0	250	-16	0
Ulna	0	16	0	250	16	0
Mano	0	-16	0	100	-16	0

Body	Posizione del baricentro		
	x	y	z
Omero	150	0	0
Radio	159	0	0
Ulna	78	0	0
Mano	51	0	0

1.6 MODELLI DI MUSCOLO

Ogni azione eseguita dal corpo umano è resa possibile dal tessuto muscolare.

Nel corpo umano sono presenti tre tipi di muscoli: *scheletrico*, *cardiaco* e *liscio*. Questi ultimi che rivestono gli organi interni cavi sono involontari e operano tutte le azioni meccaniche involontarie e sono caratterizzati da una struttura profondamente diversa da quella degli altri due tipi. I muscoli cardiaci e scheletrici hanno la stessa struttura microscopica e fisiologia, ma differiscono per la natura volontaria della loro attivazione: mentre i muscoli cardiaci sono ovviamente, involontari, i muscoli scheletrici possono essere attivati con stimoli volontari. Essi forniscono l'intermedium tra il movimento articolare desiderato e la sua realizzazione.

I muscoli scheletrici non sono elementi lineari, ma viscoelastici che possono essere contratti su attivazione volontaria: quando un segnale nervoso agisce su di essi possono esercitare una forza trasmessa dai tendini, tra i loro punti di attacco. Sono asimmetrici e possono produrre forze di trazione mentre non rispondono a compressione.

Di conseguenza possono produrre movimenti di giunti articolari in due direzioni, solitamente lavorando in gruppi, il più semplice dei quali è rappresentato da una coppia di muscoli antagonisti, agenti nel fornire coppia nei due versi rispetto al giunto. Abbastanza comunemente, gruppi muscolari costituiti da più di due fasci agiscono per lo stesso movimento in parallelo come nel caso dei bicipiti, tricipiti e quadricipiti.

1.6.1 *Strutture e microstrutture dei muscoli schelestrici*

I muscoli scheletrici e cardiaci sono anche indicati come muscoli *striati*, presentano una serie di piccole unità di contrazione attivate dagli stimoli elettrici del sistema nervoso.

L'unità contrattile di base è chiamata *sarcomero*, una struttura composta da lunghe fibre proteiche che possono scorrere una sull'altra sotto attivazione. Strutture composte da *miosina* si interpongono ai lunghi filamenti di *actina* che disposte in modo da formare una rete e maglie esagonali, completano il fascio muscolare che si collega all'estremità del sarcomero.

Il sarcomero rappresenta l'unità contrattile di base dei muscoli ma da

solo non può esercitare alcuna forza, è necessario che sia guidato da uno stimolo. A questa funzione provvede uno speciale tipo di fibra nervosa (o *assone*) che congiunge l'azione neurale con un limitato insieme di fibre muscolari. L'unità motrice di base (Motor Unit, MU) è una struttura formata da fasci di assoni che controllano le fibre.

Allargando la visione della struttura, è possibile riconoscere che l'insieme dei sarcomeri costituiscono *miofibrilla* della quale sono composte le *fibre muscolari*, che a loro volta organizzate in *fasci* formano l'intero muscolo.

I muscoli sono connessi ai giunti articolari o alle ossa in generale, attraverso i tendini che costituiscono una connessione rigida.

Il processo di contrazione è visualizzato in Figura 2. Quando il sarcomero viene stimolato, le protuberanze della miosina chiamate *cross-bridges* che sono connesse con i filamenti della actina, si piegano verso il centro del sarcomero, creando un effettivo slittamento rispetto alla miosina e causando un accorciamento dell'intera struttura.

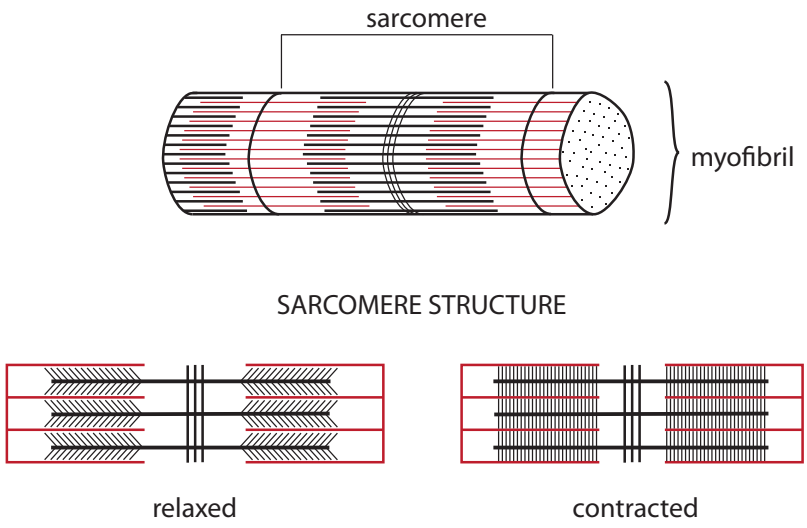

Figura 2: Le miofibrille sono lunghe catene di sarcomeri. Più sotto, schema per la contrazione del singolo sarcomero. In rosso, le molecole di actina, mentre in nero sono rappresentate le molecole di miosina. Quando il sarcomero è attivato, le miosine si piegano all'indietro, causando uno slittamento dei gusci di actina e un accorciamento del sarcomero.

1.6.2 *Proprietà viscoelastiche del tessuto muscolare*

Le proprietà generali del muscolo derivano dalle caratteristiche dei singolo sarcomeri, considerando che I test sui singolo sarcomeri o sulla singola unità motrice, sono impraticabili, sono spesso effettuati test sull'intero muscolo [13, 24] in-vitro o in soggetti vivi umani e animali.

La forza generata dai sarcomeri dipende strettamente dal grado di sovrapposizione delle proteine di miosina e actina e così dal grado di sforzo della fibra muscolare. Il parametro più comunemente usato è quello di indicare la forza assiale del sarcomero come lunghezza adimensionale.

$$x = \frac{l}{l_o} \tag{1.1}$$

al posto della deformazione normalmente intesa

$$\epsilon = \frac{l - l_o}{l_o} \tag{1.2}$$

Se la fibra o il muscolo sono tenuti ad una lunghezza costante e attivata, si ottengono condizioni di *contrazione isometrica* e dopo un breve transitorio il muscolo produce la sua forza di contrazione isometrica. Variando la lunghezza della fibra e ripetendo l'esperimento fino al raggiungere la massima forza è possibile identificare il picco di forza isometrica F_o e la lunghezza della fibra corrispondente chiamata lunghezza ottimale l_o.

La Figura 3 mostra il rapporto forza-lunghezza per un generico sarcomero, contrapposti ai dati provenienti dall'esperimento di [13]. Le curve presentano tre distinte regioni

- un'iniziale regione ascendente da 0.2 a 0.4 l_o
- un plateau tra 0.8 e 1.1 l_o
- un regione discendete che si riporta a zero la forza intorno a 1.6 l_o

Le regioni ascendenti e discendenti della curva possono essere approssimate con delle funzioni esponenziali e presentano un certo grado di simmetria.

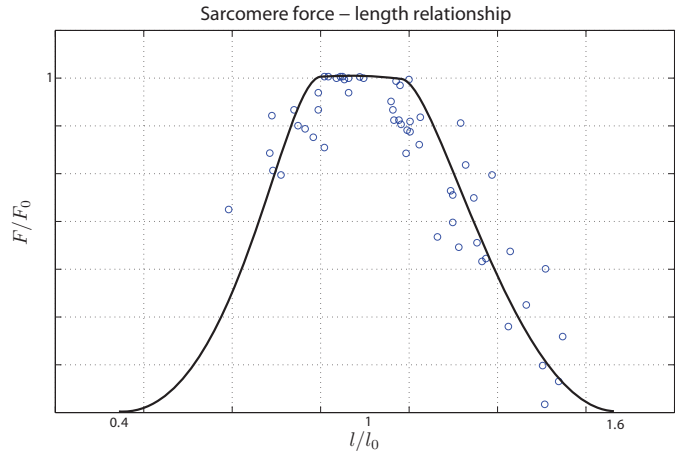

Figura 3: Relazione sforzo-deformazione del singolo sarcomero. I punti sono riportati da [13]

La forza muscolare inoltre mostra una stretta correlazione non lineare con la velocità di contrazione che è la definita come la derivata della lunghezza istantanea del muscolo cambiata di segno.

$$V = -\dot{l} \tag{1.3}$$

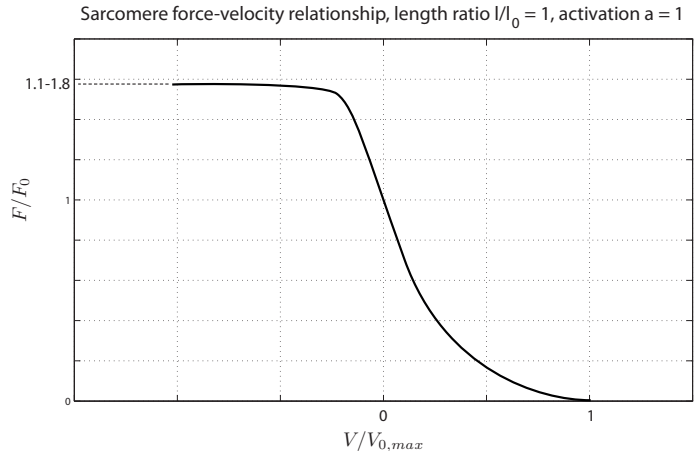

Figura 4: Relazione forza - velocità di deformazione per il singolo sarcomero.

Iniziando da una condizione isometrica e rilasciando la fibra mentre il valore di forza scambiata tra il vincolo e la fibra stessa viene misurata

è possibile determinare la relazione forza-velocità. (Figure 4).

A $V = 0$, $x = 1$ and $a = 1$ il picco di forza isometrica è raggiunta come visto in precedenza. Quando $V < 0$ quindi la fibra si sta accorciando, produce una forza maggiore, fino approssimativamente 1.6 F_0, mentre mostra una diminuzione della forza prodotto in condizioni di allungamento progressivamente più rapido. Una massima velocità di allungamento $V_{0,max}$, è raggiunta nel momento in cui la fibra non produce più nessuna forza.

Diversi modelli sono stati sviluppati per condensare le caratteristiche viscoelastiche dei muscoli senza il bisogno di modellare la singola unità motrice.

1.6.3 *I modelli di muscolo di Hill*

Il modello più utilizzato per la descrizione della dinamica della contrazione dei muscoli è bastato sul lavoro di Archibald Vivian Hill, che propose la prima versione del modello nel 1938.

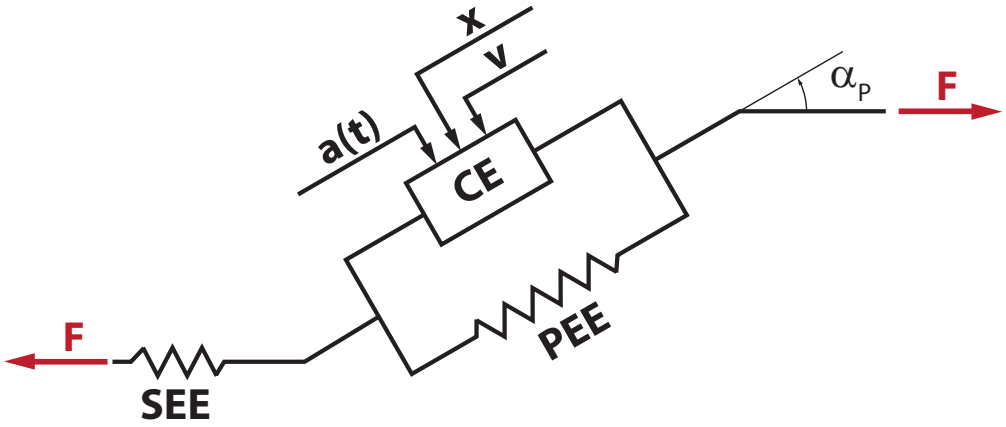

Figura 5: Schema del modello di Hill per la dinamica della contrazione muscolare. La forza muscolare F è prodotta dagli effetti di un elemento contrattile CE, in parallelo con un primo elemento elastico PEE e in serie con un altro elemento elastico SEE, dal momento che la rigidezza dei tendini è generalmente dominante SEE può essere trascurato.

La Figura 5 mostra schematicamente il modello nella sua forma originale. L'*elemento contrattile* CE è responsabile della generazione della

componente attiva della forza del muscolo, agendo sia come attuatore che con un comportamento elastico. Di conseguenza la forza generata nel CE è in funzione della lunghezza dimensionale del muscolo , la velocità di contrazione V oltre che ai parametri di attivazione $a(t)$.

L'angolo α rappresenta *l'angolo di pennazione* del muscolo, cioè l'angolo che le fibre del muscolo formano con l'asse del tendine, è generalmente acuto e contenuto, la sua variazione durante il moto può essere tralasciata tranne che nei muscoli con tendini molto corti.

Le proprietà elastiche dei tendini sono introdotte per mezzo di un *elemento elastico in parallelo* PEE, a volte chiamato *elemento passivo*. Un *elemento elastico serie* SEE è considerato a volte , per separare l'energia elastica muscolare immagazzinata nei cross-bridge (presumibilmente nella *titina*) da quella immagazzinata nei tendini.

Siccome la prima è generalmente irrilevante rispetto alla seconda, è possibile omettere il SEE almeno con muscoli con tendini corti rispetto alla propria lunghezza [11].
Omettendo i SEE porta all'eliminazione di alcuni comportamenti incompatibili con l'ipotesi che i sarcomi agiscano all'unisono e le proprietà delle fibre sia una diretta conseguenza delle proprietà degli stessi sarcomi.

$$L_m = \gamma \cdot L_s \tag{1.4}$$

dove L_s è la lunghezza del sarcomero e γ il numero totale dei sarcomeri nella fibra muscolare. In questo caso, dunque, la legge costitutiva di una fibra non sarebbe la somma delle singole leggi costitutive dei sarcomeri [37].

1.6.4 *Approssimazioni dovute a Zajac*

Nel lavoro che divenne fondamentale per la modellazione dei muscoli [37], Zajac propose alcune semplificazioni adatte alla simulazione della dinamica muscolare in casi in cui diversi gruppi muscolari concorrono alla generazione delle coppie di giunto e quindi al moto dei giunti stessi.

Le sue assunzioni possono essere condensate come:

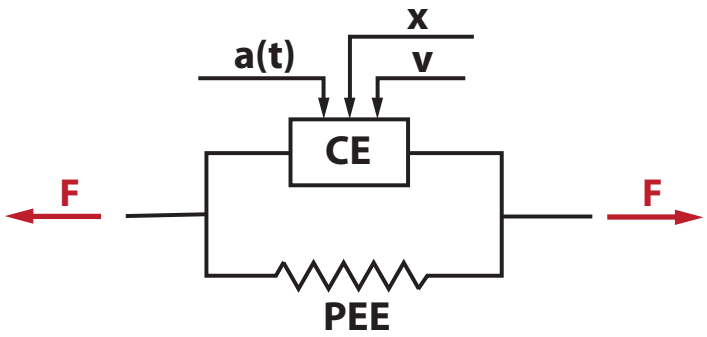

Figura 6: Schematizzazione semplificata del modello di Hill utilizzato. L'angolo di pennazione è trascurato come l'elasticità dei cross-bridge. L'elasticità dei muscoli e tendini è inclusa nell'elemento elastico in parallelo PEE.

1. la forma della curve forza-lunghezza è la stessa per tutti i muscoli e non cambia con l'attivazione
2. i muscoli SEE quando associati con cross-bridge rigidi possono essere trascurati completamente. L'elasticità dei muscoli può essere associata all'elasticità nei singoli PEE
3. il punto in cui la curva forza-velocità intercetta l'asse delle ascisse è indipendente dall'attivazione
4. la variazione dell'angolo di pennazione è rilevante solo per muscoli con tendini corti rispetto alla lunghezza e può essere tralasciato quando è minore di 15-20°.

Queste considerazioni hanno portato Pennestrì ed altri nell'adattamento del modello di Hill [31], adeguato per la simulazione biomeccanica di un arto superiore, il quale condensa le proprietà elastiche passive dei tendini e dei muscoli nei PEE e il comportamento di contrazione nei CE in parallelo alla forma. I parametri dei 25 muscoli presenti sono raccolti nella Tabella 5 e 6. La variabilità dell'angolo di pennazione è trascurabile in quanto è molto piccolo per tutti i muscoli coinvolti. La schematizzazione del modello è rappresentata nella Figura 6.

La forza dei muscoli è definita come

$$F_m = F_a + F_p = F_o \left(f_1 f_2 a(t) + f_3 \right) \tag{1.5}$$

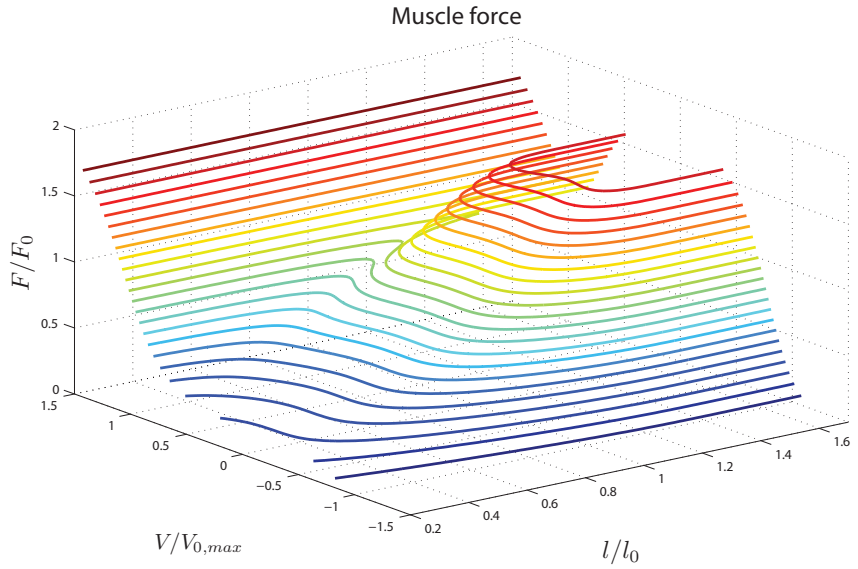

Figura 7: Forza muscolare adimensionalizzata, funzionde della lunghezza adimensionale e della velocità di contrazione adimensionalizzata.

La relazione forza-lunghezza per i comportamenti passivi

$$f_3 = 1.3 \cdot \arctan\left(0.1(x - 0.22)^{10}\right) \tag{1.6}$$

mente per componenti CE attivi

$$f_1 = e^{\left(-40(x-0.95)^4 + (x-0.95)^2\right)} \tag{1.7}$$

La relazione forza-velocità è

$$f_2 = 1.6 - 1.6e^{\left(-\frac{1.1}{(1-v)^4} + \frac{0.1}{(1-v)^2}\right)} \tag{1.8}$$

Le variabili nelle funzioni (1.6 - 1.8) sono

$$x = \frac{l}{l_0} \tag{1.9a}$$

$$v = \frac{V}{V_0} \tag{1.9b}$$

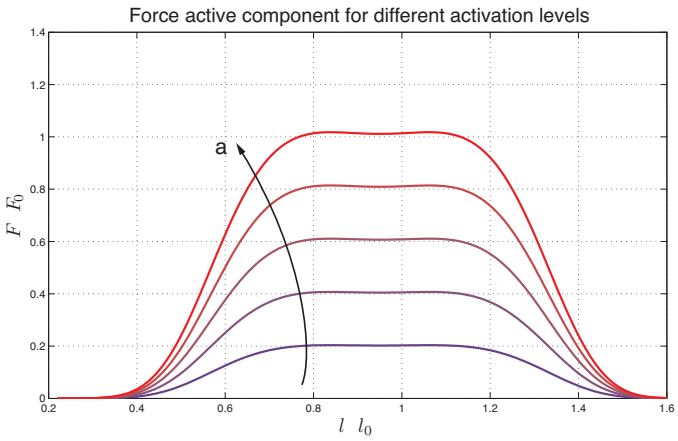

Figura 8: Componente attiva della forza nel sarcomero per differenti livelli di attivazione a velocità di contrazione nulla. La curva inferiore corrisponde ad $a = 0.2$ mentre la più alta ad $a = 1$, con passo di 0.2.

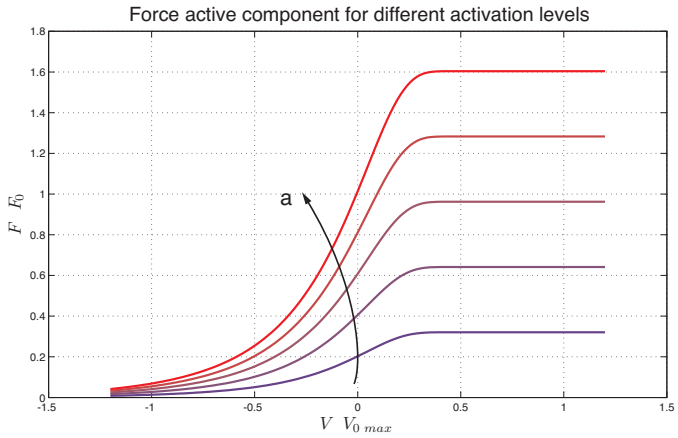

Figura 9: Componente attiva della forza nel sarcomero per differenti livelli di attivazione. La lunghezza del sarcomero è costante a l_o. La curva inferiore corrisponde a $a = 0.2$ mentre quella più alta ad $a = 1$, con passo 0.2.

La lunghezza totale dei muscoli l è da considerare inclusi i tendini.

L'attivazione modifica le curve delle figure 3 e 4 senza cambiare la loro forma come mostrato nelle figure 8 and 9. La figura 7 mostra le curve iso-forza per la superficie di forza adimensionalizzata ammissibile in funzione di x e V.

Tabella 5: Parametri del modello di muscolo per i fasci muscolari presenti nel modello. Forze massime isometriche e lunghezze di ottimo sono desunte da [18], angoli di pennazione da [23, 18, 24].

	Muscolo	L_0 [mm]	F_0 [N]	α [deg]	P_1 [mm]			P_2 [mm]		
					x	y	z	x	y	z
Muscoli che connettono l'omero al resto del corpo										
1	Coracobrachialis	197	242.5	27	20	30	35	174	21	0
2	Deltoide - Anterior	179	1142.6	22	35	25	35	136	-12	10
3	Deltoide - Medialis	159	1142.6	15	35	-22	20	136	-24	18
4	Deltoide - Posterior	148	259.9	18	-35	10	0	136	-24	18
5	Latissimus Dorsi	380	1059.2	21	-65	110	-290	75	25	9
6	Pectoralis Major	147	1270.3	22	45	110	10	36	0	25
7	Supraspinatus	108	487.8	7	-36	80	35	-32	2	-13
8	Infraspinatus	111	1210.8	19	-32	80	-40	-26	0	-20
Muscoli che connettono il radio al resto del corpo										
9	Biceps brachii caput longus	388	624.3	0	0	-15	10	34	16	0
10	Biceps brachii caput brevis	324	435.6	0	20	30	25	3	16	0
Muscoli che connettono l'ulna al resto del corpo										
11	Triceps brachii caput longus	290	798.5	12	-35	20	-20	-15	0	-22
Muscoli che connettono l'omero all'ulna										
12	Anconeus	55	350	0	300	-5	-12	-14	7	-11
13	Triceps brachii caput laterale/mediale	211	1248.6	9	112	0	-28	-27	0	-6
14	Brachialis	140	987.3	0	196	-8	16	17	15	5

Tabella 6: Parametri del modello di muscolo per i fasci muscolari presenti nel modello – continuazione.

	Muscolo	L_0 [mm]	F_0 [N]	α [°]	P_1 [mm]			P_2 [mm]		
					x	y	z	x	y	z
Muscoli che connettono l'omero al radio										
15	Brachioradialis	306	261.3	2.4 ± 6	246	-7	0	238	-18	13
16	Pronator teres	148	566.2	9.6 ± 8	270	33	-7	55	-18	12
Muscoli che connettono l'omero alla mano										
17	Flexor carpi ulnaris	317	128.9	12.1	265	27	-5	5	30	23
18	Extensor carpi ulnaris	290	93.2	3.5	269	-27	-5	5	30	-18
19	Extensor digitorum	387	100.7	3.0	269	-20	-20	8	0	-16
20	Flexor digitorum superficialis	380	226.6	4.9 ± 0.7	275	27	-10	7	18	26
21	Flexor carpi radialis	307	74	3.1	275	27	-7	3	-20	32
22	Extensor carpi radialis	305	405.4	0	245	-20	0	5	-23	-11
Muscoli che connettono l'ulna al radio										
23	Pronator quadatrus	33	75.5	9.9 ± 3	200	7	14	236	27	23
24	Supinator	61	476	< 15	13	17	-8	28	13	-24
Muscoli che connettono l'ulna alla mano										
25	Adbuctor pollicis longus	202	59.5	2.6 ± 6	115	-21	-5	3	-18	23

2

DINAMICA INVERSA E FORZE MUSCOLARI

2.1 INVERSIONE DELLA CINEMATICA

2.1.1 *Meccanismi ridondanti*

Come descritto più sopra, il modello possiede 7 gradi di libertà.

Per rendere possibile l'inversione della dinamica, le storie temporali di posizione, velocità e accelerazione della mano devono essere imposte. Dal momento, però , che questo comporta un numero massimo di gradi di libertà imposti pari a 6, il modello presenta una ridondanza di un grado di libertà, e vincoli aggiuntivi devono essere imposti per poterne invertire la cinematica.

Le equazioni algebriche dei vincoli possono essere riassunte,

$$\boldsymbol{\Phi}(\mathbf{q}) = 0, \tag{2.1}$$

a queste è possibile affiancare i vincoli di movimento imposto

$$\boldsymbol{\psi}(\mathbf{q}) = \overline{\mathbf{q}}_h(t). \tag{2.2}$$

nei sistemi completamente determinati, la risoluzione della cinematica è spesso ottenuta a livello delle velocità, derivando rispetto al tempo le equazioni di vincolo per ottenere un sistema lineare

$$[\varphi(\mathbf{q}, t)_{/q}]\dot{\mathbf{q}} = \begin{bmatrix} [\Phi_{/q}] \\ [\psi_{/q}] \end{bmatrix} = \begin{Bmatrix} 0 \\ \dot{\overline{\mathbf{q}}}_h(t) \end{Bmatrix} \tag{2.3}$$

La matrice $[\varphi(\mathbf{q}, t)_{/q}]$ è quadrata $n \times n$ e ha rango pieno se i vincoli sono ben posti. E' quindi invertibile,

$$\dot{\mathbf{q}} = -[\varphi(\mathbf{q}, t)_{/q}]^{-1}\boldsymbol{\varphi}(\mathbf{q}, t)_{/t} \tag{2.4}$$

Se il sistema è ridondante, al contrario, $[\varphi(\mathbf{q}, t)_{/q}]$ non è quadrata: se m è il numero delle equazioni di vincolo, risulta una matrice $m \times n$, non

invertibile in senso classico.

Un modo per risolvere l'indeterminazione risulta quello di risolvere ad ogni passo un problema di ottimizzazione, in cui la funzione di costo è generalmente funzione del problema.

Molte tecniche diverse sono disponibili per invertire la cinematica di sistemi ridondanti in modo efficiente [17, 21, 27, 16], ma quello che è stato considerato più adatto per gli scopi di questo lavoro è quello proposto in [9], basato sulla risoluzione di un sistema statico equivalente al sistema originario, ma vincolato da elementi elastici - fittizi, che impongono dei pesi rispetto al movimento di alcuni gradi di libertà in ragione della loro rigidezza relativa. Il sistema risolvente risulta

$$\Delta \mathbf{q} = [K]^{-1}[\varphi_{/q}]^T([\varphi_{/q}][K]^{-1}[\varphi_{/q}])^T(\overline{\mathbf{q}}_h(t) - \varphi(\mathbf{q}, t)\mathbf{q}) \tag{2.5}$$

in cui [K] è la matrice di rigidezza associata con le molle fittizie. Se [K] ha la forma $\gamma[I]$, con γ scalare, la soluzione corrispondente alla minimizzazione della norma delle velocità viene ritrovata.

Risolvere la cinematica al livello delle posizioni ha però uno svantaggio: per poter imporre velocità e accelerazioni dell'end-effector (in queso caso, della mano) è necessario derivare numericamente le componenti in posizione, processo che non assicura a volte la qualità della soluzione necessaria. Per ovviare a questo inconveniente, una metodo per ottenere l'inversione completa della cinematica di un meccanismo ridondante è stato sviluppato nell'ambito di questo lavoro.

2.2 INVERSIONE CINEMATICA COMPLETA DI UN SISTEMA RIDONDANTE

2.2.1 *Posizioni*

L'inversione a questo livello avviene riferendo il problema da un sistema statico equivalente, soggetto all'azione di elementi elastici fittizi in grado di introdurre coefficienti di costo dipendenti dalla configurazione. La funzione di costo del problema di ottimizzazione che viene risolto ad ogni istante di tempo dipende dall'energia potenziale elastica di questi elementi. Ad essa viene aggiunto un termine il cui fine è controllare

la qualità della soluzione ottenuta, dipendente dalla distanza della soluzione al passo corrente rispetto a quella del passo che lo precede

$$J_s = E_p + w_q(\mathbf{q} - \mathbf{q}_{prev})[M](\mathbf{q} - \mathbf{q}_{prev}) \tag{2.6}$$

$\mathbf{q}_{prev}$ sono le posizioni al passo precedente; w_q un coefficiente di peso.

Usando il metodo dei moltiplicatori di Lagrange, il sistema diventa

$$([K(\mathbf{q})] + [M]w_q)\mathbf{q} + [\varphi_{/q}]\boldsymbol{\lambda}^T = [K]\mathbf{q}_0 + w_q[M]\mathbf{q}_{prev} \tag{2.7a}$$

$$\varphi(\mathbf{q}, t) = \overline{q}_h \tag{2.7b}$$

Che può essere risolto con metodi alla Newton - Raphson.

La rigidezza degli elementi elastici può essere scelta in modo da riflettere le caratteristiche del sistema che si sta analizzando: in questo caso, è stato scelto di usare elementi elastici in grado di imporre un costo proporzionale al discomfort associato ad una configurazione, in analogia a quanto proposto in [31]: sono stati introdotti quindi elementi elastici rotazionali con rigidezza crescente all'allontanarsi dalla posizione articolare media.

Questo metodo è molto facile da implementare e controllare, ed ha interpretazione immediata. Non è però legato a quantità fisiologiche, come sembrerebbe più appropriato.

E' stato scelto quindi di affiancare agli elementi elastici rotazionali anche degli elementi elastici monodimensionali, rappresentanti i muscoli in condizioni di attivazione nulla: la componente passiva della forza muscolare è infatti funzione della sola deformazione del muscolo, ed è quindi disponibile ad ogni istante di tempo, mentre i coefficienti di attivazione sono estratti tramite un post-processing dei risultati della dinamica inversa. Questa componente di forza muscolare è nulla fino a quando il muscolo non viene portato ad una lunghezza superiore alla propria lunghezza di ottimo isometrico, mentre presenta una pendenza marcata per allungamenti superiori. E' quindi un buon indice del fatto che il braccio si sta portando in una posizione potenzialmente poco confortevole, e quindi poco probabile.

2.2.2 *Velocità*

Anche il problema in velocità risulta sottoderminato, ed è risolto anche in questo caso imponendo la minimizzazione di una funzione di costo

come vincolo aggiuntivo.

La derivata numerica della soluzione in posizione è calcolata ad ogni passo

$$\dot{\mathbf{q}}_{k+1} = \frac{1+|\rho_\infty|}{h}(\mathbf{q}_{k+1} - \mathbf{q}_k) - |\rho_\infty|\dot{\mathbf{q}}_k \tag{2.8}$$

Con ρ_∞ raggio spettrale asintotico. Per ragioni legate alla stabilità del metodo, anche se è questa forma più generale ad essere implementata, il raddio spettrale è stato fissato pari a zero, e il metodo si riduce quindi ad un metodo di Eulero implicito. Il funzionale di costo è definito in analogia al problema nelle posizioni con l'unica differenza che la parte che controlla la qualità della soluzione è dipendente dalla velocità al passo precedente

$$J_s = \frac{1}{2}(\dot{\mathbf{q}} - \dot{\mathbf{q}}_0)^T[R](\dot{\mathbf{q}} - \dot{\mathbf{q}}_0) + w_{\dot{q}}\frac{1}{2}(\dot{\mathbf{q}} - \dot{\mathbf{q}}_{prev})[M](\dot{\mathbf{q}} - \dot{\mathbf{q}}_{prev}) \tag{2.9}$$

la soluzione del problema è data dalla soluzione del sistema

$$([R] + w_{\dot{q}}[M])\dot{\mathbf{q}} + [\varphi_{/q}]^T\boldsymbol{\lambda} = [R]\dot{\mathbf{q}}_0 + w_{\dot{q}}[M]\dot{\mathbf{q}}_{prev} \tag{2.10a}$$

$$[\varphi_{/q}]\dot{\mathbf{q}} = \dot{\bar{q}}_h \tag{2.10b}$$

2.2.3 *Accelerazioni*

Ancora una volta l'approccio è identico, e il funzionale pesa la derivata numerica delle velocità congiuntamente alla differenza fra la soluzione al passo corrente e la soluzione al passo precedente, in termini di accelerazioni.

$$J_s = \frac{1}{2}(\ddot{\mathbf{q}} - \ddot{\mathbf{q}}_0)^T[M](\ddot{\mathbf{q}} - \ddot{\mathbf{q}}_0) + w_{\ddot{q}}\frac{1}{2}(\ddot{\mathbf{q}} - \ddot{\mathbf{q}}_{prev})^T[M](\ddot{\mathbf{q}} - \ddot{\mathbf{q}}_{prev}) \tag{2.11}$$

e quindi il sistema risolvente risulta

$$(1 + w_{\ddot{q}})[M]\ddot{\mathbf{q}} + [\varphi_{/q}]^T\boldsymbol{\lambda} = [M]\ddot{\mathbf{q}}_0 + w_{\ddot{q}}[M]\ddot{\mathbf{q}}_0 \tag{2.12a}$$

$$[\varphi_{/q}]\ddot{\mathbf{q}} = \ddot{\mathbf{q}}_{prev} - ([\varphi_{/q}]\dot{\mathbf{q}})_{/q}\dot{\mathbf{q}} \tag{2.12b}$$

2.3 INVERSIONE DELLA DINAMICA E IDENTIFICAZIONE DELLE FORZE MUSCOLARI

Nota la cinematica del sistema, il problema si sposta sulla determinazione delle coppie ai giunti necessarie all'ottenimento della cinematica stessa. Scritto in coordinate di giunto, il problema risulta

$$[M]\ddot{\mathbf{q}} + [\Phi_{/q}]^T\boldsymbol{\lambda} + [\vartheta_{/q}]^T\mathbf{c} = \mathbf{f} \tag{2.13}$$

Le accelerazioni sono note dalla soluzione del prolema di cinematica inversa, e quindi il vettore $[M]\ddot{\mathbf{q}}$ può essere portato a termine noto

$$\begin{bmatrix} \Phi_{/q} \\ \vartheta_{/q} \end{bmatrix}^T = \mathbf{f} - [M]\ddot{\mathbf{q}} \tag{2.14}$$

Dalla soluzione del sistema si ricava il vettore $\mathbf{c}$ delle coppie necessarie a garantire la cinematica imposta.

Le coppie sono generate da 25 fasci muscolari, che agiscono per produrre le 7 componenti del vettore $\mathbf{c}$. Il problema è quindi sovraattuato, e ancora una volta presenta una indeterminazione. Quest'ultima può essere risolta imponendo la minimizzazione dell'attivazione totale dei muscoli, dal momento che lo stato del sistema è noto ad ogni istante. Le forze muscolari devono quindi essere tali che sussista la relazione

$$\mathbf{c} = [\vartheta^+_{/q}]^T[B(\mathbf{q})]\mathbf{f}_m \tag{2.15}$$

La matrice $[\vartheta^+_{/q}]^T$ rappresenta la pseudoinversa trasposta dello Jacobiano delle coordinate di giunto, e la matrice $[B(\mathbf{q})]$ contiene i bracci e le proiezioni delle forze muscolari sulle coordinate generalizzate. Le forze possono essere separate in una componente attiva, dipendente dai coefficienti di attivazione, e una componente passiva, funzione solo dello stato del sistema

$$\mathbf{f} = [F_{0m}](\mathbf{f}_0(\mathbf{q}) + [F_a(\mathbf{q}, \dot{\mathbf{q}})]\boldsymbol{\alpha}) \tag{2.16}$$

Anche il vettore delle coppie è quindi separabile in una componente dovuta alle forze attive e ad una dovuta alle forze passive.

Il sistema risolvente risulta quindi dalla minimizzazione del funzionale

$$J_s = \frac{1}{2}\mathbf{a}^T[W]\mathbf{a} \tag{2.17}$$

soggetto ai vincoli

$$[B_a(\mathbf{q}, \dot{\mathbf{q}})]\mathbf{a} - \mathbf{c}_a = 0 \tag{2.18a}$$

$$\phi^T_{/\mathbf{q}}\mu = 0 \tag{2.18b}$$

$$0 \leqslant a \leqslant 1 \tag{2.18c}$$

Un generico algoritmo di ottimizzazione, implementato in *MATLAB*® è stato usato per questo scopo.

To be able to solve system 2.18, projector $[\varphi^{\dagger}_{/\mathbf{q}}]^T$ and matrix [B] need to be built for the model.

2.4 VALIDAZIONE DEL MODELLO: DINAMICA INVERSA

Al fine di valutare la bontà del modello e del metodo di identificazione delle forze muscolari, sono state effettuate simulazione di due tipi.

La prima mira alla stima dei massimi momenti producibili in condizioni isometriche da gruppi di muscoli sinergici agenti sullo stesso giunto, mentre un secondo valuta le capacità del modello di stimare pattern di attivazione muscolare corrispondenti ad una traiettoria imposta alla mano.
Per entrambi è stato fatto riferimento a dati sperimentali tratti dalla letteratura per la comparazione dei risultati e il confronto critico.

2.5 VALIDAZIONE DEL MODELLO

2.5.1 *Massimi momenti articolari*

Ogni movimento articolare è reso possibile dall'azione di un (generalmente) ristretto numero di fasci muscolari agenti in concomitanza in una direzione, e da un corrispondente gruppo di muscoli che agiscono in direzione opposta.

Imponendo il movimento articolare corrispondente al primo gruppo in modo che sia molto lento, e attivando i corrispondenti fasci muscolari, si può stimare il momento massimo che questi ultimi sono in grado di generare a partire dalle reazioni vincolari del giunto stesso.

In questa fase, i risultati sono messia confronto con risultati numerici e sperimentali riportati in letteratura, facendo riferimento per la maggior parte alla pubblicazione di Holzbaur e altri [18], che riporta dati sperimentali da una vasta letteratura per eseguire una analoga validazione.

2.5.1.1 *Momenti di abduzione e adduzione della spalla*

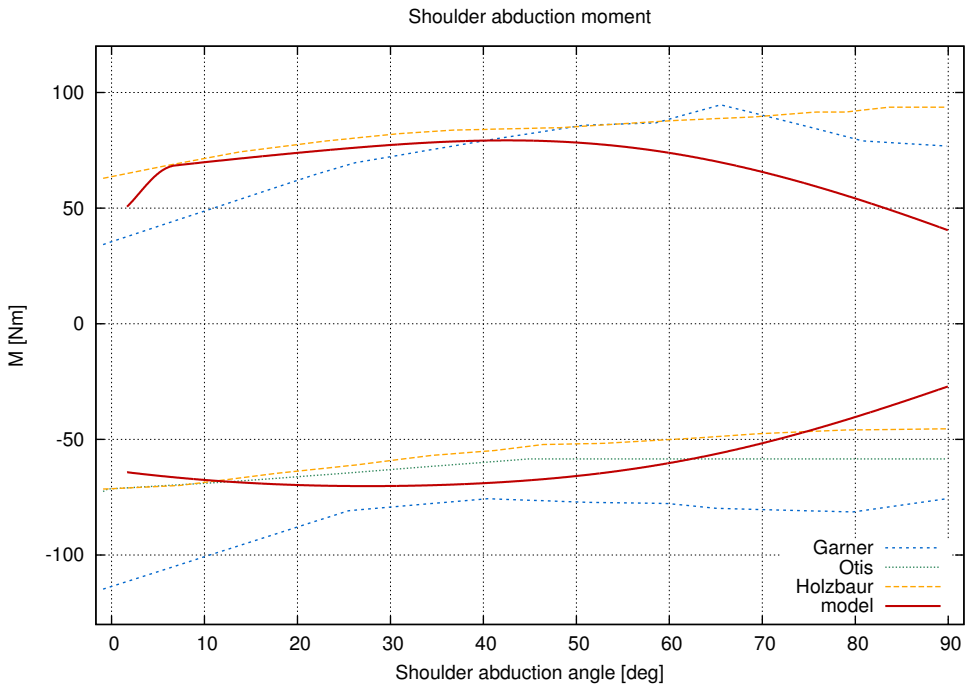

Figura 10: Massimo momento di abduzione della spalla in condizioni isometriche. Il risultato del modello è messo a confronto con risultati pubblicati da Holzbaur [18], Garner and Pandy [10] e Otis [30]. L'angolo di abduzione è considerato 0° quando il braccio è in posizione di riposo, lungo il corpo, mentre vale 90° quando il braccio è completamente abdotto.

La stima relativa al momento massimo di abduzione della spalla è ottenuta a partire da una configurazione in cui il braccio è a riposo

lungo il corpo, l'omero è quindi esteso con una rotazione positiva di 90° rispetto al suo asse y, facendo riferimento alla Figura 1. Alla spalla è imposta una lenta abduzione di 90°, ovvero una rotazione negativa di 90° rispetto al suo asse x. I gruppi muscolari attivi in questa fase sono riportati in Tabella 2.5.1.2. Il massimo momento di abduzione stimato, pari a 71 Nm, è compatibile con i dati pubblicati da Garner ad Pandy [10], Otis et al. [30] and Holzbaur et al. [18]. Lo stesso si può dire del massimo momento di adduzione, pari a 82 Nm. Fino ad angoli di 70°, anche l'andamento dei momenti è correttamente riprodotto. La perdita in precisione per angoli di abduzione elevati è dovuta alla semplificazione del complesso della spalla, operata nella scelta dei vincoli e dei corpi rigidi presenti nel modello: ad angoli così elevati infatti il movimento di scapola e clavicola può determinare importanti variazioni dei bracci delle forze muscolari coinvolte.

Durante il controllo di veicoli, però, il braccio è generalmente in posizione poco abdotta.

Tabella 7: Muscoli attivi per l'abduzione e l'adduzione della spalla

Muscoli che adbucono l'omero
Deltoid, fibre intermedie
Infraspinatus
Supraspinatus
Muscoli che adducono l'omero
Deltoid, fibre anteriori
Pectoralis Major
Latissimus dorsi

2.5.1.2 *Flessione della spalla*

In questo caso, il braccio è posto in lenta flessione a partire dalla posizione di riposo, con omero disteso lungo il lato del corpo.

I gruppi muscolari attivi in questa fase sono riportati in Tabella 8.

I momenti di flessione e di estensione sono riprodotti con una buona precisione. Il momento massimo, pari a 107 Nm, rappresenta un valore più elevato rispetto a quelli riportati in letteratura nel range 30-50°, ma è anche da notare che la varianza associata ai risultati sperimentali è

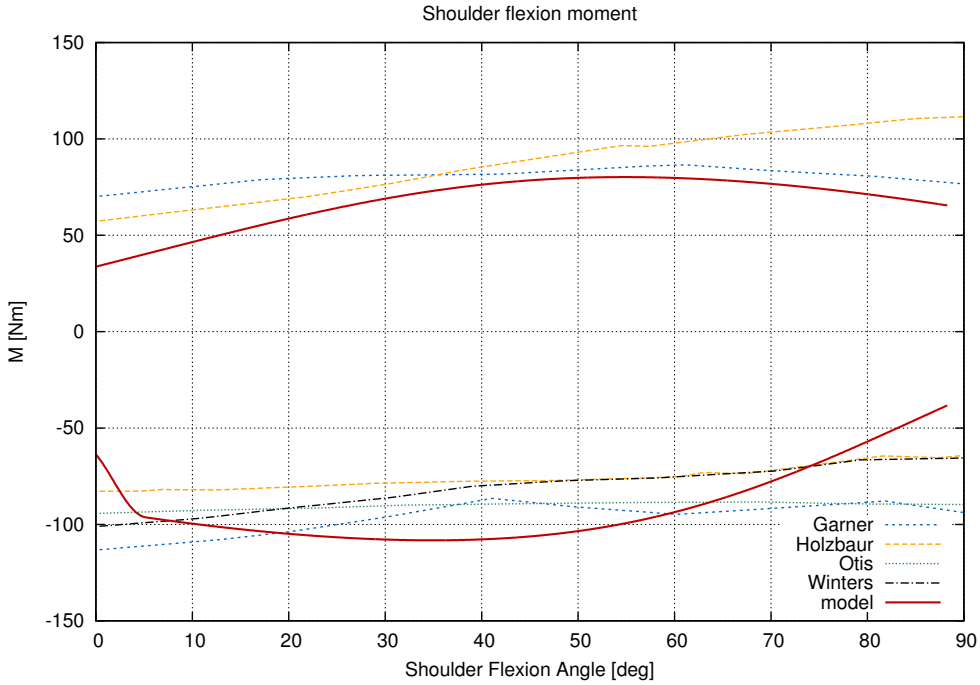

Figura 11: Momenti di flessione in condizioni isometriche della spalla calcolati dal modello, a confronto con dati da Holzbaur [18], Garner and Pandy [10] and Otis [30] and Winters [36]. Un angolo di 0° in figura corrisponde alla posizione di braccio disteso lungo il corpo, e un angolo di 90° alla completa flessione

generalmente molto elevata. Al contrario, il modello sottostima di soli 1.4 Nm il momento di estensione a 50° se confrontato ai risultati di Garner [10], e la forma della curva è riprodotta correttamente. Anche in questo caso, una certa perdita di accuratezza è osservabile a partire da circa 70°, per gli stessi motivi esposti più sopra.

2.5.1.3 *Flessione dell'avambraccio*

In questo caso il braccio inizia la simulazione nella sua posizione di riposo, lungo il lato del corpo, e il gomito è flesso progressivamente e lentamente fino ad un angolo di 140°.

I musculi flessori dell'avambraccio sono più vigorosi dei corrispondenti estensori, e il modello riproduce correttamente questa caratteristica, come si può notare in Figura 12. Il massimo momento di flessione è pari a 73 Nm, a fronte di dati sperimentali nel range 75-80 Nm. Il mo-

Tabella 8: Muscoli attivi per la flessione e l'estensione della spalla.

Muscoli flessori della spalla
Deltoide, fasci anteriori e intermedi Pectoralis Major
Muscoli estensori della spalla
Deltoide, fibre posteriori Latissimus dorsi

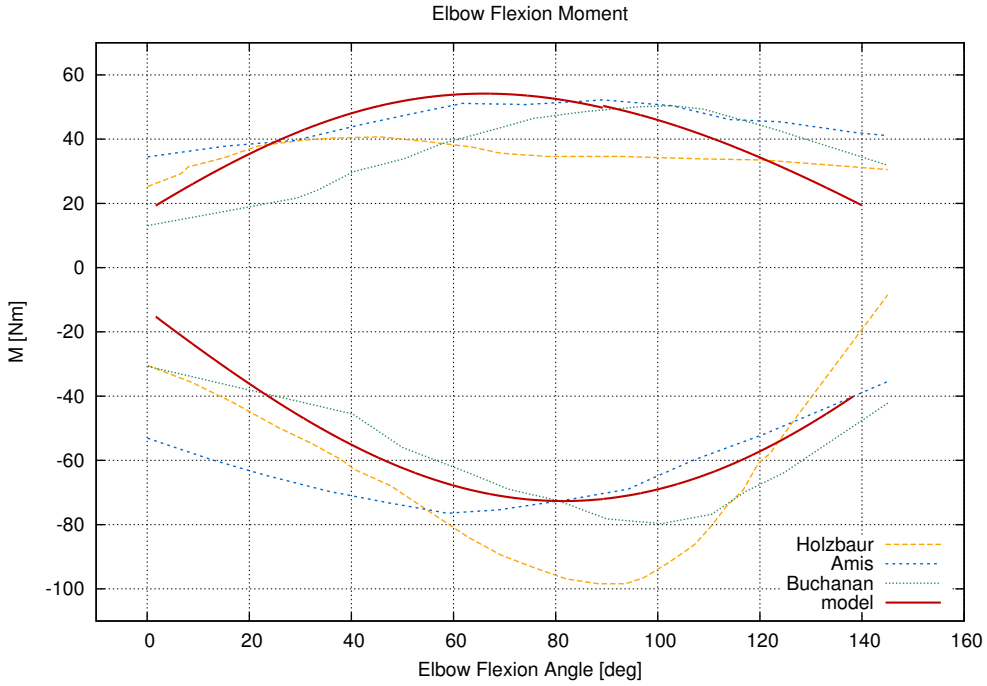

Figura 12: Momento di flessione del gomito in condizioni isometriche stimato dal modello, a confronto con dati provenienti da Holzbaur [18], Amis [2] and Buchanan [4]. Un angolo di flessione di 0° corrisponde all'avambraccio completamente esteso, mentre la massima flessione è raggiunta ad un angolo pari a 140°

mento di estensione è nel range dei dati pubblicati, e il suo andamento è riprodotto in modo corretto.

Tabella 9: Muscoli attivi per la flessione e l'estensione dell'avambraccio.

Muscoli flessori dell'avambraccio
Brachialis
Brachioradialis
Biceps (entrambi i capi)
Pronator Teres
Muscoli estensori dell'avambraccio
Triceps, tutti i capi

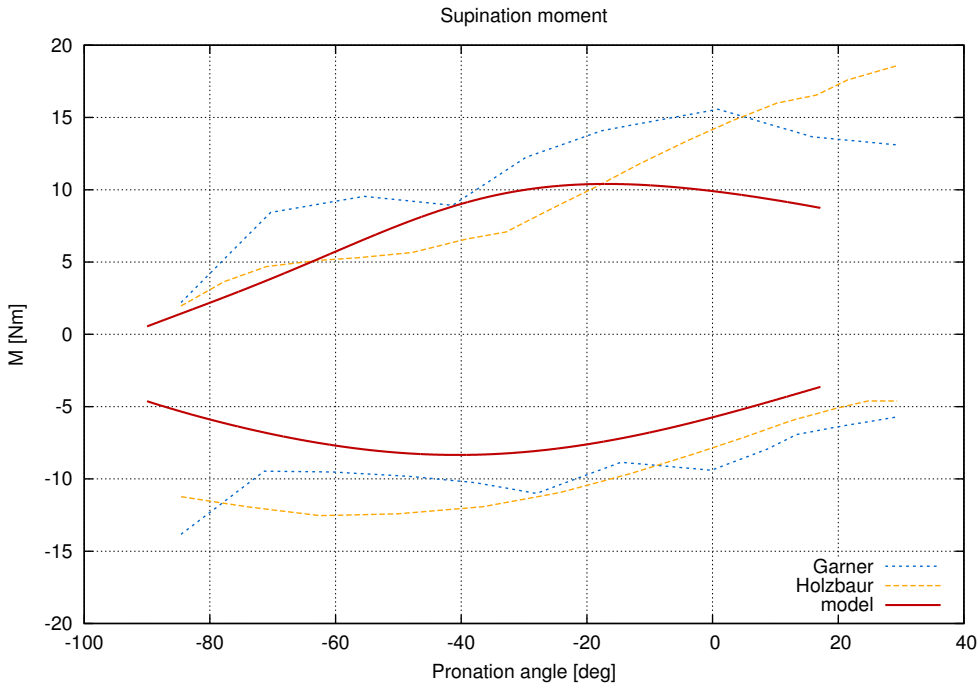

Figura 13: Momento isometrico di supinazione stimato, a confronto con dati da Holzbaur [18] and Garner [10]. Angoli positivi corrispondo ad avambraccio pronato.

2.5.1.4 *Pronazione dell'avambraccio*

Il braccio inizia la simulazione nella sua posizione completamente flessa, con l'omero orizzontale e la mano che punta anteriormente, il gomito completamente esteso e il palmo della mano verso l'alto. La mano stessa viene messa in lenta rotazione attorno al suo asse x, fino ad un angolo

di pronazione leggermente inferiore a 20°.

Dal confronto con i dati sperimentali si evince che i momenti di prono-supinazione sono leggermente sottostimati dal modello. Il momento di supinazione, in particolare, è al di sotto dei range di dati sperimentali disponibili. Questa limitazione è però considerata non stringente, in quando nelle applicazioni considerate i momenti di prono-supinazione sono generalmente trascurabili o quasi trascurabili.

Tabella 10: Muscoli attivi per la pronazione e la supinazione dell'avambraccio

Muscoli pronatori dell'avambraccio
Brachioradialis
Pronator Quadratus
Pronator Teres
Muscoli supinatori dell'avambraccio
Supinator Brevis
Biceps

2.5.1.5 *Flessione del polso*

Per stimare i momenti massimi legati alla flessione ed estensione del gomito, il braccio è posto in una configurazione con l'omero parallelo al piano orizzontale, rivolto in avanti. La mano inizia la simulazione flessa di -50°, e raggiunge un angolo di estensione massimo di 50°.

Dati sperimentali riportati Delp e altri [6] e dati numerici provenienti dal modello biomeccanico sviluppato da Holzbaur e altri [18] sono messi a confronto con i risultati desunti dal modello. Sia gli andamenti che i valori assoluti dei momenti presentano un buon accordo, con la sola eccezione del momento di estensione, moderatamente sottostimato.

2.5.1.6 *Deviazione del polso*

La deviazione del polso, in direzione ulnare e radiale, è resa possibile dai gruppi muscolari riportati in Tabella 12. In questa simulazione la mano ruota da -20° a + 20°, ossia da 20° in direzione ulnare a 20° in direzione radiale.

I valori di momento stimati posso essere paragonati favorevolmente con i dati sperimentali disponibili, pubblicati da Delp e altri [6].

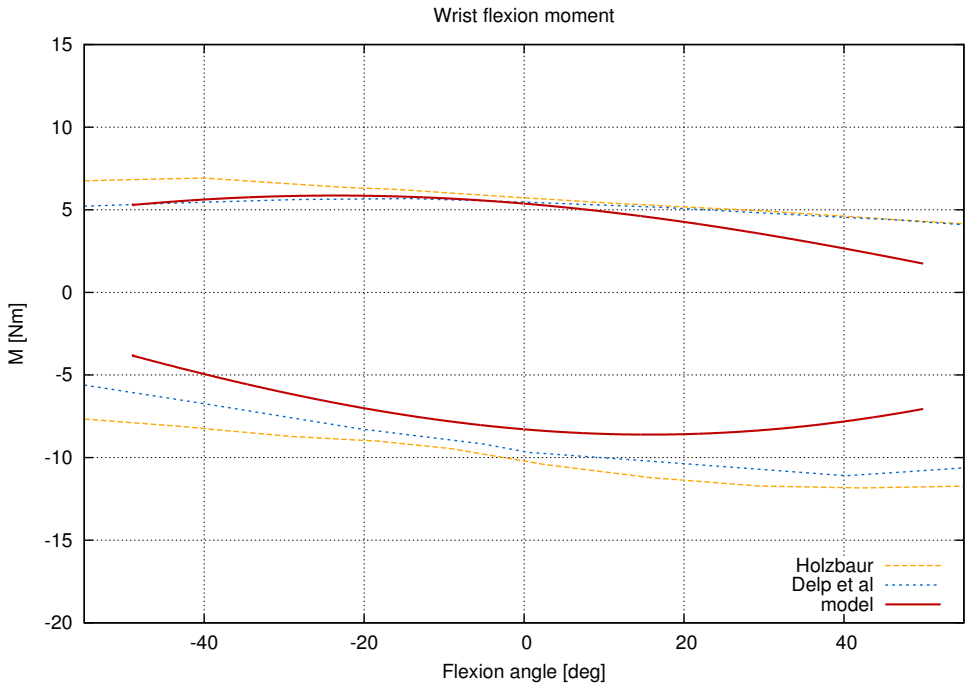

Figura 14: Momenti massimi in condizioni isometriche di flessione del polso stimati dal modello, a confronto con dati pubblicati da Holzbaur [18] and Delp [6]. Angoli positivi corrispondono a condizioni di estensione del polso.

Tabella 11: Muscoli attivi per la flessione e l'estensione del polso

Muscoli flessori del polso
Flexor Carpi Radialis
Flexor Carpi Ulnaris
Flexor Digitorum
Abductor Pollicis Longus
Muscoli estensori del polso
Extensor Carpi Radialis
Extensor Carpi Ulnaris
Extensor Digitorum

2.5.2 *Attivazione muscolare*

Per esaminare le prestazioni del modello nei riguardi della riproduzione corretta dei pattern di attivazione, è stata riprodotto numericamente

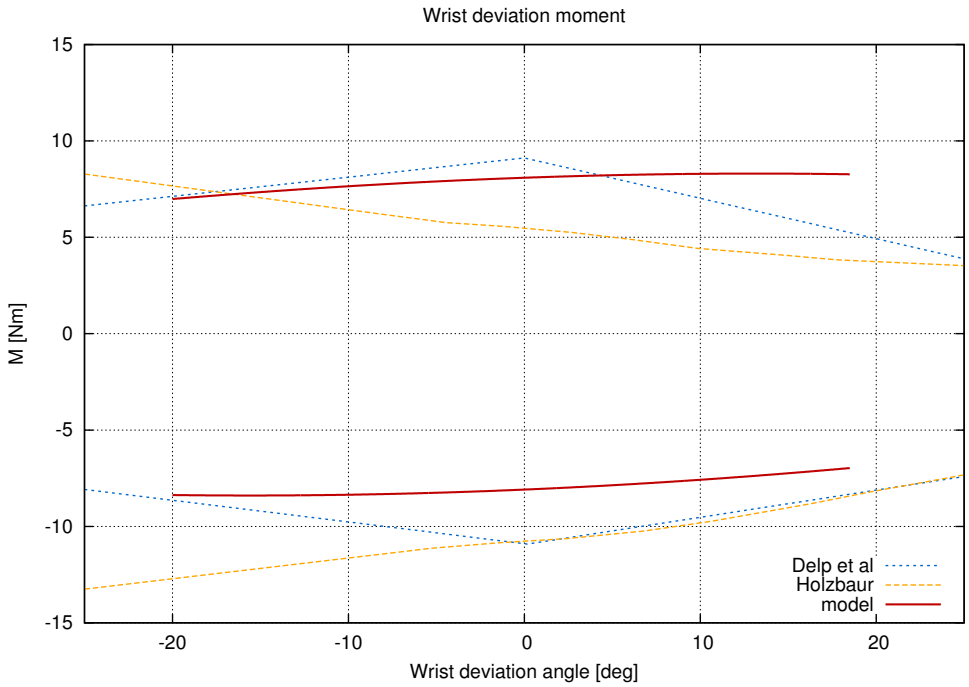

Figura 15: Massimi momenti di deviazione del polso stimati dal modello, messi a confronto con risultati sperimentali e numerici pubblicati da Holzbaur [18] e Delp [6]. Angoli positivi corrispondono alla flessione del gomito.

Tabella 12: Muscoli attivi per la deviazione del polso.

Muscoli che effettuano la deviazione ulnare
Flexor Carpi Ulnaris
Extensor Carpi Ulnaris
Extensor Digitorum
Flexor Digitorum
Muscoli che effettuano la deviazione radiale
Extensor Carpi Radialis
Flexor Carpi Radialis
Abductor Pollicis Longus

l'esperimento di Huang et al. [20]. In questo esperimento l'attivazione di quattro gruppi muscolari della spalla e del braccio è stata misurata

per mezzo di elettromiografia (EMG) mentre i soggetti svolgevano attività fisica su di un macchinario da palestra chiamato *stepper* capace di imporre, con scarti inferiori all'1%, la traiettoria della mano.

Il movimento della mano è stato imposto nel modello multibody per essere simile a quello usato in [20], e le attivazioni sono state calcolate con i metodi sopra esposti. I risultati sono riportati nelle Figure 16 e 17, in cui è possibile notare che gli andamenti generali sono correttamente individuati dal modello, mentre non è possibile una validazione vera e propria sul valore assoluto delle attivazioni, in quanto manca il dato riferito alla massima forza isometrica dei soggetti. D'altro canto un confronto sui valori assoluti non avrebbe molto senso, in assenza di dati antropometrici e biomeccanici dei soggetti coinvolti nella campagna sperimentale.

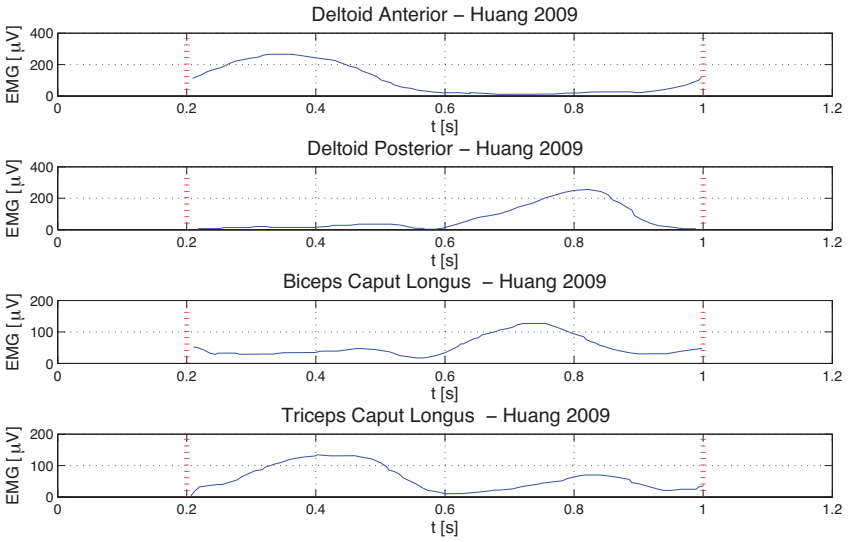

Figura 16: Dati EMG di Huang e altri [20], rilevati in un ciclo di *stepper*

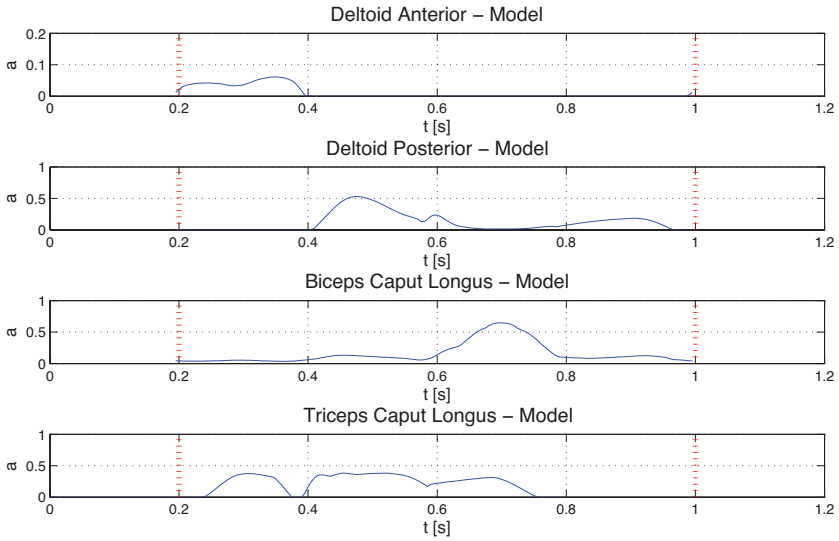

Figura 17: Coefficienti di attivazione calcolati dal modello, in una simulazione che ripete l'esperimento di [20].

3

IMPEDENZA EQUIVALENTE DELL'ARTO SUPERIORE

3.1 METODOLOGIA

Scopo finale della simulazione è quello di stimare l'impedenza meccanica equivalente dell'arto superiore, in condizioni dinamiche. Per superare i problemi legati ai metodi numerici usati comunemente, è stato seguito un metodo più analitico.

Se il sistema è in condizioni di equilibrio

$$[\phi_{/q}]^T\lambda + [\psi_{/q}]^T\mu = [B]f_m(q, \dot{q}, a) \tag{3.1a}$$

$$\psi(q) = \alpha(t) \tag{3.1b}$$

$$\phi(q) = 0 \tag{3.1c}$$

con μ vettore delle forze generalizzate che la mano applica al manipolatore, e $\psi(q)$ vettore che definisce le relazioni non lineari fra le coordinate generalizzate e il moto imposto.

Linearizzando la singola forza muscolare

$$\delta f_m(q, \dot{q}, a) = \frac{\partial f}{\partial x} \cdot \frac{1}{l_0}\frac{\partial l}{\partial q}\delta q + \frac{\partial f}{\partial v} \cdot \frac{1}{v_0}\left(\frac{\partial \dot{l}}{\partial q}\delta q + \frac{\partial \dot{l}}{\partial \dot{q}}\delta \dot{q}\right) \tag{3.2}$$

che può essere riscritta, separando i termini legati a δq da quelli legati a $\delta \dot{q}$

$$f_{/q}\delta q = f_{/x}\frac{1}{l_0}l^T[l_{/q}]\delta q \tag{3.3a}$$

$$f_{/\dot{q}}\delta q = f_{/v}\frac{1}{v_0}\dot{l}^T([I] - ll^T)[l_{/q}]\delta q \tag{3.3b}$$

$$f_{/\dot{q}}\delta \dot{q} = \frac{1}{v_0}l^T[l_{/\dot{q}}]\delta \dot{q} \tag{3.3c}$$

$[\mathbf{l}_{/\mathbf{q}}]$ and $[\mathbf{l}_{/\dot{\mathbf{q}}}]$ rappresenta la matrice delle derivate del vettore $\mathbf{l}$ rispetto alle coordinate generalizzate.

Le **??** definiscono le righe delle matrici $[\mathbf{f}_{\delta \mathbf{q}}]$ e $[\mathbf{f}_{\delta \dot{\mathbf{q}}}]$: le righe della prima sono la somma dei vettori riga che moltiplicano $\delta\mathbf{q}$ nelle prime due equazioni, mentre le righe della seconda i vettori riga che moltiplicano $\delta\dot{\mathbf{q}}$.

Mediante una perturbazione della 3.1 e una proiezione nelle coordinate di giunto

$$[\vartheta^{+}_{/\mathbf{q}}]^{T}[\psi_{/\mathbf{q}}]^{T}\delta\boldsymbol{\mu} = [\vartheta^{+}_{/\mathbf{q}}]^{T}[B][\mathbf{f}_{\delta\mathbf{q}}][\vartheta^{+}_{/\mathbf{q}}]\delta\boldsymbol{\theta} \tag{3.4a}$$

$$[\psi_{/\mathbf{q}}][\vartheta^{+}_{/\mathbf{q}}]\delta\boldsymbol{\theta} = \delta\boldsymbol{\alpha} \tag{3.4b}$$

che può essere riscritto come

$$\begin{bmatrix} -[\vartheta^{+}_{/\mathbf{q}}]^{T}[B][\mathbf{f}_{\delta\mathbf{q}}][\vartheta^{+}_{/\mathbf{q}}] & [\vartheta^{+}_{/\mathbf{q}}]^{T}[\psi_{/\mathbf{q}}]^{T} \\ [\psi_{/\mathbf{q}}][\vartheta^{+}_{/\mathbf{q}}] & [0] \end{bmatrix} \begin{Bmatrix} \delta\boldsymbol{\theta} \\ \delta\boldsymbol{\mu} \end{Bmatrix} = \begin{Bmatrix} 0 \\ [I]\delta\boldsymbol{\alpha} \end{Bmatrix} \tag{3.5}$$

dalo momento però che vale anche

$$\delta\boldsymbol{\theta} = [T]\delta\boldsymbol{\alpha} \tag{3.6a}$$

$$\delta\boldsymbol{\mu} = [K]\delta\boldsymbol{\alpha} \tag{3.6b}$$

$$\tag{3.6c}$$

il precedente sistema può essere infine riscritto per evidenziare la matrice di rigidezza

$$\begin{bmatrix} -[\vartheta^{+}_{\mathbf{q}}]^{T}[B][\mathbf{f}_{\delta\mathbf{q}}][\vartheta^{+}_{/\mathbf{q}}] & [\vartheta^{+}_{/\mathbf{q}}]^{T}[\psi_{/\mathbf{q}}]^{T} \\ [\psi_{/\mathbf{q}}][\vartheta^{+}_{/\mathbf{q}}] & [0] \end{bmatrix} \begin{bmatrix} [T] \\ [K] \end{bmatrix} \delta\boldsymbol{\alpha} = \begin{bmatrix} [0] \\ [I] \end{bmatrix} \delta\boldsymbol{\alpha} \tag{3.7}$$

una procedura del tutto analoga porta a scrivere

$$\begin{bmatrix} -[\vartheta^{+}_{\mathbf{q}}]^{T}[B][\mathbf{f}_{\delta\dot{\mathbf{q}}}][\vartheta^{+}_{/\mathbf{q}}] & [\vartheta^{+}_{/\mathbf{q}}]^{T}[\psi_{/\mathbf{q}}]^{T} \\ [\psi_{/\mathbf{q}}][\vartheta^{+}_{/\mathbf{q}}] & [0] \end{bmatrix} \begin{bmatrix} [T] \\ [R] \end{bmatrix} \delta\dot{\boldsymbol{\alpha}} = \begin{bmatrix} [0] \\ [I] \end{bmatrix} \delta\dot{\boldsymbol{\alpha}} \tag{3.8}$$

Le matrici $[K]$ e $[R]$ così trovate non rappresentano, a rigore, le *vere* matrici di massa e smorzamento equivalente del sistema, ma possono essere considerate come delle loro equivalenti per un sistema che è stato *congelato* nella condizione di riferimento.

3.2 TORQUE - LESS MODES OF ACTIVATION

Dal momento che una coppia articolare è sempre ottenuta dall'azione congiunta di gruppi muscolari, sicuramente in numero uguale o superiore al doppio del numero di giunti considerati, il problema di ricostruire le forze muscolari è quindi, come ricordato più volte, un problema che non ammette una soluzione unica.

Esistono quindi combinazioni lineari di forze muscolari che non cambiano la coppia agente sui giunti, ma che possono cambiare l'impedenza equivalente del sistema. Chiameremo ciascuna di queste combinazioni *torque-less activation mode* (TLAM).

In condizioni di equilibrio

$$\mathbf{c} = [\vartheta^{+}_{/\mathbf{q}}]^{T}[B(\mathbf{q})]\mathbf{f}_{m}(\mathbf{q}, \dot{\mathbf{q}}, \mathbf{a}). \tag{3.9}$$

e linearizzando la legge costitutiva dei muscoli,

$$\mathbf{f} = \mathbf{f}_{0}(\mathbf{q}) + \mathbf{f}_{/a}(\mathbf{q}, \dot{\mathbf{q}})a \tag{3.10}$$

si perviene ad una forma lineare del legame coppie-attivazioni, che perturbata porta a

$$[\vartheta^{+}_{/\mathbf{q}}]^{T}[B]\mathbf{f}_{/\mathbf{a}}\delta\mathbf{a} = [A]\delta\mathbf{a} = \delta\mathbf{c} \tag{3.11}$$

Applicando una decomposizione a valori singolari alla matrice $[A]$, è possibile isolare il suo spazio nullo

$$[A] = [U][\Sigma][V] = [U][[\Sigma][0]][[V_1][V_2]] \tag{3.12}$$

le colonne della matrice $[V_2]]$ sono i vettori singolari della matrice $[A]$, e rappresentano in questo caso proprio le combinazioni di valori dei coefficienti di attivazione che non portano ad una variazione di coppia nel giunto. La coppia è ora esprimibile anche in funzione del contributo dei TLAM

$$C_{/q} = [A]\left[f_{0/\mathbf{q}} + f_{a/\mathbf{q}}\left(\mathbf{a}_{min} + \sum \boldsymbol{\nu}_{i0}\mathbf{a}_{TLAM}\right)\right] \tag{3.13a}$$

$$C_{/\dot{q}} = [A]\left[f_{a/\dot{\mathbf{q}}}\left(\mathbf{a}_{min} + \sum \boldsymbol{\nu}_{i0}\mathbf{a}_{TLAM}\right)\right] \tag{3.13b}$$

3.3 ROTORCRAFT PILOT'S ARM IMPEDANCE IDENTIFICATION

3.3.1 *PAO testing at University of Liverpool*

Dati raccolti dal research group on rotorcraft aeroservoelasticity, Dipartimento di Ingegneria Aerospaziale del Politecnico di Milano sono stati utilizzati per ricostruire la cinematica del modello multibody.

I test qui presi in considerazione miravano alla valutazione di PAO (Pilot Induced Oscillations - See **??**) in situazioni di accoppiamento pilota-elicottero, e sono stati prodotti al Bibby Flight Simulation Laboratory della University of Liverpool, mediante l'utilizzo di un simulatore di elicottero a 2 gradi di libertà aeroelastico.

Il pilota nel test qui considerato cerca di mantenere un'altitudine costante, o di eseguire alcune manovre predeterminate, mentre l'aeromobile è soggetto a disturbi sull'asse verticale, agendo sul comando del collettivo.

La storia temporale della rotazione del comando, espressa in scostamento percentuale rispetto alla configurazione di riferimento (in questo caso collettivo al 50%) è riportata in Figura 18

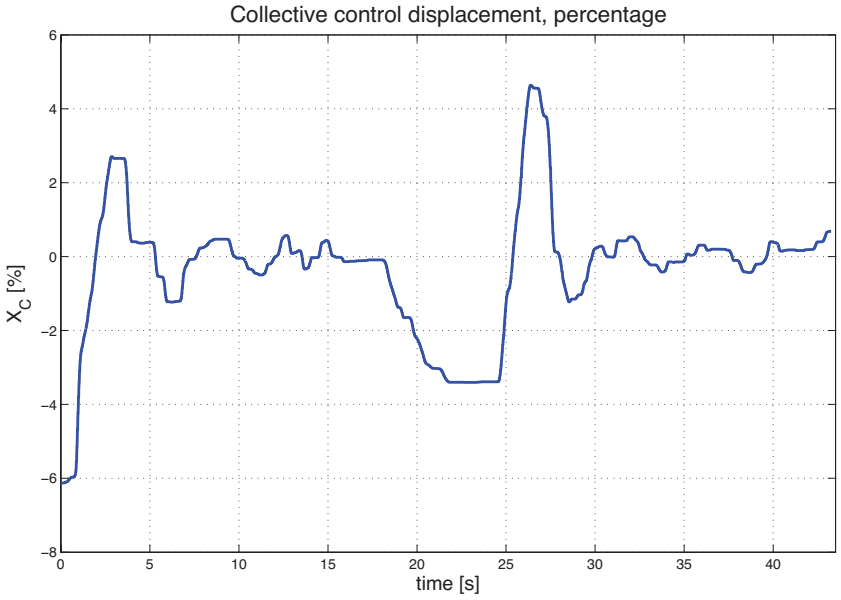

Figura 18: Storia temporale del comando del collettivo usata per imporre il moto nel modello multibody

A partire dalle informazioni sulla posizione del collettivo, la cinematica del braccio è ricostruita tramite il procedimento presentato alla Sezione **??**. Si può notare come lo spostamento angolare del collettivo è limitato, approssimativamente, al range -2.1° to +2°, ed è quindi piuttosto limitato.

Il campo di forze agente sul modello multibody è stato ridotto alla sola forza di gravità, mentre le azioni inerziali restituite dal simulatore sono state trascurate in questa analisi preliminare.

Le componenti di coppia articolare necessaria per eseguire le manovre sono quindi molto limitate, e anche le attivazioni dei muscoli, riportate in Figura 19 per i muscoli della spalla, sono di entità limitata.

Questa considerazione porta a presupporre che anche le componenti di rigidezza e smorzamento equivalente saranno contenute. In effetti questa previsione è confermata dai risultati ottenuti, riportati in Figura 20.

E' da sottolineare come le potenzialità del modello si fermino, allo stato attuale, all'individuazione dell'impedenza biomeccanica detta *intrinseca*, ovvero quella parte di impedenza dovuta alla componente attiva e passiva delle forze muscolari, ma non di quella parte dovuta alla eventuale reazione volontaria del pilota: per fare questo il modello dovrebbe comprendere un sistema di controllo attivo in feedback, capace di sfruttare la dinamica di attivazione per controllare la posizione della mano.

3.3.2 *Effetto dei Torque Less Activation Modes*

Tramite il procedimento delineato in 3.2, è possibile isolare le combinazioni lineari di attivazioni che modificano l'impedenza del sistema senza modificarne le coppie ai giunti. E' importante verificare il potenziale contributo dei TLAMs per verificare l'importanza relativa che essi possono rivestire nel cambiamento delle caratteristiche meccaniche equivalenti del pilota: si pensi ad un pilota in stato di tensione nervosa. Egli impugnerà i comandi in modo certamente più saldo di un pilota rilassato, ed è quindi facile immaginare che la sua impedenza equivalente sia più alta.

Un effetto come questo non è rappresentabile tramite la sola attivazione minima, ma risulta dipendente dall'attivazione contemporanea di diversi gruppi di muscoli antagonisti.

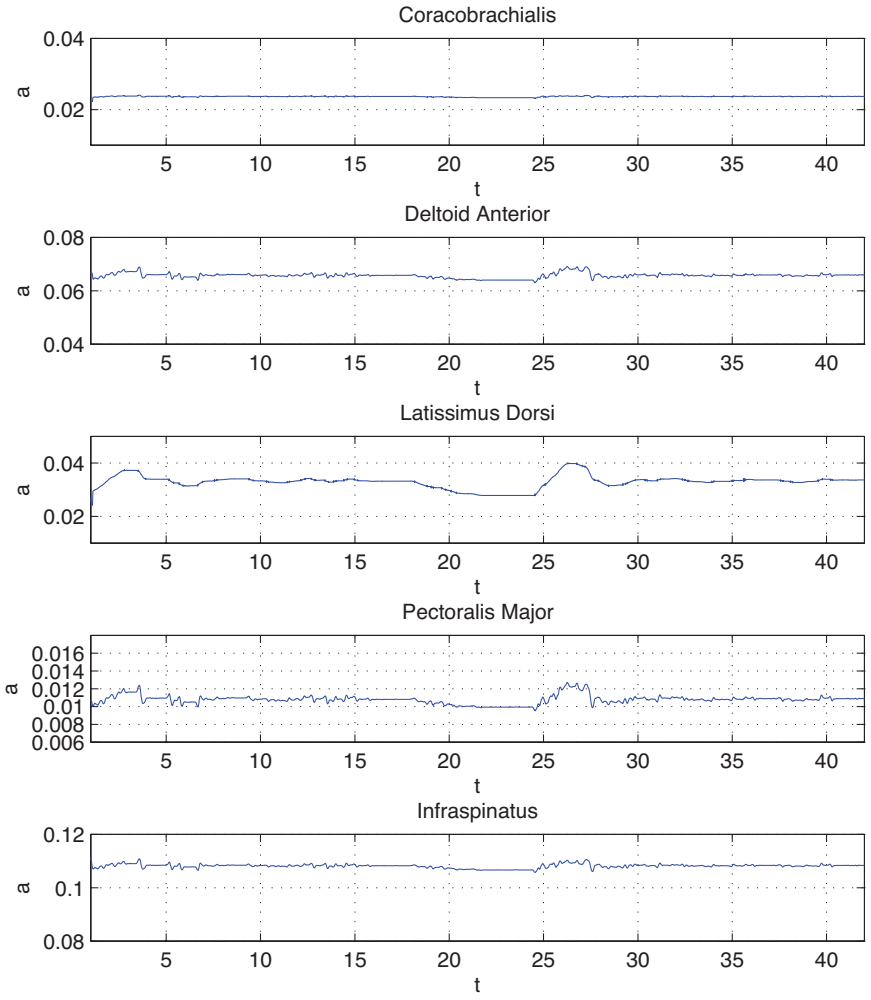

Figura 19: Parametri di attivazione dei gruppi muscolari della spalla durante la manovra. Sono mostrati solo i gruppi muscolari più attivi. E' facile notare come i gruppi corretti sono effettivamente attivati.

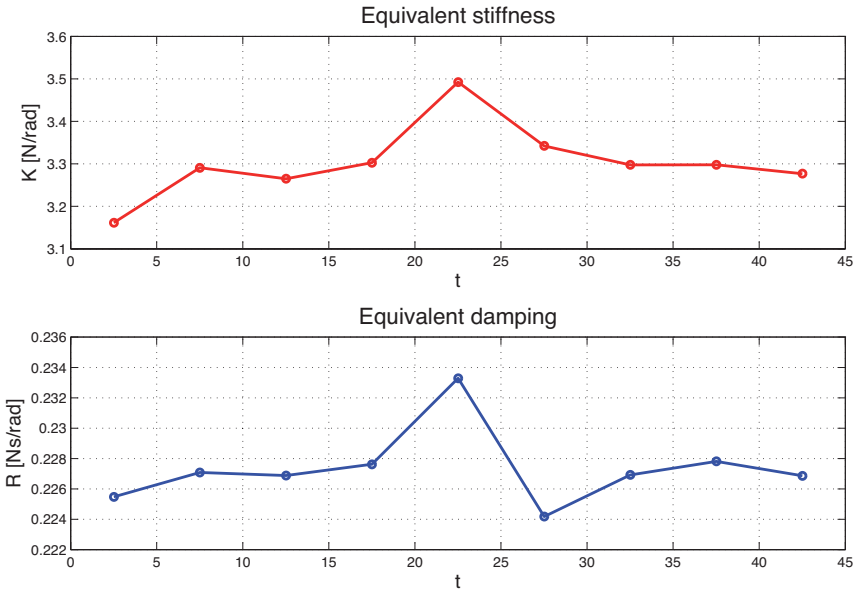

Figura 20: Impedenza intrinseca dell'arto superiore, calcolata ogni 5 s a partire da $t = 2.5$ s

Si può vedere come l'impedenza vari in funzione dei TLAM anche in modo importante: la rigidezza media aumenta del 30% a seguito dell'effetto dei TLAM considerati, e lo smorzamento medio aumenta fino a 4 volte.

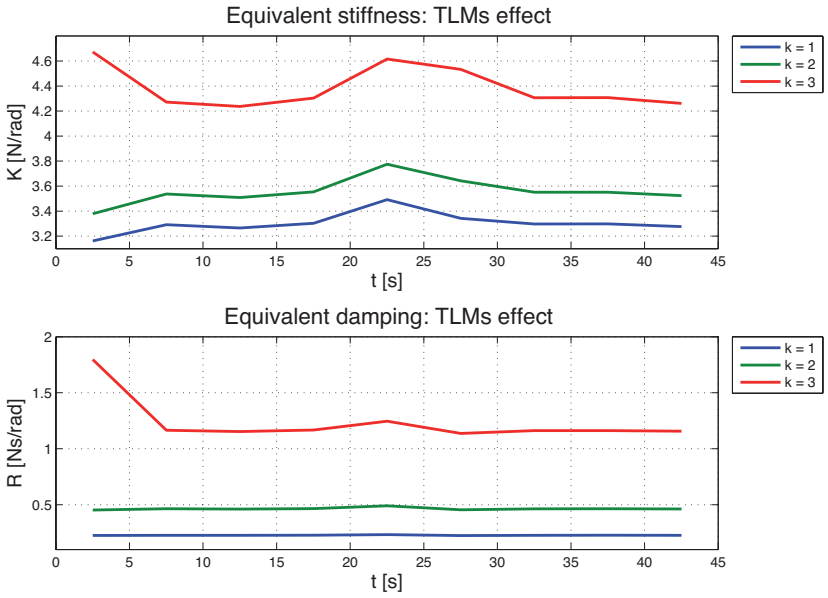

Figura 21: Effetto dei modi di attivazione a coppia nulla (TLAM) sull'impedenza equivalente del sistema biomeccanico

4

CONCLUSIONI E SVILUPPI FUTURI

Al centro di questo lavoro di tesi è stato posto l'obiettivo di definire una metodologia generale capace di stimare l'impedenza meccanica dell'arto superiore umano del pilota impegnato nel controllo di veicoli, sfruttando le potenzialità delle tecniche multibody e di ottimizzazione, che fosse in grado di valutare i contributi di una vasta gamma di geometrie del cockpit, di corporature del pilota, di parametri biomeccanici e fisiologici diversi, e di risolvere i problemi legati alle ridondanze del sistema meccanico equivalente, sia in termini di gradi di libertà eccedenti sia in termini di sovra-attuazione del sistema, dovuta alle forze muscolari.

Un modello multibody comprendente 4 corpi rigidi e 7 gradi di libertà è stato progettato e sviluppato specificamente per gli scopi suddetti, in grado di simulare il moto di omero, ulna, radio e della mano. L'azione di 25 muscoli del braccio e avambraccio è inclusa nel modello: ogni fascio muscolare è modellato tramite un attuatore viscoelastico monodimensionale.

La cinematica del sistema è invertita a tutti e tre i livelli: posizioni, velocità e accelerazioni, con una procedura in grado di risolvere la ridondanza al primo di questi livelli. La qualità della soluzione è controllata costantemente ai livelli successivi, attraverso ottimizzazioni vincolate successive.

La dinamica del sistema è poi invertita per ricavare le coppie ai giunti necessarie per garantire la cinematica ricavata al passo precedente, e un processo di minimizzazione vincolata dell'attivazione totale dei muscoli permette di ottenere le forze muscolari associate.

I risultati del modello sono stati messi a confronto con risultati sperimentali pubblicati in letteratura.

Per la stima delle caratteristiche di impedenza equivalente dell'arto, è stato sviluppato un approccio di tipo analitico, operante in condizioni di dinamica *congelata*, ovvero in condizioni in cui il sistema può essere linearizzato senza significative perdite di informazione.
Il metodo proposto è stato utilizzato per identificare l'impedenza associata al braccio di un pilota soggetto a test *PAO*, utilizzando dati sperimentali raccolti dal rotorcraft aeroservoelasticy research group del Dipartimento di Ingegneria Aerospaziale del Politecnico di Milano presso il Bibby Flight Simulation Laboratory, University of Liverpool.

Il concetto di Torque-Less Activation Modes, ovverosia di combinazioni lineari di coefficienti di attivazione che non producono variazione nella coppia ai giunti, ma capaci di variare l'impedenza meccanica, è stato introdotto e la sua possibile importanza relativa è stata valutata.

4.1 SVILUPPI FUTURI

Questo lavoro rappresenta un primo tentativo di affrontare il problema di identificazione dell'impedenza meccanica del pilota a partire da principi primi, ed è inteso quindi in senso esplorativo.
Diversi sviluppi futuri sono quindi possibili e auspicabili:

1. una conferma sperimentale relativa ai risultati ottenuti dal metodo proposto è necessaria per valutare la sua reale efficacia. La campagna sperimentale dovrà includere misurazioni EMG, dei fasci muscolari rilevanti, di un pilota che interagisce con un simulatore del veicolo;

2. la funzione di trasferimento relativa al comportamento passivo del pilota, soggetto a profili di accelerazione noti, dovrà essere estratta dal modello. Questo processo renderà possibile la valutazione critica di diverse geometrie dell'apparato di controllo, un processo questo che si rivelerebbe fondamentale in modo particolare in campo elicotteristico. Diverrebbe possibile la valutazione di differenti geometrie e disposizioni dei comandi in relazione alla loro propensione o meno nel generare situazioni pericolose per l'interazione pilota-velivolo.

3. il modello dell'arto superiore sarà inserito in un modello multibody rappresentante la dinamica del veicolo, per valutare in modo diretto la dinamica accoppiata pilota-veicolo;

4. l'impedenza dell'arto sarà stimata non solo come impedenza globale dell'intero braccio, ma come combinazione delle impedenze associate alle singole coordinate di giunto, per permettere una migliore adattabilità del modello a diversi soggetti;

5. un sistema di controllo in grado di attivare i fasci muscolari corretti per raggiungere un adeguato obiettivo in relazione al controllo del veicolo, dovrà essere sviluppato per riprodurre il contributo di impedenza associato alla risposta neurologica;

La realizzazione concreta di questi sviluppi è in corso di pianificazione presso il Dipartimento di Ingegneria Aerospaziale, Politecnico di Milano.

BIBLIOGRAFIA

[1] J. Ambrósio, C. Quental, B. Pilarczyk, J. Folgado, and J. Monteiro. Multibody biomechanical models of the upper limb. *IUTAM Symposium on Human Body Dynamics*, 2:4–17, 2011.

[2] A. A. Amis, D. Dowson, and V. Wright. Analysis of elbow forces due to high-speed forearm movements. *Journal of Biomechanics*, 13: 825–831, 1980.

[3] R. Barry Walden. A retrospective survey of pilot-structural coupling instabilities in naval rotorcraft. *Proceedings of 63rd AHS Annual Forum*, 2007.

[4] S. Buchanan, T., L. Delp, and J. A. Solbeck. Muscular resistance to valgous loads at the elbow. *Journal of Biomechanical Engineering*, 120:634–639, 1998.

[5] S.K. Charles and N. Hogan. Dynamics of wrist rotations. *Journal of Biomechanics*, 44:614–621, 2001.

[6] S. L. Delp, A. E. Grierson, and T. S. Buchanan. Maximum isometric moments generated by the wrist muscles in flexion-extension and radial-ulnar deviation. *Journal of Biomechanics*, 29:1371–1375, 1996.

[7] O. Dieterich, J. Götz, D.B. Vu, H. Haverdings, P. Masarati, M. Pavel, M. Jump, and M. Gennaretti. Adverse rotorcraft-pilot coupling: Recent research activities in europe. *Proceeding of 34th European Rotorcraft Forum*, pages 1–13, September 16-19 2008.

[8] M. Foumani, L. Blankevoort, C. Stekelemburg, S.D. Strackee, B. Carelsen, R. Jonges, and G.J. Streekstra. The effect of tendon loading on in-vitro carpal kinematics of the wrist joint. *Journal of Biomechanics*, 43:1799–1805, 2010.

[9] A. Fumagalli, G. Gaias, and P. Masarati. A simple approach to kinematic inversion of redundant mechanisms. *Proceedings of IDETC/CIE*, September 4-7 2007.

[10] B. A. Garner and M. G. Pandy. Musculoskeletal model of the upper limb based on the visible human male dataset. *Computer Methods in Biomechanical and Biomedical Engineering*, 3:96–126, 2001.

[11] B.A. Garner and M.G. Pandy. Estimation of musculotendon properties in the human upper limb. *Annals of Biomechanical Engineering*, 31:207–220, 2003.

[12] D. Gattamelata, E. Pezzuti, and P.P. Valentini. Accurate geometrical constraints for the computer aided modelling of the human upper limb. *Computer Aided Design*, 39:540–457, 2007.

[13] S.K. Gollapudi and D.C. Lin. Experimental determination of sarcomere force-length relationship in type-i human skeletal muscle fibers. *Journal of Biomechanics*, 42:2011–2016, 2009.

[14] T. Groot, H.J. Damveld, M. Mulder, and M.M. van Paassen. Effects of aeroelasticity on the pilot's phsychomoto behavior. *Proceedings of Atmospheric Flight Mechanics Conference and Exhibit*, August 21-24 2006.

[15] D. Hamel. Rotorcraft-pilot coupling: A critical issue for highly augmented helicopters. *AGARD*, CP-592, May 1996.

[16] H. Hashiguchi, S. Arimoto, and R. Ozawa. Control of a handwriting robot with dof redundancy based on feedback in task coordinates. *Journal of Robotics and Mechatronics*, 16, 2004.

[17] J. Hollerbach and K. Suh. Redundancy resolution of manipulators through torque optimization. *IEEE Journal of Robotics and Automation*, 3:308–316, 1987.

[18] K.R.S. Holzbaur, W.M. Murray, and S.L. Delp. A model of the upper extremity for simulating muscoloskeletal surgery and analyzing neuromuscular control. *Annals of Biomechanical Engineering*, 33: 829–840, 2005.

[19] G. Höne. Computer aided development of biomechanical pilot models. *Aerospatial Science and Technology*, 4:57–69, 2000.

[20] H. J. Huang and D. P. Ferris. Upper and lower limb muscle activation is bidirectionally and ipsilaterally coupled. *Medicine & Science in Sports & Exercise*, 41:1778–1789, 2009.

[21] Baillieul John. A constraint oriented approach to inverse problems for kinematically redundant manipulators. *IEEE International Conference on Robotics and Automation*, pages 1827–1833, March 31 - April 3 1987.

[22] A. Keckeméthy and A. Weinberg. An improved elasto-kinematic model of the human forearm for biofidelic medical diagnosis. *Multibody System Dynamics*, 14:1–21, 2005.

[23] M.A. Lemay and P.E. Crago. A dynamic model for simulating movement of the elbow, forearm and wrist. *Journal of Biomechanics*, 29:1319–1330, 1996.

[24] L.R. Lieber and T.J. Burkholder. *Biomechanics: Principles and Applications*. CRC Press, 2008.

[25] C.C. MacAdam. Understanding and modeling the human driver. *Vehicle System Dynamics*, 40:101–134, 2003.

[26] J.R. Mayo. The involuntari participation of a human pilot in a helicopter collective control loop. *Proceedings of 15th European Rotorcraft Forum*, pages 81.001–012, 1989.

[27] R.V. Mayorga and A.K.C. Wong. A singularities avoidance method for the trajectory planning of redundant and nonredundant robot manipulators. *IEEE International Conference on Robotics and Automation*, pages 1707–1712, March 31 - April 3 1987.

[28] D.T. McRuer and R.E. Smith. Pio - a historical perspective. *AGARD*, AR-335, 1995.

[29] C.P. Neu, J.J. Crisco, and S.W. Wolfe. In vivo kinematic behaviour of the radio-capitate joint during wrist flexion-extension and radioulnar deviation. *Journal of Biomechanics*, 34:1429–1438, 2001.

[30] J. C. Otis, R. F. Warren, S. I. Backus, and T.J. Santner. Torque production in the shoulder of the normal young adult male. the interaction of function, dominance, joint angle, and angular velocity. *American Journal of Sport Medicine*, 18:119–123, 1990.

[31] E. Pennestrì, R. Stefanelli, P.P. Valentini, and L. Vita. Virtual musculo-skeletal model for the biomechanical analysis of the upper limb. *Journal of Biomechanics*, 40:1350–1361, 2007.

[32] R.S. Sharp. On steering wobble oscillations of motorcicles. *Proceedings of Institution of Mechanical Engineers*, 218 Part C: Journal of Mechanical Engineering Science:1449–1456, 2004.

[33] S. Sullivan, N.A. Langrana, and S.A. Sisto. Multibody computational biomechanical model of the upper body. *Proceedings of IDETC/CIE*, pages 1–6, March 31 - April 3 2005.

[34] M.M. van Paassen. *Biophisics in aircraft control*. PhD thesis, Delt University of Technology, 1994.

[35] J. Venrooij, D. A. Abbink, M. Mulder, M. M. van Paassen, and M. Mulder. Method to measure the relationships between biodynamic feedthrough and neuromuscular admittance. *IEEE Transactions on Systems, Man. and cybernetics — Part B*, 41:1158–1169, 2011.

[36] J. M. Winters and D. G. Kleweno. Effect of initial upper limb alignment on muscle contributions to isometric strenght curves. *Journal of Biomechanics*, 26:143–153, 1993.

[37] F.E. Zajac. Muscle and tendon: properties, models, scaling, and application to biomechanics and motor control. *CRC Critical Reviews in Biomedical Engineering*, 17(4):359–410, 1989.

CONTENTS

THESIS 1

1 INTRODUCTION 3
- 1.1 Human controller modeling 4
- 1.2 Rotorcraft Pilot Coupling 5
- 1.3 Multibody model of the human arm 6
- 1.4 State of The Art 8
- 1.5 Thesis overview 10

2 BIOMECHANICAL MULTIBODY MODEL 13
- 2.1 Upper limb anatomy 13
  - 2.1.1 Anatomical terminology 13
  - 2.1.2 Upper limb osteology and arthrology 14
  - 2.1.3 Upper limb myology 20
- 2.2 Model geometry and constraints 36
  - 2.2.1 Algebraic constraints 38
- 2.3 Muscle models 40
  - 2.3.1 Structure and microstructure of skeletal muscles 42
  - 2.3.2 Muscle viscoelastic properties 43
  - 2.3.3 Hill-type muscle models 46
  - 2.3.4 Zajac approximations 50

3 INVERSE DYNAMICS 57
- 3.1 Kinematics inversion 57
  - 3.1.1 Redundant mechanism 57
- 3.2 Complete kinematics inversion for a redundant system 62
  - 3.2.1 Positions problem resolution 62
  - 3.2.2 Velocity problem resolution 64
  - 3.2.3 Accelerations problem resolution 66
- 3.3 Example: Planar 3-link robot 67
  - 3.3.1 Geometrical constraints 68
  - 3.3.2 Position 69
  - 3.3.3 Velocity 71
  - 3.3.4 Acceleration 73
  - 3.3.5 Tracking example 73
- 3.4 Inverse dynamics 77
- 3.5 Muscle forces identification 78

3.5.1 Matrix [B] 81
3.5.2 Joint space projection matrix 83
3.6 Model Validation 85
3.6.1 Maximum joint moments 85
3.6.2 Muscular activation 95
4 UPPER LIMB IMPEDANCE 99
4.1 Methodology 99
4.2 Torque - less modes of activation 102
4.3 Rotorcraft pilot's arm impedance identification 104
4.3.1 PAO testing at University of Liverpool 104
4.3.2 Activation coefficients 109
4.3.3 Musculoskeletal system impedance 110
4.3.4 Effect of Torque Less Activation Modes 114
4.3.5 Pilot's body type effect 117
5 CONCLUSIONS AND FUTURE DEVELOPMENTS 121
5.1 Future Developments 122

BIBLIOGRAPHY 125

LIST OF FIGURES

Figure 1 Posterior view of the right scapula. Adapted from [51] 15

Figure 2 Anterior view of the right humerus. Adapted from [51] 17

Figure 3 Posterior view of the left humerus. Adapted from [51] 18

Figure 4 Bones of the forearm. Anterior view (left) and posterior view (right). Adapted from [51] 19

Figure 5 Superficial muscles of the posterior part of the neck, trunk and shoulder area. Adapted from [51] 21

Figure 6 Superficial muscles of the ventral part of the trunk and the arm. Adapted from [51] 22

Figure 7 Dorsal muscles of the scapula and triceps. The spine of the scapula has been sectioned close to its lateral extremity. The acromion and the coroidal process have been removed. The humerus is laterally rotated and the forearm is pronated. Adapted from [51] 23

Figure 8 Deep muscles of the ventral part of the trunk and of the arm. Adapted from [51] 25

Figure 9 Superficial flexors of the forearm. Adapted from [51] 32

Figure 10 Deep flexors of the forearm. Adapted from [51] 33

Figure 11 Superficial extensors of the forearm. Adapted from [51] 34

Figure 12 Deep extensors of the forearm. Adapted from [51] 35

Figure 13 Model schematics. A node is placed at each bones', or set of bone's in the case of the hand, proximal epixondyle. 36

Figure 14 Myofibrils are long chains of sarcomeres. Below, schematics for sarcomere contraction. In red, actin proteins, while in black myosin proteins are represented. When the sarcomere is activated, myosin terminations bend backwards, making the actin shells slide and shortening the sarcomere. 43
Figure 15 Force-length relationship for the sarcomere. Circles represent data collected by Gollapudi et al. and published in [16] 44
Figure 16 Force-velocity relationship for the sarcomere. 45
Figure 17 Hill's model for contraction dynamics scheme. Muscle force F is the product of the effect of a contractile element CE, in parallel with a first elastic element PEE and in series with another elastic element SEE. Since tendon compliance is generally dominant, SEE can often be neglected. 47
Figure 18 Simplified schematics for Hill-type model used. Pennation angle is being disregarded, as well as cross-bridge elasticity. Muscle and tendon elasticity is included in parallel elastic element PEE. 50
Figure 19 Dimensionless muscle force as a function of muscle length ratio e lengthening velocity. 52
Figure 20 Active contribution of sarcomere force for different activation levels, with null constant contraction velocity. The lower curve corresponds to $a = 0.2$ and the higher one to $a = 1$, with 0.2 steps. 55
Figure 21 Active contribution of sarcomere force for different activation levels. Sarcomere length is kept constant at l_o. The lower curve corresponds to $a = 0.2$ and the higher one to $a = 1$, with 0.2 steps. 55
Figure 22 Schematics of the planar manipulator model analyzed in its initial position. 67
Figure 23 Ergonomic spring force as a function of relative angle between two nodes. 71
Figure 24 Imposed trajectory of the end effector of Link 3 in the X-Y plane. 74
Figure 25 Imposed position, velocity and acceleration components of the end effector of Link 3. 75

Figure 26 Relative angles between the links, with different initial prestrain applied to the non - linear elastic elements that represent the discomfort functions. The solution changes to find the new local minimum of the potential energy stored in the springs. 76
Figure 27 Solutions comparison for the planar 3 link robot, subjected to the action of rotational springs with different initial prestrain. 76
Figure 28 Shoulder abduction isometric moment estimated by the model, in comparison to data published Holzbaur [21], Garner and Pandy [13] and Otis [41]. The abduction angle is reported here considering the arm rest position alongside the body corresponding to 0°, and the full flexion position to an angle of 90°. 87
Figure 29 Shoulder flexion isometric moment estimated by the model, in comparison to data published Holzbaur [21], Garner and Pandy [13] and Otis [41] and Winters [52]. The flexion angle is reported here considering the arm rest position alongside the body corresponding to 0°, and the full flexion position to an angle of 90°. 89
Figure 30 Elbow flexion isometric moment estimated by the model, in comparison to data published Holzbaur [21], Amis [2] and Buchanan [4]. The flexion angle is reported here considering the 0° angle corresponding to the forearm completely extended, while the maximum flexion occurs for an angle of 140°. 90
Figure 31 Forearm supination isometric moment estimated by the model, in comparison to data published Holzbaur [21] and Garner [13]. The pronation angle is reported here considering the -90° angle corresponding to the forearm completely supinated, while positive angles correspond to a pronated forearm. 91

Figure 32 Wrist flexion isometric moment estimated by the model, in comparison to data published Holzbaur [21] and Delp [9]. Negative angles corresponds to the wrist completely flexed, while positive angles correspond to a wrist extension. 93
Figure 33 Wrist deviation isometric moment estimated by the model, in comparison to data published Holzbaur [21] and Delp [9]. A -90° angle corresponds to the wrist completely flexed, while positive angles correspond to a wrist extension. 94
Figure 34 The experimental setup used by Huang et al to measure EMG activity of upper limb muscles during physical exercise. Source: [23] 95
Figure 35 EMG activity of the four muscle bundles measured by Huang et al. [23] compared with activation coefficients estimated by the model. The level of accuracy is not even between the muscles, but the general tendencies are captured. Without indications on EMG activity corresponding to maximum isometric force, it is not possible to confront the absolute values of the quantities. 98
Figure 36 Picture of the rotorcraft simulator of the Bibby Flight Simulation Laboratory, University of Liverpool (UK). The pilot is showing the 0%, 50% and 90% collective control positions, in a., b. and c., respectively. Source: [32] 104
Figure 37 Cockpit geometry in the multibody model. 105
Figure 38 Collective control inceptor's angular position time history used for the prescribed motion of the handle in the multibody model (above), and vertical displacement of the rotorcraft (below). The z-axis is assumed positive in the upward direction. 107
Figure 39 Model in its initial position. Thick lines correspond to elements representing the muscles, while thin lines represent their offests with respecto to the nodes. 108

Figure 40 Joint torques of the pilot's upper limb, obtained by dynamics inversion of the multibody model, fed with the time history of the collective control's inceptor. 109
Figure 41 Activation parameters of the muscles of shoulder during the maneuver. Only the most active muscles are shown. It can be noted that the correct bundles are active, and that to a modification of the joint torque corresponds a modification of the activation patterns of the muscles acting on the joint itself. 111
Figure 42 Activation parameters of the muscles of the forearm during the maneuver. 112
Figure 43 Intrinsic impedance of the upper limb, calculated every 5 s starting from $t = 2.5$ s 113
Figure 44 Torque Less Activation Modes for the pilot upper limb's muscles, in the reference configuration of the instant of time $t = 27.5$ s. The numbering of the muscles follows that of Tables 5 and 6 115
Figure 45 Torque Less Activation Modes effect on the impedance of the biomechanical system. 116
Figure 46 Impedance parameters for pilots of three different body types: the 118

LIST OF TABLES

Table 1 Parameters of several muscles of the upper limb. Source: [14] 7
Table 2 Different types of synovial joints and their algebraic approximations 39

Table 3 Inertial properties of the rigid bodies in the model. All masses and moment of inertia are considered as accounting for both the bones and their related muscles. Data reported here is valid for 50% percentile male, with height 180 cm and weight 80 kg, according to regression equations of [7, 8] 40
Table 4 Geometrical properties of the model. All the quantities are expressed in millimeters, in the reference frame of the body to which they refer to. 41
Table 5 Muscle model parameters for muscle bundles present in the model. Peak isometric force and optimal lengths are taken from [21], pennation angles from [28, 21, 30]. 53
Table 6 Muscle model parameters for muscle bundles present in the model – continuation. 54
Table 7 Planar 3 link mechanism inertial and geometrical parameters. Initial orientation is given by θ_{i0} and is expressed with reference to the global reference system. 68
Table 8 Muscle bundles in the model, that act on abduction and adduction of the shoulder. 88
Table 9 Muscle bundles in the model, that act on the flexion and the extension of the shoulder. 89
Table 10 Muscle bundles in the model, that act on the flexion and the extension of the forearm. 91
Table 11 Muscle bundles in the model, that act on the pronation and the supination of the forearm. 92
Table 12 Muscle bundles in the model, that act on the flexion and the extension of the wrist. 93
Table 13 Muscle bundles in the model, that act on the deviation the wrist. 95
Table 14 Pilot parameters used in the simulations. 106
Table 15 Parameters of pilots of different body types, used in the simulation. 117

THESIS

1

INTRODUCTION

In modern vehicle design, broader and increasing attention is being given to pilot modeling and, more widely, to the interaction between the human controller and the vehicle itself.
The general topic of understanding how a human driver, rider or pilot behaves and transferring that behavior into a mathematical form encompasses a great variety of engineering fields, that cannot in general be considered separately.

Pilot and vehicle interact in such a way that is generally impossible to treat them as separate systems: they have to be considered, in a sense, a single entity. The behavior of the vehicle depends on the inputs that it receives from the pilot, and conversely pilot behavior is influenced by the reactions that are exchanged between him and the vehicle.

Often, this last kind of relationship develops at the perceptual and psychological level: e.g. the driver of a car will approach a slalom maneuver with a higher average speed when he is not subject to motion feedback, than when he is actually put in an environment that simulates the accelerations he would receive from the car during the maneuver [48].

In some cases, though, a mechanical type of interaction is possible and observed: vibrations of the vehicle structure can act on the pilot in such a way to cause involuntary control actions, determined by the mechanical response of the body. Both passive and active biomechanics of the human body, and particularly of the pilot arm, play a fundamental role in the manifestation of self-sustaining oscillations that can lead to dangerous conditions in different human-machine interactions.

In the field of ground vehicles, the strongest coupling between human and vehicle is found in the control of motorbikes, where inertia and mechanical impedance of the rider strongly contribute to the dynamical behavior of the bike-rider system, and particularly its stability.
As an example, rider action on the handlebars can significantly change the frequency associated with wobble mode resonance, and thus have an impact on bike stability [43].

1.1 HUMAN CONTROLLER MODELING

The design process for ground vehicles, aircraft and rotorcraft has become more and more sophisticated while at the same time manufacturers' tendency is to eliminate or reduce, whenever possible, the need for direct testing on prototypes, for reasons related to cost saving. The strong development that human pilot numerical modeling has received in recent years stems from this two seemingly contrasting needs.

MacAdam proposed in 2003 [31] a set of characteristics that has to be included in a vehicle driver model, that can be certainly generalized to include pilot and rider models with some minor modifications:

1. use of preview for sensing the upcoming control requirements
2. adaptation provision so that alteration to the controlled vehicle dynamics and operating conditions can be approximated or accounted for within the pilot/driver model
3. exhibition of a linear regime "crossover model" behavior in the immediate vicinity of the crossover frequency. The crossover model was first proposed by MrRuer in 1967 [36].
4. presence of an internal vehicle model - or equivalent capability - within the structure of the driver model in order to help estimate future controlled vehicle responses
5. provision for modification of path inputs or path planning
6. previewed path adjustment capabilities and strategies to account for skill-related abilities
7. provisions for processing incoming sensory signals to account for neural delays, thresholding, rate limiting, and dynamical properties of individual channels
8. neuromuscular filtering elements for output channels

Pilot modeling, especially in the ground vehicle field, has focused primarily on the first six traits, mainly because vibration from the vehicle structure are less subject to produce a reaction by driver's structures significant enough to be transferred into adverse control

inputs, since driver action augmentation is very much less significant than that, e.g. of an aircraft or rotorcraft.

Moreover, the frequencies associated with engine forces and structural vibration of a vehicle chassis are generally outside the range interested to biomechanical response. Aside from racing vehicles, reactions due the rigid motion of the chassis allowed by the suspension system are not likely to be significant enough to be a relevant forcing term for the driver's body vibration.

The majority of the attention is thus put on the neural input/output behavior of the human controller, hence to his parameters as related to control aspects. A great deal of effort is spent in the determination of which inputs the human brain selects as meaningful, and of which control techniques can better approximate the transformation this parameters are subject to in becoming the neural output, and with which time delays, thresholding and frequency contributions.

Nonetheless it is becoming fundamental in various aspects of vehicle design to be able to model in an efficient yet sufficiently precise way the forces that the human controller is able to apply to the mechanical system with which he interacts. Ergonomics, cockpit design and control system design, especially when specifically designed for differently abled people, offer some clear examples.

Another interesting example is represented by APC (Aircraft Pilot Coupling) and RPC (Rotorcraft Pilot Coupling). The two phenomena are related to one another in the sense that aeroelastic vibratory behavior properties of the aerial vehicle interact with the biomechanical properties of the pilot to produce unwanted, involuntary and possibly self-sustaining vibrations of the system.
Rotorcraft, at the same time, represent a critical case for flight security and an interesting testing bed for the problems highlighted here, for the reason that frequencies relative to engine and drivetrain dynamics (1st torsion mode), flight control systems dynamics, rigid rotor dynamics, and airframe dynamics all are in the range of pilot biomechanical response.

1.2 ROTORCRAFT PILOT COUPLING

Modern flight control systems can lead to unexpected and unintended oscillations or divergences of the pilot-rotorcraft system, and rise to

hazardous and even catastrophic events in some cases [37, 18, 3]. Two kinds of destabilization and/or pilot participation in the control loop are known:

- PIO: Pilot - Induced Oscillations
- PAO: Pilot - Assisted Oscillations

Oscillations of the first kind manifest themselves when the pilot introduces a phase lag or moves the controls in the wrong direction, possibly in response to misleading cues, and they are not always detrimental of flight safety. They need an active involvement of the pilot in the control loop, so if he releases the controls or change his action in other fashion, PIO will cease.

Those of the second kind are a result of completely involuntary participation of the pilot in the control loop, and are thus more related to pilot biomechanics and biodynamics, heavily dependent from his body type, experience, and neuromuscular system characteristics [34] [17].

Conventional approach to the modeling of this kind of feedback is to measure control displacements while the pilot is subject to known vibrations, imposed by means of a shaker table, and build a pilot transfer function that represents his impedance characteristics.
A more sophisticated way to achieve the same goal is to measure pilot behavior in a controlled simulator environment. However, such an approach has some restrictions: the most evident being that transfer functions obtained are strongly dependent on cockpit geometry and control dynamic properties, and cannot be used for extrapolation.

1.3 MULTIBODY MODEL OF THE HUMAN ARM

More extensively, the limitations that can be attributed to the transfer function modeling of the human biomechanical behavior arise from a wide variability of parameters upon which it depends

- pilot size (height and weight)
- pilot and cockpit geometrical configuration (i.e. limb rest position)
- subjective pilot attitude

Table 1: Parameters of several muscles of the upper limb. Source: [14]

Muscle	G&P[a] (2003)	Wood (1989)	Veeger (1991)	Bassett (1990)	Winters (1988)	An (1981)	Veeger (1997)
Volume [cm^3]							
Triceps	619.99	298.24	99.70	152.00	283.02	152.60	397.00
Biceps	365.84	108.15	111.20	128.00	113.21	64.20	128.00
Physiological Cross Section Area (PCSA) [cm^2]							
Triceps	76.30	11.40	6.84	4.61	–	18.80	13.81
Biceps	25.90	3.39	6.29	4.80	–	4.60	5.34

a Garner & Pandy

- task performed (MTE, Mission Task Element)
- any additional workload the pilot is being subjected to

Since the force-generating capabilities of the human body strongly depend upon the configuration of the environment in which it operates, lumped parameter models derived from testing (i.e. human controller transfer functions) cannot be extended outside the domain in which they were generated. Environment configuration here is intended in a very broad sense: it can be the geometrical disposition of the controls and of the cockpit with respect to the controller position, the feedback characteristics of the controls, the vibration behavior of the structure, etc.

Secondly, the variability associated with biomechanics parameter values within the different human individuals plays a fundamental role and can be a great source of uncertainty. As an enlightening example, in Table 1 an extract of the work published in [14] is shown. Parameters regarding muscles in the upper limb found in literature and estimated by Garner and Pandy are compared.

It is evident, just by looking at the data, how these parameters can vary greatly from one research to another. Every claim for generalization of an approach based upon the frequency response of a necessarily small sample of individuals, has to deal with this variability, which is likely to cause poor data correlation [22].

Hence the multibody approach comes into the picture, offering an extremely powerful and even more flexible framework in which to operate. Multibody analysis allows to easily account for the specific geometry-related, vibrational and feedback properties of the environment and also, at least in principle, the biomechanical ones of the human controller.
In the design stage, when different configurations of the structure of the vehicle, together with different control dispositions and dynamics, are tested and evaluated, the possibility of doing so without having to invest a significant amount of time and resources in specific tests, is obviously a sought target. It can be accomplished by devolving to numerical simulations a wide range of preliminary tests, and leaving to physical testing on prototypes only the validation of restricted range of numerical results.

Multibody modeling offers a further advantage, in being able to produce the full set of physical quantities related to simulated system dynamics. That is a major distinction from physical testing, where for obvious reasons the data collection is limited to several representative and pre-determined signals.
Thus, greater insight into the behavior of the physical systems involved (in this case, the vehicle and the human controller) can generally be obtained by multibody simulation.

The choice to focus on modeling the human arm can be justified by noting that the upper limb represents the most complex element of the human body that it is actively involved in the generation of control input, if the controller is being assigned to a passive part in the control loop (in an active case, the brain would take the supreme spot, as obvious). Thus, while the rest of the body is probably well approximated by a single, lumped parameters element, the arm needs a special treatment. It is also to be noted that the upper limb can change geometrical and dynamical configuration (i.e. dynamical state) in a greater extent with respect to the rest of the body.

1.4 STATE OF THE ART

At present, various attempts have been made to model the upper limb through multibody techniques, mainly for purely biomechanical and biofidelic models, aimed at obtaining reliable information from a med-

ical and physiological point of view [26, 1, 45, 28]. The required level of accuracy is achieved by a detailed description of each articular joint, sometimes deformable and with migrating rotation axes [15], a comprehensive set of elements modeling muscle behavior, with independent activation dynamics, and are generally fed by kinematic data acquired by accurate measurements to perform inverse dynamics simulations and obtain muscle activation patterns.

Multibody modeling of the human body, on the other hand, applied to a human controller, is being applied primarily to comfort - related problems, at least in the ground vehicle field. Human body models tend also to be lumped-parameters models, in the sense that they do not include muscle - modeling elements, but only elements that represent the mechanical impedance of the whole body part (e.g. the forearm).

In the aeronautical engineering field, several further attempts to model the biomechanical properties of the pilot body, as related to the pilot-aircraft and pilot-rotorcraft coupling, have been made [22, 17, 47]. In many cases, though, a mechanical equivalent of the human body is sought, utilizing parameters identified statically or by specific testing to extract dedicated linear transfer functions.

A general procedure, aimed at extracting the relevant impedance data from first principles, without the need of referring to a single condition, has been delineated in [10], developed in the framework of the *GARTEUR*[1] organization.
A multibody model of the upper limb is used to compute activation patterns for a given hand motion, and impedance of each articulation is estimated in terms of the relationship between joint torque and joint motion.

Two different kinds of redundancies raise the complexity of the problem: the first one is related to kinematics, as the human arm is generally considered as a 7 degrees of freedom system, and a maximum of 6 degrees of freedom can be imposed to the hand.
The second one is related to the generation of joint torques: since muscle bundles are incapable of generating compressive forces, they can generate torque about a joint only by working in antagonist couples. Furthermore, they typically work in more than one couple to produce torque about the same axis, making the system even more redundant.

The entire procedure can be outlined in four steps

1 Group for Aeronautical Research and Tecnology in EURope: www.garteur.eu

1. inverse kinematics of an undetermined system, needed to estimate articular joint motion from measured or imposed motion of the hand, considered as the end-effector of a manipulator mechanism
2. inverse dynamics of a fully determined system aimed at the computation of joint torques
3. optimization procedure applied to muscle activation, to compute muscle forces that can generate joint torques
4. computation of mechanical impedance parameters for each articulation

Points 1 and 3 need some kind of redundancy - resolving algorithm or closure form to be carried to completion. The work presented here stems from this approach, representing its implementation, and its further development.

It is to be noted though that due to the aforementioned sources of uncertainty and variability, the method proposed here does not claim to deterministically define the pilot-vehicle relationship, or the biomechanical transfer function of the pilot, but aims to be an assessment tool for the source of variance that the current human controller's transfer functions exhibit.

Through this procedure, a determination of the relative importance between the causes of poor data correlation of the current preferred method is sought, to make it possible to concentrate on those parameters which can be identified as the most problematic. A greater comprehension of the phenomena involved in the coupled human-vehicle or, more generally, human-machine interaction is also atop of the priorities that drove the attempt to implement this procedure.

1.5 THESIS OVERVIEW

In Chapter 2, the anatomical structures of the human upper limb are presented, both from an arthrological (i.e. related to the skeletal structure and the articular motion) and a myological (i.e. related to the muscles and their functions) point of view. Their critical analysis leads to the definition of the geometry and the choice of algebraic constraints of the multibody model, and also to the definition of the constitutive

law of the deformable elements representing the skeletal muscles.

In Chapter 3, methods developed for the inversion of the system kinematics and dynamics are presented. The optimization technique used to find muscular activations is also shown and the results obtained by each method are exemplified and compared with experimental data published in the literature.

In Chapter 4 the procedures developed and exploited for the identification of the impedance characteristics of the upper limb are shown, and experimental data collected by the research group on rotorcraft aeroservoelasticity of the Politecnico di Milano, at Bibby's Flight Simulation Laboratory, University of Liverpool, was used to estimate the equivalent impedance of the pilot's upper arm.

In Chapter 5, conclusions and future developments are summarized.

2

BIOMECHANICAL MULTIBODY MODEL

In this chapter, the multibody model of the upper limb developed for the purposes of this work is described. It is necessary, for obvious reasons, to premise some fundamental notions of human anatomy, regarding the general terminology and the aspects related specifically to the upper limb.

It will indeed be shown that to correctly define a *musculotendon actuator*, i.e. the element that reproduces both the elastic properties and the active force generation properties of a muscle bundle, a set of parameters has to be defined: the dependencies of the force generated by factors such as muscle and tendon length, muscle contraction velocity and voluntary activation are functions, are functions of the geometrical disposition of the bones to which they connect.

More specifically, the positions of the origin and attach point of each muscle are of great importance, as they influence the arms of muscle forces with respect to articular joint moments. They have thus to be chosen accurately in a functional sense, and not only in an anatomical one. To be able to do that, a fundamental knowledge of the actions performed by each muscle is needed.

A subsequent section shows the anatomical aspects are translated into the geometry and the choice of constraints in the multibody model.

The last section contains information about the physiology and biomechanics of human muscles, and explains the choice of the muscle model utilized.

2.1 UPPER LIMB ANATOMY

2.1.1 *Anatomical terminology*

Every science field has its own terminology, and anatomy certainly does not fall behind in this aspect. It is thus necessary to introduce some basic nomenclature, related to the anatomical reference systems and directions.

Conventionally, every anatomical description refers to the body in the so called *anatomical position*: the body is erect, facing the observer, with the palms facing the observer as well.

Directions are defined by means of three orthogonal planes: the *medial* or *sagittal plane*, a vertical plane that divides the body into right and left halves.
The *frontal plane* plane subdivides the body into an *anterior* (closer to the observer) and a *posterior* halve.
Every plane orthogonal to these two is a *transverse* or *horizontal* plane, that separates *cranial* or *superior* from *caudal* or *inferior* structures.

Structures closer to the medial plane are called *medial*, while structures farther from the plane are called *lateral*. Structures closer to the observer are *anterior* structures, and conversely structures farther from the observer are *posterior* structures.

When looking at a limb, the direction that identifies structures closer to the body, along the limb axis, is the *proximal direction*, while its opposite is the *distal direction*. A movement that brings the limb extremity in lateral direction is called *abduction*, opposite to the *adduction*.
A rotation that moves a point situated upon the anterior surface of the upper arm toward the body is a *medial rotation*, opposite to the *lateral rotation*.
Rotating the forearm about the elbow so that the hand is brought closer to the shoulder constitute an elbow *flexion*, while bringing the hand away from the shoulder will produce an elbow *extension*.
A rotation of the hand so that the palm will be brought toward facing the medial plane constitute a *pronation* of the hand and the forearm, while a *supination* of represents its opposite.

2.1.2 *Upper limb osteology and arthrology*

The upper limb is a very complex structure made of 32 bones and their relative muscles. Since the scope of this work is to model situations in which finger movements are inessential, the hand can be considered as a single body, which represents an important simplification due to the fact that the hand complex is alone composed by 27 bones and the related structures.

Considering the limb and the shoulder from its proximal end (the shoulder complex), to its distal end (the hand), the bones encountered

are the *clavicle*, the *scapula*, the *humerus*, the *radius*, the *ulna*, and the hand complex.

The joints that connect the different bones are *synovial* joints: the surfaces of the ends of the bones are coated with an elastic tissue called *ialine cartilage*, and can slide into a capsule in which a lubricant is present, the *synovial fluid*, that provides sustain, removes the friction, and nourish the cartilage.

The clavicle, the scapula and the humerus are joint together at the shoulder complex. The scapula is a flat, triangular bone with a broadly concave anterior surface (the *subscapular fossa*) that joins medially with the clavicle and laterally with the humerus, through the *glenoid fossa*, situated at the lateral end. A large, triangular process, the *acromion*, overhangs the glenoid fossa and, together with part of the *coracoid process*, provides stabilization to the superior part of the shoulder.

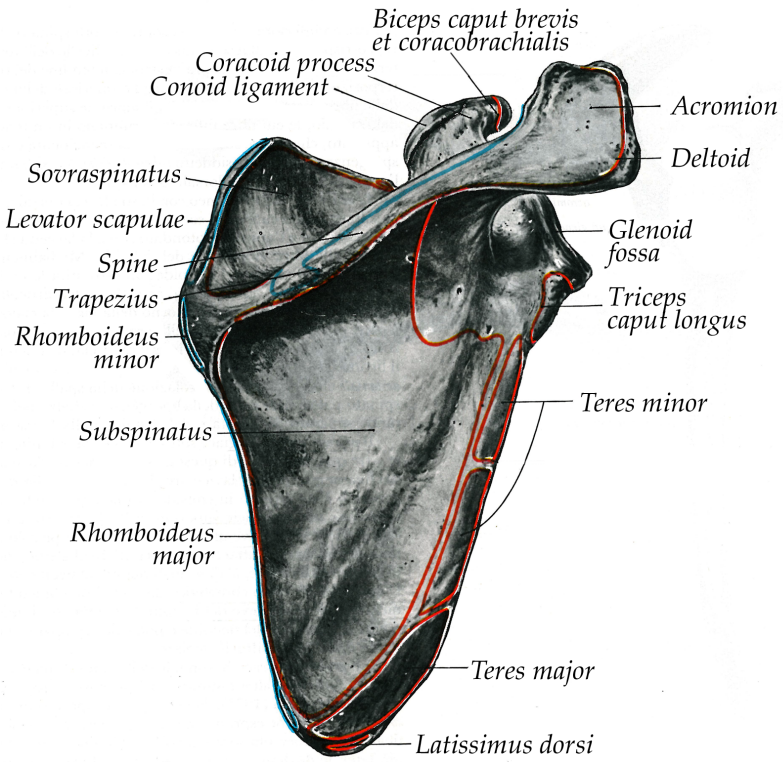

Figure 1: Posterior view of the right scapula. Adapted from [51]

Stabilization is needed because the shoulder is a weak joint that derives its stability from the muscles that surrounds it rather than from the geometrical shape of the connecting bones' sections. In fact, the convexity of the proximal end of the humerus, the *head*, is much more pronounced that the concavity of the glenoid fossa. This geometry permits an ample range of movements, eased by the low friction properties of the synovial joint.

The head of the humerus and the corresponding surfaces of the acromion and the coracoid process thus form a synovial joint that presents a spherical surface (the humerus head) that can rotate inside a concave housing, namely an *enarthrosis*. Allowed movements are

- abduction and adduction of the humerus with respect to the body
- medial and lateral rotation of the humerus
- flexion and extension of the humerus

The clavicle is an oblong, S-shaped bone that connects the subscapular fossa of the scapula to the sternum. Its medial end, saddle-shaped, connects with the clavicular notch of the menubrium. The resulting articulation is a *saddle* synovial articulation, that allows rotations in the transverse and vertical planes, and also a modest rotation about the clavicle long axis (up to about 30°.
At its lateral end, as already indicated, it connects to the acromion, forming the *acromioclavicular* joint.
In this kind of synovial joint, the two surfaces that interact are almost planar, and only gliding movements in the common plane of the two are permitted.

At the distal end of the humerus, the *epicondyle*, the elbow represents the connection of this bone with the radius and the ulna. In the elbow, three different joints are held together by a synovial capsule: the *humeroulnar joint*, the *humeroradial joint* and the *proximal radioulnar joint*. The joint is therefore a *composite* synovial joint.

On the distal end of the humerus, two processes can be observed: one, the *trochlea*, of roughly cylindrical shape, occupies the anterior, inferior and posterior faces of the medial part of the inferior extremity, and it is embraced by the interior surface of the *olecranon*, a C-shaped process at the proximal end of the ulna, when the arm in extended.
The ulna can thus rotate about the trochlear axis, and move slightly in

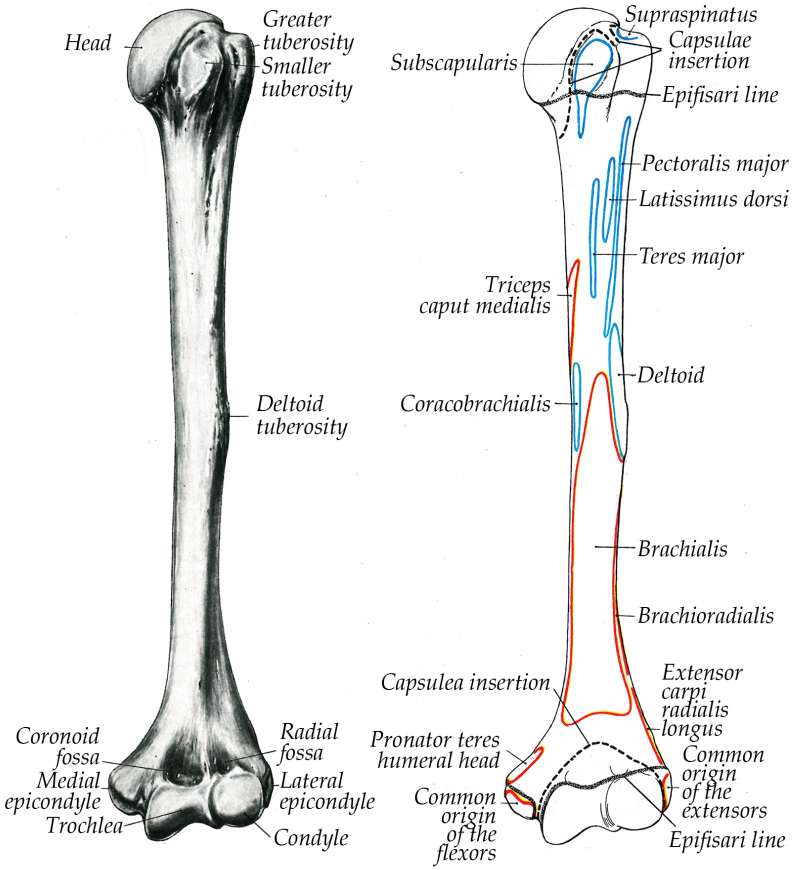

Figure 2: Anterior view of the right humerus. Adapted from [51]

distal direction when full flexion of the arm and pronation of the hand are reached [26].

Aside and medially from the throchlea, the *capitulum* is connected to a disc-shaped, slightly convex surface at the proximal end of the radius, the *radius head*. All three rotations of the radius with respect to the humerus are thus permitted by this joint.

The head of the radius is held firmly against the *radial notch*, i.e. a narrow, oblong depression on the lateral side of the proximal end of the ulna, the *coronoid process*. This joint allows only the rotation of the radius about the axis of symmetry of the radial notch. The *orbicular ligament* encircles the radial head to ensure the stability of the connection. This type of joint takes the name of *trochoid joint* or *pivot joint*.

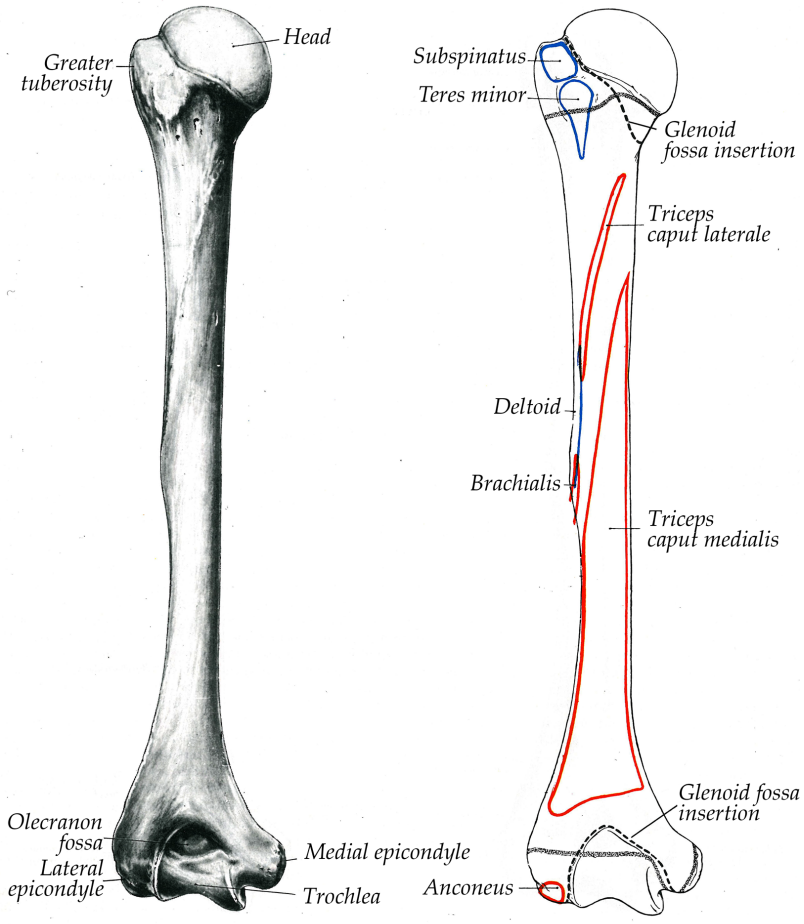

Figure 3: Posterior view of the left humerus. Adapted from [51]

At their distal ends, the ulna and the radius connect with the *distal radioulnar joint* with another trochoid joint, this time connecting the convex distal end of the ulna with a depression of the radius, the *ulnar notch*. Thus, the radius can again rotate about the axis of the notch.

Normally, the prono-supination of the hand is considered as a rotation of the radius about an axis that passes through the center of its proximal end (the head) and by the point of connection between the ulna and the articular disc at the distal end. This representation is, however, not entirely correct, since the ulna is not fixed during radius rotation; on the contrary, its inferior extremity moves on a curve: posteriorly and lateraly during pronation, and frontally and medially during supination. Thus, the axis of rotation moves laterally during pronation,

and medially during supination.

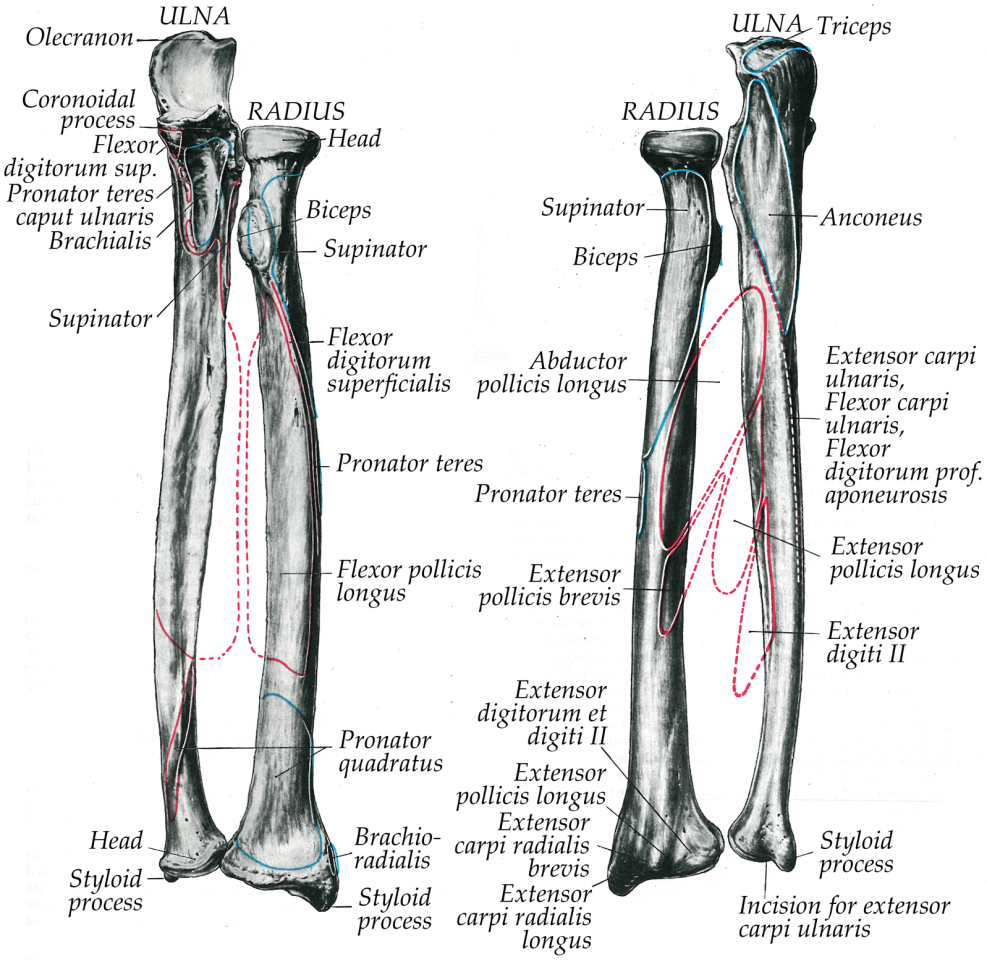

Figure 4: Bones of the forearm. Anterior view (left) and posterior view (right). Adapted from [51]

The distal end of the radius is connected to the hand through the *radiocarpal* joint, a bi-axial, *ellipsoidal* synovial joint. On the hand side, three carpal bones take part in the joint: the *scaphoid*, the *lunate* and the *triquetrum*. The surface generated by the radium extremity together with a triangular fibrocartilaginous element, the *triangular fibrocatilage complex*, form a concave surface, roughly elliptical, with long transverse axis.

Wrist movements are allowed not only by the radiocarpal joint, but

also by a group of joints: the radiocarpal joint, the *intercarpal* joints and the *mediocarpal* joint. The joints of act together to allow the flexion and extension of the hand (approximatively 85° in either direction) and its abduction and adduction (approximatively 15° and 45°, respectively).

2.1.3 *Upper limb myology*

With the term myology, the branch of physiology devoted to the study of the structure, functioning and disease of muscles. Here, naturally, focus will be set on the first two aspects. Every articular movement is made possible by the combined effect or two or more antagonist muscles that act through their tendons on the bones connected by the joint. It is beyond the scope of his work to go into detail on each involved muscle bundle; but nonetheless it is necessary to at least present them in a very brief, schematic way.

2.1.3.1 *Shoulder muscles*

Starting from the dorsal side of the trunk (see fig. 5), the two most extended muscle bundles are the *trapezius* and the *latissimus dorsi*.

The *trapezius* is a triangular, flat muscle that has multiple medial insertions: superiorly it is connected to the *occipital bone*, then in caudal direction to the *ligamentum nuchae*, and to the spinal processes of vertebrae T01-T12. Its superior fascicles insert on the posterior edge of the lateral part of the clavicle, the intermediate ones to the medial edge of the acromion and to the posterior part of the superior edge of the spine of the scapula (the process that ends with the acromion) and the inferior ones to the medial edge of the spine. It serves as a stabilizer for the scapula, controlling it during the active movement of the arm.

The origin area of the *latissimus dorsi* is as wide as that of the trapezius, starting from the spinal process of the T06 vertebra and descends along the spinal column to reach the iliac crest. Its insertion is found on the bottom of the bicipital groove of the humerus, on the medial part of the anterior surface below the humerus head. Its *aponeurosis*, i.e. the flat sheet or ribbon of tendon-like material that anchors the muscle or connects it with the part that the muscle moves, terminates into a large, flat tendon.
The latissimus dorsi concurs in the adduction, extension and more

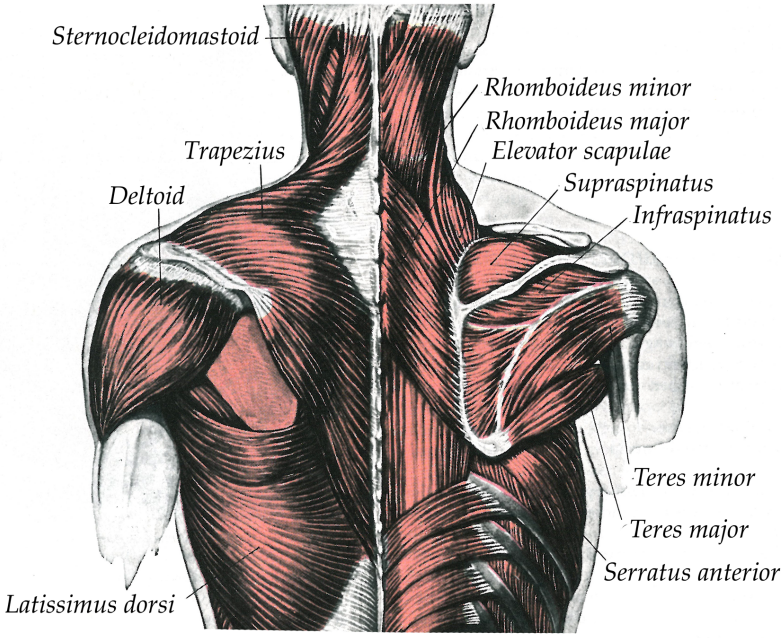

Figure 5: Superficial muscles of the posterior part of the neck, trunk and shoulder area. Adapted from [51]

importantly medial rotation of the humerus.

Other three muscles, the *rhomboideus major*, *rhomboideus minor* and *elevator scapulae* concur to stabilize the scapula and control its movement. The two rhomboidei bring the scapula backward, and they also rotate it together with the elevator scapulae and the *pectoralis minor*.

Switching to the frontal part of the trunk, and using as a reference fig. 6, it can be noted that two more muscles help controlling the scapula's motion: the *pectoralis minor* and the *serratus anterior*.

From the superior margin of the third, fourth and fifth rib originates the *pectoralis minor*, which finds its insertion on the medial edge and on the coracoid process of the scapula.

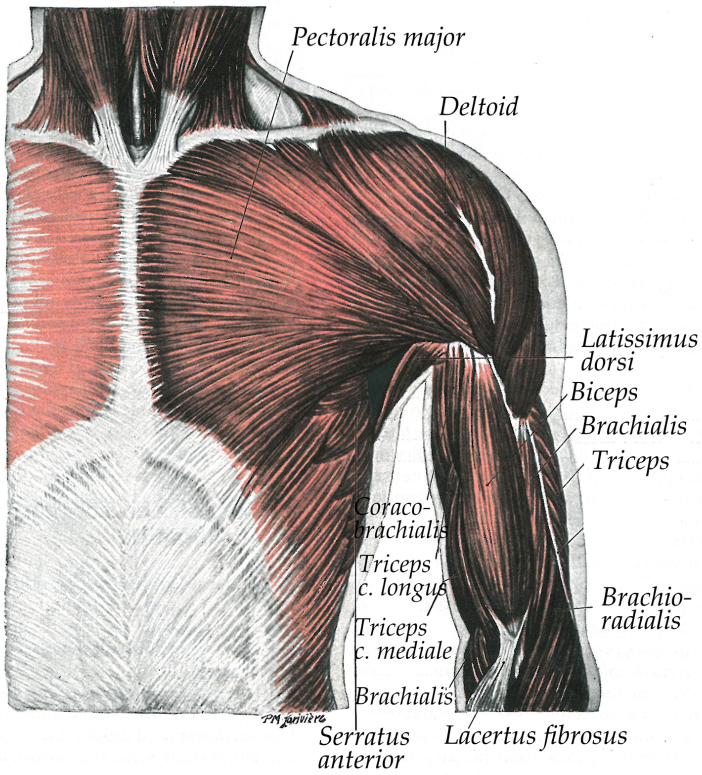

Figure 6: Superficial muscles of the ventral part of the trunk and the arm. Adapted from [51]

The *serratus anterior* originates from an extended costal area, and after enclosing the lateral part of the trunk terminates with an insertion on the medial edge of the scapula.
Together, these two muscles move the scapula anteriorly.

From the scapula, six muscles cover the shoulder and connect the scapula to the humerus: the *deltoid*, the *supraspinatus* and *infraspinatus*, the *teres major* and *teres minor*, and the *subscapularis*.

The *deltoid* is a large and robust muscle that originates from the anterior margin of the superior edge in the lateral part of the clavicle, from the lateral part and the superior surface of the acromion, and from the entire inferior edge of the scapula's spine. The muscle's fascicula

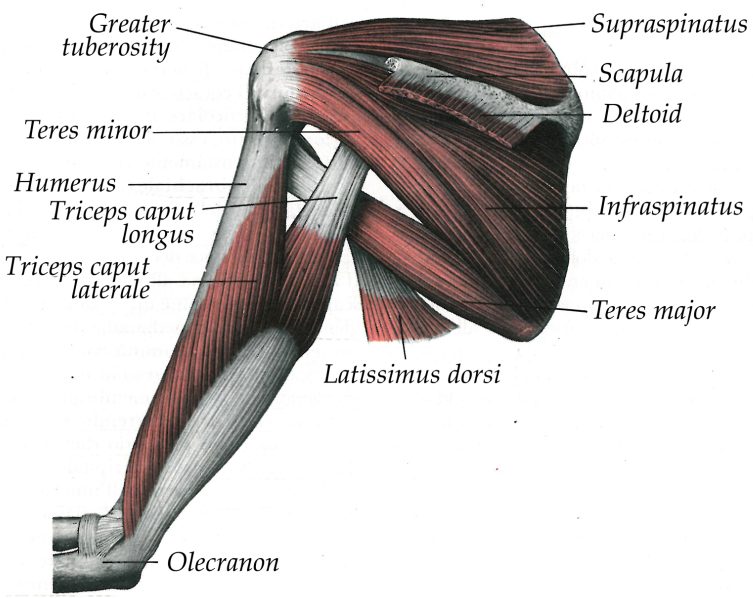

Figure 7: Dorsal muscles of the scapula and triceps. The spine of the scapula has been sectioned close to its lateral extremity. The acromion and the coroidal process have been removed. The humerus is laterally rotated and the forearm is pronated. Adapted from [51]

converge to an aponeurosis that connects to the deltoid tuberosity on the antero-lateral part of the intermediate part of the humerus (fig. 3). This muscle, together with the *pectoralis major*, flexes the humerus and rotates it anteriorly. Together with the supraspinatus, adduces and raises laterally the arm.

The *pectoralis major* is a large, thick and triangular muscle that origins from the medial half of the clavicle, from the lateral part of the anterior surface of the sternum and inferiorly up the the seventh rib. Its insertion is situated on the anterior and lateral edge of the proximal part of the humerus, laterally to that of the latissimus dorsi, where it ends with a flat tendon, approximately 5 cm wide. It is an active muscle in humerus extension, adduction and internal rotation. The superior fascicles are more active on the extension of the humerus, while the inferior ones are more active on internal rotation and adduction of the arm.

The *subscapularis* originates from the lateral two-thirds of the scapula, it converges into a tendon that inserts at the small tuberosity of the humerus (fig. 2) in the anterior part of its proximal end.

The *supraspinatus* has its origin on the *supraspinatus fossa* of the scapula, i.e. the depression found in the superior part of the posterior surface of the scapula, that terminates in the scapula's spine. The muscle passes then under the acromion and converges into a tendon that inserts in the most proximal facet of the greater tuberosity of the humerus.

The *infraspinatus* is a triangular muscle that originates from the *infraspinatus fossa* of the scapula, a wide depression underneath the spine, and its terminal tendon inserts on the intermediate facet of the greater tuberosity of the humerus.

A thin and elongated muscle, the *teres minor*, originates from the superior two-thirds of the posterior surface of the scapula, close to its lateral edge, and converges to a tendon that inserts on the inferior facet of the greater tuberosity of the humerus.

These last three muscles act together to hold the humerus head in its correct place in the glenoid fossa, and offering resistance to sliding movements of the head itself, with respect to its housing.

The *teres major* is a thick, flat muscle, that originates from an oval area of the posterior surface of the scapula, near its inferior edge, and converges into a 5 cm-wide tendon, at the base of the bicipital groove of the humerus. It carries the humerus medially and posteriorly, and it rotates it medially.

2.1.3.2 *Arm muscles*

This group of muscles is composed by the *coracobrachialis*, the *brachialis*, the *biceps brachii* and the *triceps brachii*. The first one acts only on the scapulohumeral joint, the last two act both on the scapulohumeral joint and on the elbow joint. The brachialis acts only on this last joint.

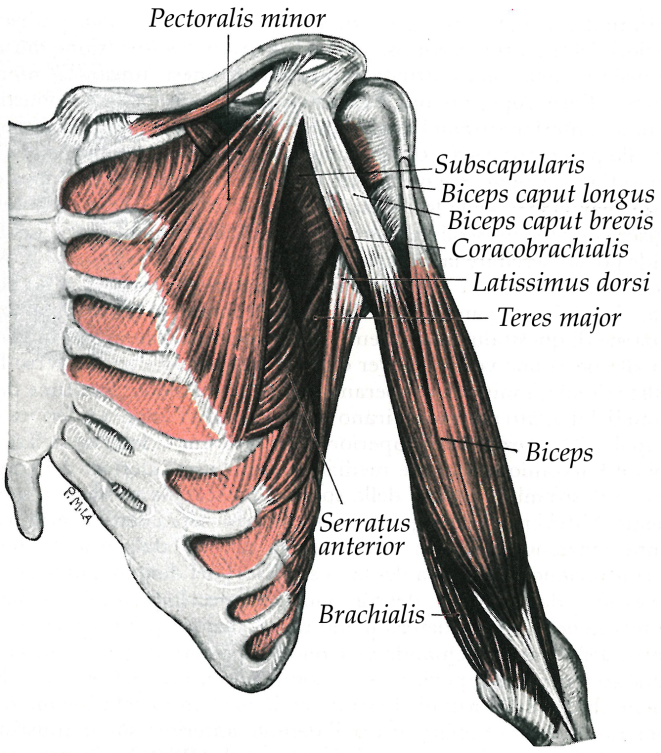

Figure 8: Deep muscles of the ventral part of the trunk and of the arm. Adapted from [51]

The *coracobrachialis* originates from the apex of the coracoid process, where it shares its tendon with the caput breve of the biceps, and converges to a tendon, about 3-5 cm wide, inserting on a depression situated approximatiely at the halfway medial section of the humerus.

The *biceps brachii*, or simply *biceps* since the reference to the upper limb is here obvious, is a large muscle that divides itself into two sections: the *caput breve* and the *caput longus*. The first one originates, as noted above, from the coracoid process together with the coracobrachialis, while the origin of the second is situated into the fibrous capsule of the scapulohumeral joint and immediately above the glenoid fossa. The two fascicula join approximatively 7 cm above the elbow joint, and connect to the posterior part of the radial tuberosity, a process that extends from the medial edge of the radius.
The biceps is a powerful supinator of the forearm. It also flexes the

elbow, more efficiently when the forearm is in supination. It is also a moderate flexor of the humerus.

The *brachialis* origin is in the inferior part of the anterior face of the humerus. It inserts on the ulna inferior edge and on the anterior face of the *coronoid process* (see fig.4). It is an elbow flexor, both during pronation and supination.

The *triceps brachii*, or simply *triceps*, is a three-headed muscle (the name derives from its shape). It is subdivided into the *caput longus*, the *caput laterale* and the *caput mediale*. The first head, the caput longus, originates with a flat tendon from a process just under the glenoid fossa, at the lateral edge of the scapula. The lateral head originates from a thin, linear and oblique crest on the posterior edge of the humerus and from the lateral edge of the humerus body. The medial head originates from a wide surface on the posterior part of the humerus.

All the muscle's fascicula converge into a large aponeurosis and into a common tendon, that converges prevalently on the superior edge of the olecranon. Laterally, a bundle continues over the anconeus.

The triceps is the major extensor of the forearm.

2.1.3.3 *Forearm muscles*

The muscles of the forearm are subdivided into two groups: an anterior group, made primarily of flexors, and a posterior group, in which mostly extensors are found. Some muscles can then cooperate to accomplish more elaborate tasks.

In the anterior group, the *pronator teres*, the *palmaris longus*, the *flexor carpi radialis*, the *flexor carpi ulnaris* and the *flexor digitorum superficialis* constitute the superficial flexors.

All five muscles origin is found within the common flexors tendon, in the medial epcondyle of the humerus, the *epithroclea* (Figure 3).

The *pronator teres* has two heads, one on the humerus and one on the ulna. The first one is the most important, while the second is thinner. The muscle crosses diagonally the forearm and terminates into a flat tendon that inserts on a coarse surface toward the middle of the radius. Its actions, as the name suggests, are primarily tied to the pronation of the hand, that it accomplishes by bringing the radius above and across

the ulna. A backward rotation of the palm is also noticeable during the action of the pronator teres, together with a slight flexion of the forearm. It acts in concert with the pronator quadrus.

The *palmaris longus* is a slender muscle, found on the medial side of the flexor carpi radialis, and through a long and thin tendon it inserts on the palmar aponeurosis, crossing the *carpi transversum ligament* anteriorly (Figure 9). Its function is to flex the hand, and to tense the palmar aponeurosis.

The *flexor carpi radialis* runs medially to the palmaris longus, originates from the epitrochlea trough the common tendon of the flexors, and inserts on the base of the second metacarpal bone. This muscle flexes the wrist joint, together with the flexor carpi ulnaris and the flexor digitorum superficialis. It also contributes to the abduction of the hand, also, in concert with the extensor carpi radialis.

The *flexor carpi ulnaris* is the most medial of the superficial flexors of the forearm, and originates with two heads: one humeral and one ulnar. The second is the most important and originates from the medial margin of the olecranon. It connects to the hand on the three most medial carpal bones. Together with the flexor carpi radialis, the palmaris longus and the flexor digitorum superficialis it flexes the hand, and with the extensor carpi ulnaris adduces it.

The *flexor digitorum superficialis* is the deepest of the group, and also originates with two heads: one humeroulnar and one radial. the first one is the wider, and is situated on the epitrochlea, originating form the common tendon, the anterior fascicle of the collateral ulnar ligament, and the medial surface of the coronoid process. The radial head is thin and laminar, and originates from the biceps tuberosity of the radius. The muscle presents generally two fascicle: the most superficial of the two acts on the annular and middle finger, the deeper one on the index and little finger.
The flexor digitorum superficialis flexes the fingers, starting from the middle phalanxes and then the proximal ones. It is also a flexor of the wrist, and is principally involved in the rapid and powerful flexion of the fingers, in grasping tasks.

The deep group of flexors is composed by the *flexor digitorum profundis*, the *flexor pollicis longus* and the *pronator quadrus*.

The *flexor digitorum profundis* originates from the anterior and medial three-fourths of the surface of the ulna, from a depression in the medial part of the coronoid process of the ulna, and from the proximal three-fourths of the posterior margin of the ulna. Its insertion is multiple, with four tendons that run under the ligament carpi transversum and the aponeurosis of the flexor digitorum superficialis, and connect to the palmar face of the distal phalanxes.
The muscle flexes the distal phalanxes after the action of the flexor digitorum superficialis (that flexes the medial phalanxes). It acts for moderate flexion velocities of the fingers, while it is less active for more rapid movements.

The *flexor pollicis longus* originates from the anterior surface of the radius, between the radius tuberosity and the pronator quadratus, and frequently from the lateral margin of the coronoid process. It terminates into a flat tendon that runs under the carpi transversum ligament that inserts at the palmar base of the distal phalanx of the thumb, and thus its action is to flex this finger.

The *pronator quadrus* is a square, flat muscle that originates from an oblique crest in the distal anterior part of the ulna, and terminates on the distal fourth of the anterior surface of the radius. It is the most powerful pronator of the forearm, and acts together with the pronator teres. It also keeps the radius and the ulna together when forces acting on the carpus tend to bring the forearm upward.

Following the same scheme used for the flexors, the group of the superficial extensors will be presented first, and then attention will be posed on the deep extensors.
The *brachioradialis*, the *extensor carpi radialis longus*, the *extensor carpi radialis brevis*, the *extensor digitorum*, the *extensor digiti minimi* and the *anconeus* form the first of the two groups of the extensors.

The *brachioradialis* is the most superficial muscle of the lateral part of the forearm, originates from the superior part of a surface just above the humerus' condyle, the *supracondylar ridge*. The muscle's fascicula

terminates before the halfway section of the forearm, and converge into a tendon that inserts on the distal part of the lateral surface of the radius, near the styloid process.
Even though it is in the group of the extensors, this muscle is a *flexor* of the elbow, and acts the most with a balancing function in rapid rotations of the forearm.

The *extensor carpi radialis longus* has its origin on the distal part of the supracondylar ridge, and in part on the common tendon of the extensors. The insertion of this muscle is found distally of the radial part of the dorsal surface of the base of the second metacarpal bone.

The *extensor carpi radialis brevis* originates from the lateral epicondyle of the humerus and with a tendon common to other extensors from the collateral radial ligament. It converges into a long tendon that inserts at the proximal part of the base of the second metacarpal bone.
The two previous muscles act together as *flexors* of the fingers. Together with the extensor carpi ulnaris they extend the wrist, and with the flexor carpi radialis they abduct it.

The *extensor digitorum* originates from the common tendon of the extensors, and distally it subdivides into four tendons, that run into a tunnel underneath the dorsal carpal ligament, and then diverge on the dorsal part of the hand, going each to a different finger.
It acts on the fingers' extension to set up the grabbing motion, or to release the grab itself. It is a primary actor on the extension of the wrist, together with the extensors of the carpus. It also tends to abduct the index, the annular and the little finger.

The *extensor digiti minimi* is a thin and slender muscle, situated medially to the extensor digitorum, and frequently connected to the latter. It originates from the common tendon of the extensors, Distally, its long tendon subdivides in two ramifications: one joins the common tendon of the extensors on the dorsal side of the hand, while the other gets to the little finger.
This muscle acts to extend the little finger and the wrist.

The *extensor carpi ulnaris* originates from the medial epicondyle through the common extensors' tendon and from the posterior part of the ulna. The insertion of its distal tendon is found at the base of the

fifth metacarpal bone.
Together with the extensor carpi radialis brevis and longus, it extends and stabilize the wrist, expecially during grasping tasks. With the flexor carpi ulnaris it adduces the hand.

The *anconeus* is a small, triangular muscle that has its origin on the posterior part of the epicondyle, and its insertion at the lateral margin of the olecranon and at the superior part of the posterior surface of the ulna.
It helps the triceps in extending the elbow.

The last group of muscles that will be considered here is the group of the deep extensors of the forearm, comprehending the *supinator* , the *abductor pollicis longus*, the *extensor pollicis brevis* the *extensor pollicis longus* and the *extensor digiti II*.

The *supinator* encloses the proximal third of the radius, and origins from a wide area that begins with the humerus epicondyle and descends laterally along the ulna surface. The insertion of the muscle is found at the lateral surface of the proximal part of the radius, reaching the distal insertion of the pronator teres.
As its name suggest, the supinator is the major actor in rotation the radius to bring the palm of the hand in lateral direction. For slower rotations it generally acts alone, while for faster rotations a synergistic action with the biceps is noticed.

The *abductor pollicis longus* originates from the posterior surface of the central body of the ulna, underneath the anconeus, and from the posterior third of the radius. It terminates into a tendon that connects to the radial side of the base of the first metacarpal bone.
It abduces the thumb and the wrist.

The *extensor pollicis brevis* is found medially to the abductor pollicis longus and it is tied to this muscle. Its origin is on the posterior face of the radius, while its insertion is found at the dorso-lateral part of the base of the first phalanx of the thumb.
This muscle extends the thumb and concurs to the abduction of the wrist.

The *extensor pollicis longus* is larger than the previous muscle, and covers part of its proximal insertion. It has origin in the lateral part of the medial third of the posterior surface of the central part of the ulna. Finds its distal insertion at the base of the last phalanx of the thumb. Together with the extensor pollicis brevis, it extends the thumb and abduces the wrist.

The *extensor digiti II* origins from the posterior face of the ulna, underneath the extensor pollicis longus, and from the adjacent interosseus membrane. Its insertion is found in the posterior digital expansion of the index finger.
It acts to extend the wrist and the index.

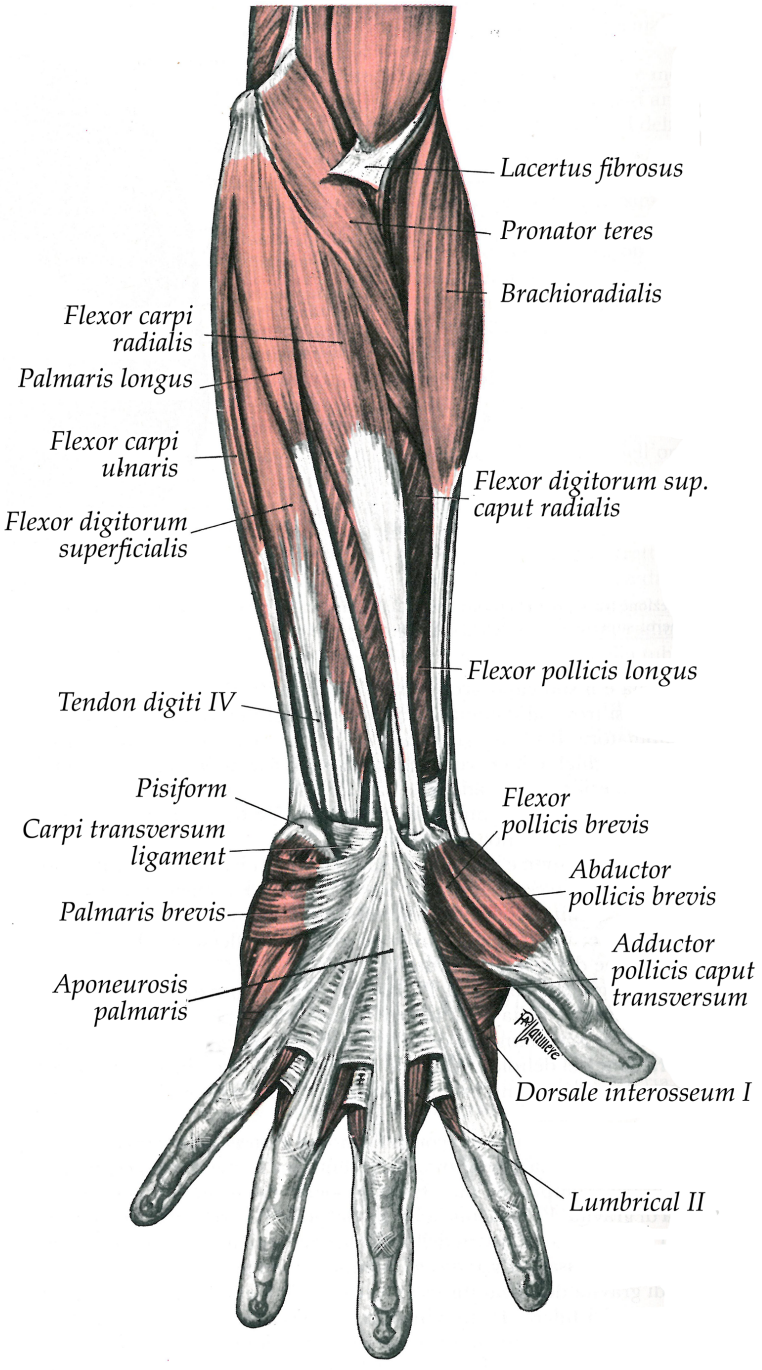

Figure 9: Superficial flexors of the forearm. Adapted from [51]

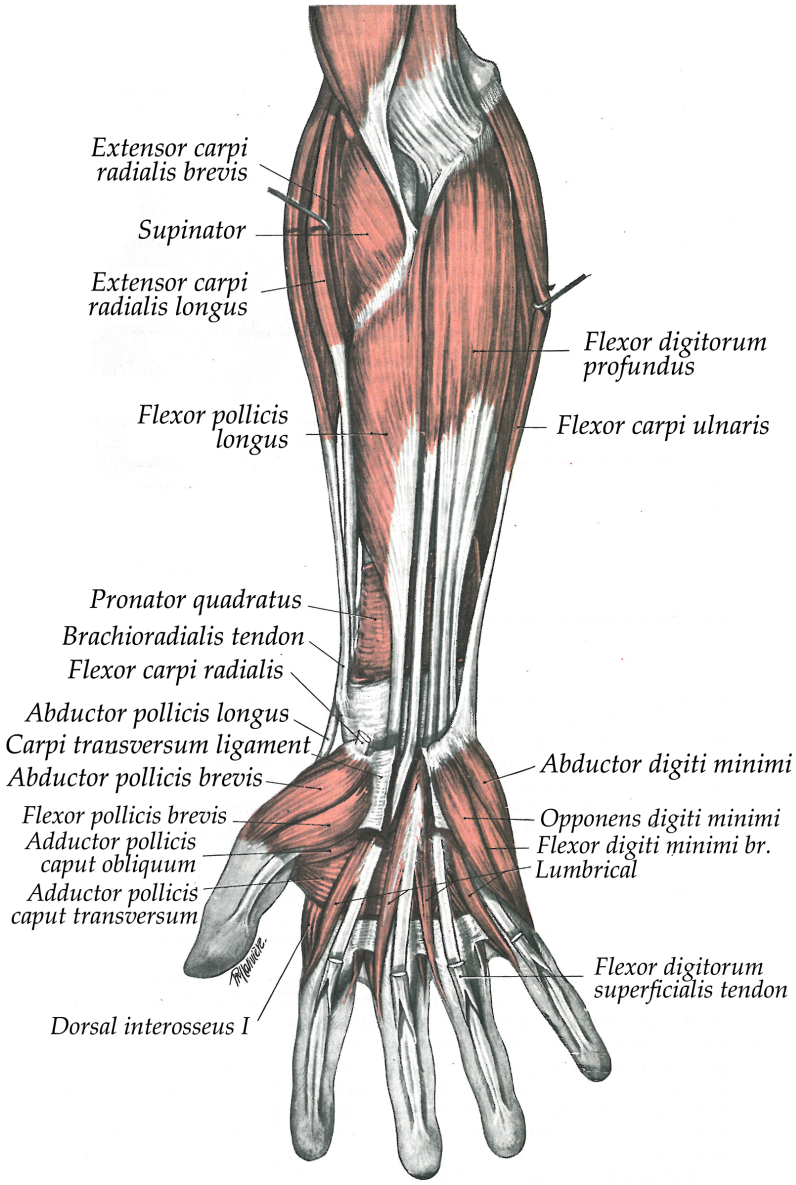

Figure 10: Deep flexors of the forearm. Adapted from [51]

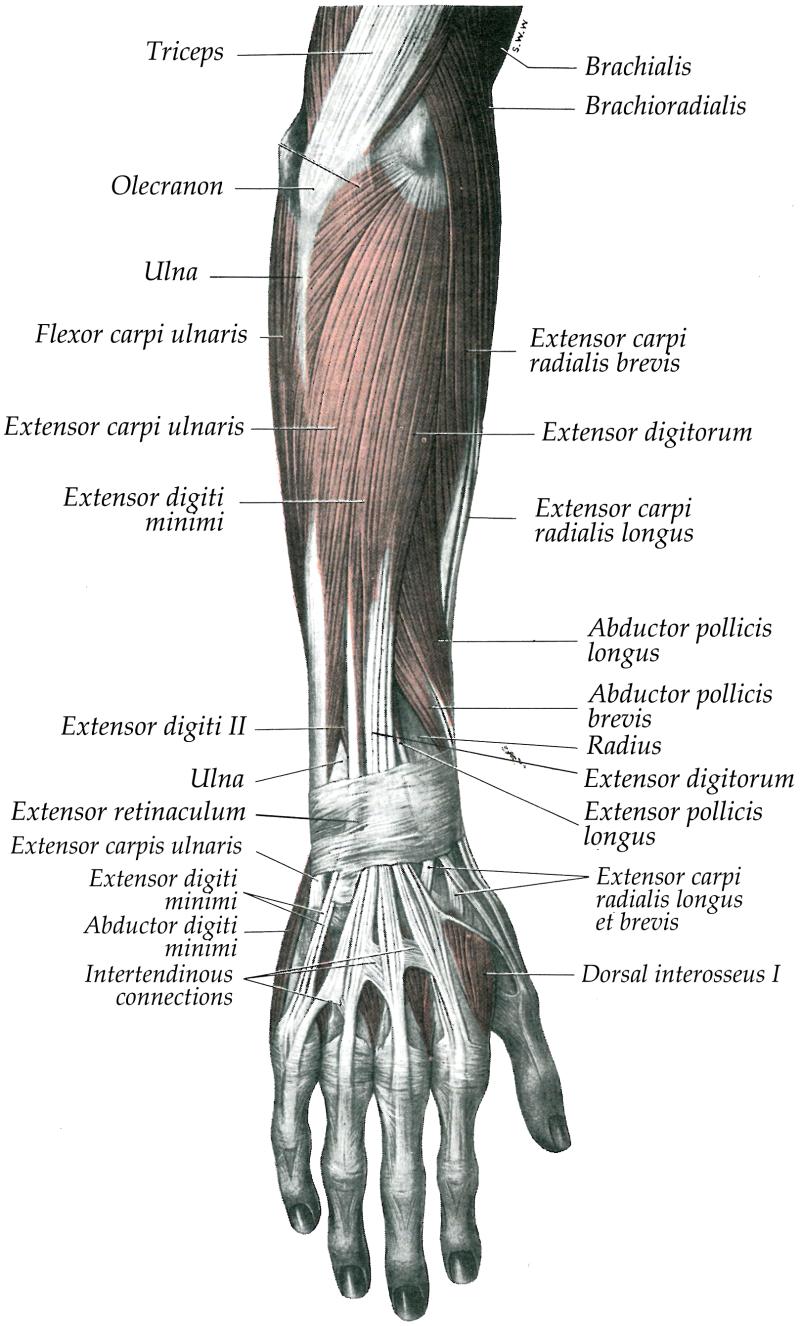

Figure 11: Superficial extensors of the forearm. Adapted from [51]

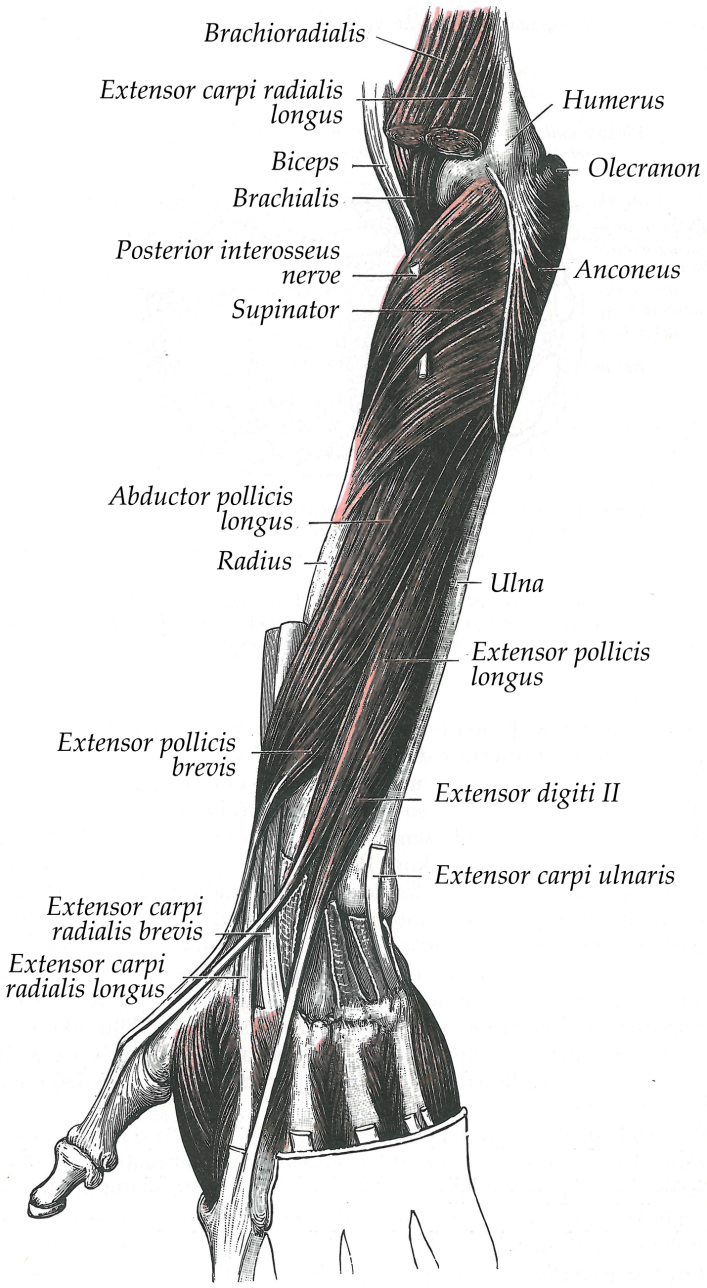

Figure 12: Deep extensors of the forearm. Adapted from [51]

2.2 MODEL GEOMETRY AND CONSTRAINTS

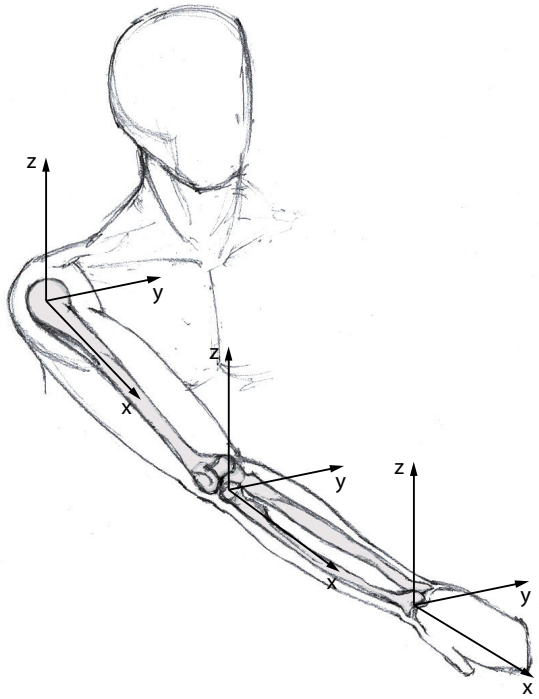

Figure 13: Model schematics. A node is placed at each bones', or set of bone's in the case of the hand, proximal epixondyle.

The general-purpose multibody software MBDyn, available under GNU GPL 2.1 open-source licence at [1] was used to generate the model. The software is developed and mantained at the Dipartimento di Ingegneria Aerospaziale, Politecnico di Milano, and distribuited freely to promote the access of academia, research facilities, and Small-Medium Enterprises (SMEs), to powerful and versatile analysis.
The capabilities of he software were both exploited and extended in the course of the present work.

The translation of the anatomical structures and relationships described above into a multibody model is a process that due to its nature

1 Multibody dynamics (MBDyn). http://www.aero.polimi.it/mbdyn/

does not offer a unique solution. The level of detail, as in any mathematical model of a physical system, depends on the desired level of accuracy, and from the physical aspects of the system that are considered most important for the phenomena investigated.

In the present case, the objective of the simulation is to reproduce the passive behavior of the human arm with respect to the generation of mechanical impedance in manipulation tasks, in which typically the hand is in grasping configuration, e.g. on the collective or cyclic control inceptor in the case of a rotorcraft, or the handlebar in the case of a motorcycle, etc.

It is also worth noticing that a very precise reproduction of the motion of the skeletal system of the upper limb is not sought. As a consequence, the assumption that during prono-supination the radius rotates about a fixed ulna is justified here. Furthermore, motions that involve an important pronation or supination of the hand are generally of little importance in vehicle and rotorcraft control.

Another simplification that can be made, in light of what has been stated above, is consist in disgregarding the action of the interior structures of the hand devolved to the control of finger motion, and therefore to condense of the behavior of the hand into one single rigid body. For this reason the anatomy of the hand was not explained in detail in the previous sections.

Shoulder complex motion is also disregarded, as the trunk and the shoulder are assumed to be in their rest position during the tasks considered, to assure that in this preliminary phase the model is the more manageable possible.

In fig. 13 the location of nodes used to model the kinematics of the upper limb are superimposed to the skeletal system. Every bone is considered as a rigid body, and joints are applied to its condyles. The length of the rigid body representing the generic bone can be thought as the distance between the bone condyles along the *mechanical axis*, i.e. the axis connecting the centerpoints of the condyles.

The model includes 4 rigid bodies: the humerus, the ulna, the radius, and the hand. Each bone's reference system is situated in the center of its proximal condyle, with the x-axis along the bone mechanical axis, the y-axis pointing toward the medial plane and the z-axis directed superiorly to form a right-handed coordinate system.

Since four nodes, i.e. objects that possess 6 degrees of freedom, are present in the model, a total of 24 degrees of freedom have to be accounted for. For practical purposes a fifth node, clamped, is used to model the ground reference frame.

2.2.1 *Algebraic constraints*

As noted in Section 2.1.2, synovial joints perform functions that can be approximated by an equivalent algebraic constraint. In Table 2 the correspondence between the different types of synovial joints and algebraic constraints is summarized.

It should be evident that modeling a joint by means of an algebraic constraint makes sense only if accurate reproduction of the joint motions is not sought, for the reason that a real articulation presents a wide range of characteristics that make it really difficult to model precisely [5, 38, 11].
For example, in gliding synovial joints, the surfaces that slide upon each other are never flat in a geometrical sense, and can present different degrees of curvature, generally making a gliding joint impose a complex surface-to-surface constraint, depending on the local curvatures.

In almost all the joints that involve a relative rotation between the participating bones, the axis (or axes) of rotation is (are) not fixed, and is (are) rarely perfectly orthogonal to the mechanical axis of the bones.

Nonetheless, axis migration and correct geometrical constraints are almost never implemented even in biomechanical multibody models that aim at extremely precise reconstruction of the upper limb motion (with some exceptions, see [15]) since this approach brings with it two major disadvantages: the resulting model would be less manageable and efficient, and more importantly it would be extremely specific for the subject modeled. Keeping in mind that the possibility to extend the model and stating it in a way as general as possible is a priority for the current project, ideal algebraic constraints have been used.

The shoulder complex can be approximated to a perfect spherical joint, that constraint the center of the proximal condyle of the humerus and the center of the glenoidal fossa to be coincident. Having disregarded the motion of the shoulder, the spherical joint acting on the humerus is grounded.

Table 2: Different types of synovial joints and their algebraic approximations

Synovial joint	Algebraic constraint	Example
gliding	in plane joint	acromioclavicular joint
pivot or trochoid	cylindrical joint	proximal radioulnar joint
hinge	revolute hinge joint	humeroulnar joint
enarthrosis	spherical joint	glenohumeral joint
condyloid or ellipsoidal	Cardano joint	radiocarpal joint
saddle joint	Cardano joint	sternoclavicular joint

At the distal end of the humerus, two joints connect the radius and the ulna to this bone: the humeroulnar joint is approximated by a revolute joint, allowing only the relative rotation of the ulna with respect to the humerus about the ulna y-axis, centered in the trochlea. The humeroradial joint is modeled as a spherical joint, constraining the center of the capitulum to be coincident with a point slightly outside the physical proximal end of the radius. For the purpose of this work it has been identified with the proximal end of the rigid body representing the radius.

Proximal and distal radioulnar joints can be simplified and condensed into a single element by imposing an in-line joint between a point P and the mechanical axis of the ulna. Point P is offset from the radius axis in radius y-direction so that the two bones in the rest position of fig.13 are held parallel to each other.

The complex succession of carpal joints has been modeled as a Cardano joint that transmits torque about the x-axis of the radius, while allowing rotations about the radius y and z-axes.

To summarize

- the spherical joints remove 3 degrees of freedom each
- the revolute joint removes 5 degrees of freedom
- the in line joint removes 2 degrees of freedom
- the Cardano joint removes 4 degrees of freedom

so that the system has $24 - 17 = 7$ degrees of freedom. When all the motions of the 6 degrees of freedom of the hand are prescribed, the

Table 3: Inertial properties of the rigid bodies in the model. All masses and moment of inertia are considered as accounting for both the bones and their related muscles. Data reported here is valid for 50% percentile male, with height 180 cm and weight 80 kg, according to regression equations of [7, 8]

Body	Mass [kg]	J_{xx} [kg mm^2]	J_{yy} [kg mm^2]	J_{zz} [kg mm^2]
Humerus	2.09	3119	18325	15763.2
Radius	0.66	480	3568	3409
Ulna	0.87	300	5352	5133
Hand	0.53	807	3949	4262

upper limb is a 1-dof redundant mechanism.

Inertial properties have been attributed to the rigid bodies associated with the humerus, radius, ulna and hand condensing the contribution of bones and the ones of the muscles, and are shown in Table 3. The parameters are calculated starting from the subject's height and weight, using statistical regression equations published in [7, 8].

Other important geometrical quantities are presented in Table 4. All the lengths of the bone sections in the model are parametrized with respect to bone's length. Reference values of 300 mm, 250 mm and 100 mm are considered for humerus, radius and ulna, hand, respectively, in the table.

The model is completed by the elements that represent the muscles. One-dimensional, viscoelastic elements that can exert a force between their attach point as a function of their deformation state and their activation level are used.
It is thus essential to closely examine the viscoelastic behavior of skeletal muscles to attribute a sufficiently accurate constitutive law into the one-dimensional elements that connect their attach points in the model.

2.3 MUSCLE MODELS

Every mechanical action throughout the human body is performed by the muscle tissue, that is the only form of contractile tissue in animals.

Three kinds of muscles are present in the human body: *skeletal*, *cardiac* and *smooth*. The latter are non-voluntary, and line the hollow internal organs: they operate all the mechanical non-voluntary actions and possess a structure profoundly different from the other two types. Cardiac and skeletal muscles share the same microscopic structure and physiology, but differentiate themselves upon the voluntary nature of their activation: while cardiac muscles are, obviously, non-voluntary, skeletal muscles can be activated by voluntary stimuli. They provide the intermedium between the desired articular motion and the actual one.

Skeletal muscles are non-linear, viscoelastic elements that can contract upon activation: when a nervous signal acts on them, they can exert a traction force between their attachment points, transmitted by tendons. Their characteristic is non-symmetric as they can only produce traction forces, and do not respond to compression.

As a consequence, to be able to produce articular joint motions in the two directions, they always act in groups, the most basic of which is a

Table 4: Geometrical properties of the model. All the quantities are expressed in millimeters, in the reference frame of the body to which they refer to.

Body	Proximal epicondyle pos.			Distal epicondyle pos.		
	x	y	z	x	y	z
Humerus	0	0	0	300	0	0
Radius	0	-16	0	250	-16	0
Ulna	0	16	0	250	16	0
Hand	0	-16	0	100	-16	0

Body	Center of mass position		
	x	y	z
Humerus	150	0	0
Radius	159	0	0
Ulna	78	0	0
Hand	51	0	0

pair of counter-acting muscles acting on the two sides of the joint. Quite commonly though, muscle groups consist of more than two muscle fascicula acting on the same joint motion in parallel, as is the case for biceps, triceps and quadriceps.

2.3.1 *Structure and microstructure of skeletal muscles*

Skeletal muscles and cardiac muscles are also indicated as *striated* muscles, as they present a microstructure composed of a collection of small contractile units, activated by electrical stimuli via the nervous system.

The basic contractile unit is called *sarcomere*, a structure made of long, fibrous proteins that can slide past each other upon activation. Hexagonal structures made of *myosin* protein are interposed to long filaments of *actin* protein, organized in complementary exagonal arrays, that connect themselves at the end of the sarcomere.

Sarcomeres represent the basic contractile unit in muscles, but cannot provide force on their own, they must be driven by a stimulus signal. The function of providing such signal is performed by a special kind of nerve fibers (or *axons*) that extend from motor neurons to a limited set of muscle fibers. A Motor Unit (MU) is the structure formed by a motor axon together with its controlled fibers.

Zooming back on the structure, it can be recognised that long, linear arrays of sarcomeres constitute *myofibrils*, that *muscle fibres* are collections of myofibrils, and that they are themselves organized in *fascicles* or *fascicula*, which together form the whole muscle.

Muscles are connected to articular joints, and bones in general, by means of tendons, which represent a non-contractile, stiff (relatively to the muscle) structure that provides a rigid connection for most of its functioning range, normally comprised in the strain range $2 - 5\%$.

The contraction process is represented in Figure 14. When the sarcomere is excited, protuberances of myosin called *cross-bridges* that are connected to the actin filaments bend toward the center of the sarcomere, effectively making actin slide with respect to myosin, and causing the shortening of the whole sarcomere.

Several different isoforms of myosin exist, each with different characteristics of ATPase activity, i.e. the activity of energy-freeing enzymes related to them. This behavior separates them into faster and slower

ones, and by extension there exist faster and slower fibers. The first ones are more akin to rapid, ballistic motions and generate a greater amount of force, while the latter are more suitable for slower but more sustained motions and can generate force for a more extended period of time.
Global force-generating characteristics of a muscle depend on the mix of slow and fast fibers that it contains.
[27].

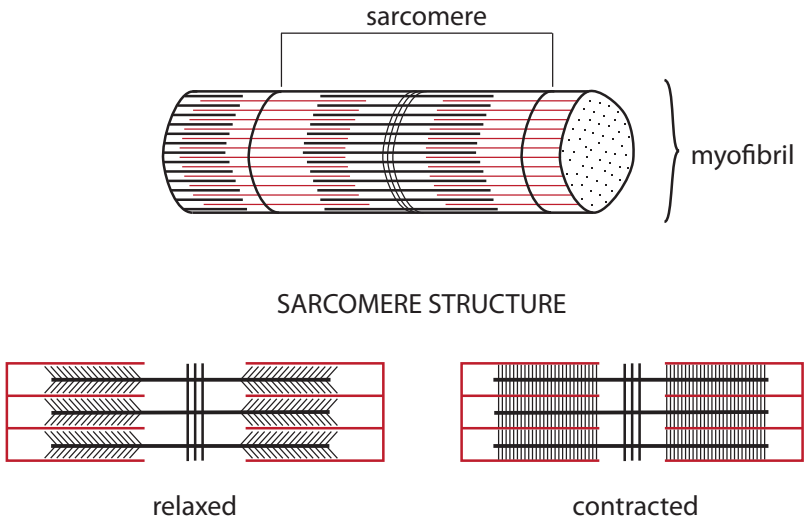

Figure 14: Myofibrils are long chains of sarcomeres. Below, schematics for sarcomere contraction. In red, actin proteins, while in black myosin proteins are represented. When the sarcomere is activated, myosin terminations bend backwards, making the actin shells slide and shortening the sarcomere.

2.3.2 *Muscle viscoelastic properties*

Global properties of the muscle arise from the characteristic of the single sarcomeres, and while tests on sarcomeres themselves are impractical, for obvious reasons, single-fiber or single-motor-unit tests are frequently executed [16, 30], together with whole-muscle tests, either in-vivo or in-vitro, human and animal samples.

The force generated by the sarcomere strongly depends on the degree of overlap between myosin and actin proteins., and thus to the general

strain field in the muscle fibers. The most commonly used parameter to indicate the axial strain of the sarcomere and, as it will be shown below, of the whole muscle, is the dimensionless length

$$x = \frac{l}{l_o} \tag{2.1}$$

rather than classically defined strain

$$\epsilon = \frac{l - l_o}{l_o} \tag{2.2}$$

If the fiber, or the muscle, is kept at a fixed length and activated, *isometric contraction* conditions are achieved, and after a brief transient, isometric force is reached. Varying the length of the fiber and repeating the experiment until a maximum force can be identified leads to the definition of peak isometric force F_o, and the fiber length that corresponds to such force is the optimal fiber length l_o.

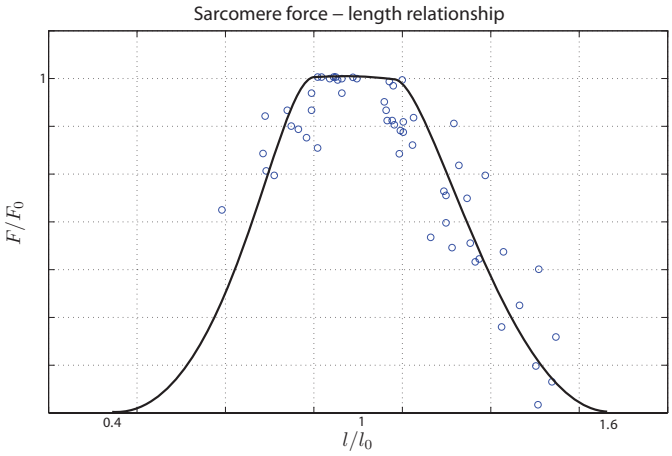

Figure 15: Force-length relationship for the sarcomere. Circles represent data collected by Gollapudi et al. and published in [16]

Figure 15 shows the force - length relationship for a typical sarcomere, superimposed to experimental data taken from [16]. The curve presents three distinct regions

- an initial ascending region, starting approximatively at 0.2-0.4 l_o
- a plateau region, extending from approximatively 0.8 to 1.1 l_o

- a descending region, that brings to zero force produced at about 1.6 l_0

Ascending and descending regions of the curve can be approximated by exponential functions, and present a certain degree of symmetry.

The peak isometric force can be estimated on the basis of muscle normal pressure σ_0 (supposed constant in skeletal muscles), and of physiological cross-section area $pCSA$. The latter can be found once muscle length, volume or mass, density and pennation angle are known. Pennation angle is the angle that muscle fibers form with the tendon axis, i.e. the axis that passes through the zone of tendon connection with the muscle bundle, the *aponeurosis*

$$pCSA = \frac{M_m \cdot \cos\alpha}{L_m \rho} = \frac{V_m \cdot \cos\alpha}{L_m} \tag{2.3}$$

with

M_m	muscle mass
V_m	muscle volume
$\rho = 1060$ kg/m^3	muscle density, constant
α	muscle pennation angle

σ_0 is also a constant for all skeletal muscles, and within the range 0.2-0.35 N/mm^2

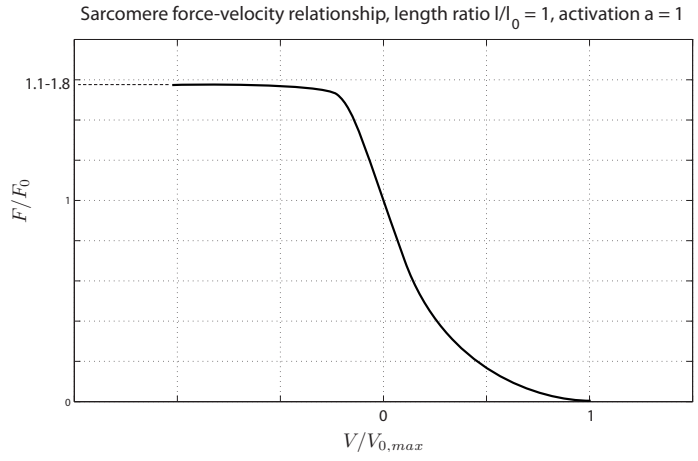

Figure 16: Force-velocity relationship for the sarcomere.

Muscle force also shows a strongly non-linear correlation to shortening velocity, i.e. the derivative with respect to time of sarcomere length, changed in sign

$$V = -\dot{l} \tag{2.4}$$

Starting from isometric conditions, and releasing the fiber while measuring the force exchanged between the constraint and the fiber itself, brings to the determination of the force-velocity relationship (Figure 16).
At $V = 0$, $x = 1$ and $a = 1$ peak isometric force is reached, as seen above. When $V < 0$, i.e. when the fiber is shortening, it can produce an higher force output, up to approximatively 1.6 times F_0, while it shows a decreasing force output as it shortens at increasingly velocity. A maximum lengthening velocity, $V_{0,max}$ is reached when the fiber is not producing any force.

While a bottom-up approach to muscle modeling, i.e. a modeling approach that starts from the single motor unit and builds the total muscle force from the sum of the single motor units forces, is possible and sometimes used [49], it would require an enormous surplus of computational cost, since it would be necessary to model the single MUs in every muscle, and every muscle can be constituted of many hundreds of MUs.

A more suitable approach, expecially when the goal of the simulations performed is kept into account, is to model the whole muscle starting from its response to strain and strain velocity, i.e. its viscoelastic properties.

2.3.3 *Hill-type muscle models*

The most widely used models for muscle contraction are based on the work of Archibald Vivian Hill, who proposed the first version of the model in 1938.

Figure 17 contains a schematic for the model in its original form.
A *contractile element* CE is responsible for the generation of the muscle force's active contribution, acting both as an actuator and as an elastic element. Thus, force generated in the CE is a function of muscle length ratio x, shortening velocity V, other than activation parameter $a(t)$.

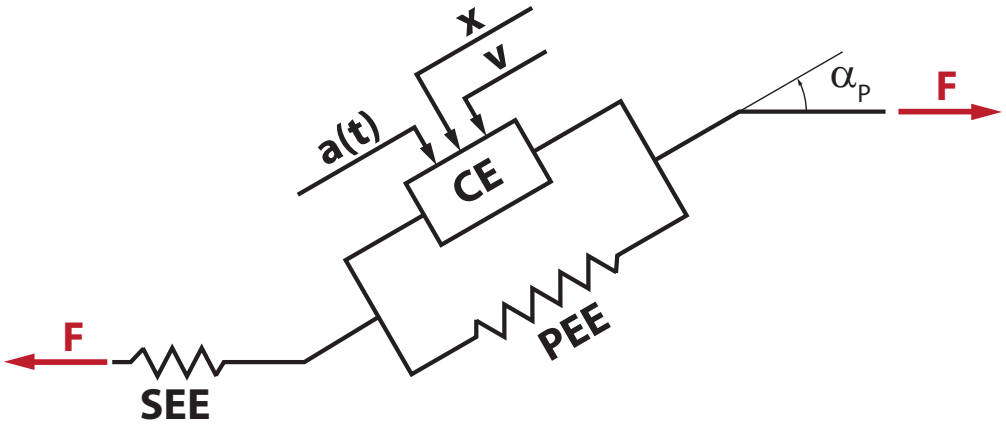

Figure 17: Hill's model for contraction dynamics scheme. Muscle force F is the product of the effect of a contractile element CE, in parallel with a first elastic element PEE and in series with another elastic element SEE. Since tendon compliance is generally dominant, SEE can often be neglected.

Angle α represents the so-called *pennation angle* of the muscle, i.e. the angle that muscle fibers form with respect to the tendon axis. It is an acute angle, generally small; its variation during the motion can be disregarded in all but short-tendon actuators.

Tendon elastic properties are introduced by means of a *parallel elastic element* PEE, sometimes referred to as *passive element*. A *series elastic element* SEE is sometimes considered, to separate muscle elastic energy stored in cross-bridges (supposedly in *titin* proteins) from elastic energy stored in tendons.
Since the former is generally negligible with respect to the latter, omitting the SEE is possible, at least when short-tendon actuators are not considered [14].
Disregarding SEE leads also to the elimination of several behaviors incompatible with the hypothesis of sarcomeres acting at unison, and fiber properties being a direct consequence of sarcomere properties. For example, fiber length could not be written as

$$L_m = \gamma \cdot L_s \tag{2.5}$$

where L_s is sarcomere length and γ the total number of sarcomeres in the fiber. This means that the force-length relationship of a fiber would not be, in this case, the scaled version of the force-length relationship of a sarcomere [53].

2.3.3.1 *Winters and Stark model*

Winters and Stark proposed a modification of an infinitely stiff SEE, and combining excitation and activation dynamics into a single relationship of the first order. This is done to take into account the delay between neural input u, that can be thought as axon input, and activation of the contractile element.

The model is only related to the active part of the muscolotendon actuator, and therefore only limited to the contractile element of Figure 17.

Output of the system is the force F, defined by means of the output function g_m

$$F = g_m(a, l, \dot{l}) \tag{2.6}$$

while state function f_m generates activation time derivative $\dot{a}$

$$\dot{a} = f_m(a, u) \tag{2.7}$$

in the above equations, l is the total muscle length. The output function f_m is defined as

$$f_m(a, u) = \frac{(u - a)^*}{\tau} \qquad \tau^* = \begin{cases} \tau_{ac} & u \geqslant a \\ \tau_{da} & u < a \end{cases} \tag{2.8}$$

with τ_{ac} activation time constant, τ_{da} deactivation time constant.

The state function g_m expression reads

$$g_m(a, l, \dot{l}) = aF_{lce}(l_{ce})F_{vce}(\dot{l}_{ce})F_{max} \tag{2.9}$$

where F_{lce} is the force-length relationship

$$F_{lce}(l_{ce}) = e^{\left(-\left(\frac{l_{ce} - l_{ceo}}{l_{cesh}}\right)^2\right)} \tag{2.10}$$

with

$$l_{ce} = l - l_t \tag{2.11a}$$
$$\dot{l}_{ce} = \dot{l} \tag{2.11b}$$

and

$$l_{ceo} = l_{min} + L_{opt}(l_{max} - l_{min}) - l_t \tag{2.12a}$$
$$l_{cesh} = L_{sh}(l_{max} - l_{min}) \tag{2.12b}$$

where

- l_{ce} length of contractile element
- l_t tendon length
- l_{ceo} optimal length of contractile element
- l_{cesh} parameter expressing the width of the force-length curve
- L_{opt} relative optimum muscle length
- L_{sh} relative width of the force-lenght curve

The force-velocity relationship is approximated by

$$F_{vce}(\dot{l}_{ce}) = \begin{cases} 0 & \dot{l}_{ce} \leqslant -v_{max} \\ \dfrac{V_{sh} \cdot (v_{max} + \dot{l}_{ce})}{V_{sh} \cdot v_{max} - \dot{l}_{ce}} & -v_{max} \leqslant \dot{l}_{ce} < 0 \\ \dfrac{V_{sh} \cdot V_{shl} \cdot v_{max} + V_{ml} \cdot \dot{l}_{ce}}{V_{sh} \cdot V_{shl} \cdot v_{max} + \dot{l}_{ce}} & \dot{l}_{ce} > 0 \end{cases} \tag{2.13}$$

with

$$v_{max} = V_{vm}\Big(1 - V_{re}\big(1 - a \cdot F_{lce}(l_{ce})\big)\Big) \tag{2.14}$$

whith

- v_{max} maximum contraction velocity
- V_{sh} parameter for concavity of Hill curve - shortening
- V_{shl} parameter for concavity of Hill curve - lengthening
- V_{ml} maximum velocity during concentric contraction
- V_{er} effect of activation on maximum velocity

As it is clear from the above relations, muscle force generation depends on a number of parameters (namely 10) that have to be fine-tuned

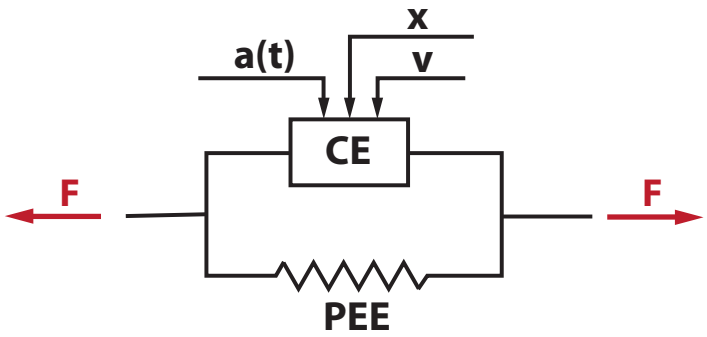

Figure 18: Simplified schematics for Hill-type model used. Pennation angle is being disregarded, as well as cross-bridge elasticity. Muscle and tendon elasticity is included in parallel elastic element PEE.

on the single muscle behavior, on top of the general coordinates dependent l and $\dot{l}$. Some considerations can be made though, to reduce the number of parameters involved and still retain sufficient accuracy to yield interesting results.

2.3.4 *Zajac approximations*

In a work that has become foundamental to muscle modeling [53], Zajac proposed some simplifications befitting to muscle-coordination level dynamic simulations, when many different muscles are involved in the generation of joint torques, and thus of joint movement.

His assumptions can be condensed as

1. the shape of the force-length curve is the same for all muscles, and does not change with activation
2. muscle SEE, when associated with cross-bridge stiffness, can be neglected completely. Muscle elasticity can be joined with tendon elasticity into a single PEE
3. force-velocity curve abscissa intercept is activation independent
4. it is reasonable to refer force-velocity relationships of all muscle fibers to a single reference maximum contraction velocity
5. pennation angle variation is relevant only for short tendon muscles, and can be disregarded when smaller than 15-20°

The first and second assumptions are dealt with in Section 2.3.1.

The third one is justified by the consideration that the force-velocity curve represents the muscle power generation characteristic, and although experimental data show that in some cases the zero-force intercept is affected by activation, this dependence will have a small effect on muscle dynamics.

Assuming that fibers do not produce compressive forces, a fully activated muscle composed of different fibers with different maximum velocities, will exert tension until the maximum shortening velocity of the fastest muscle fiber is reached. It is therefore reasonable to refer the force-length relationship to the maximum shortening velocity of fast muscle tissue, which at 37° C is about $10 \cdot L_o\, s^{-1}$

These considerations led Pennestrì et al. in the adaptation of a Hill-type model [42], suitable for upper limb biomechanic simulation, which condenses the passive elastic properties of tendon and muscle into a single PEE, and contractile behavior into a CE, in parallel with the former.

Parameters for the 25 muscles present in the model are collected in Table 5 and 6. Pennation angle variation is small for all muscles involved, and it is thus disregarded, and so the schematics for the model is the one of Figure 18.

The muscle force is defined by

$$F_m = F_a + F_p = F_o \left(f_1 f_2 a(t) + f_3\right) \tag{2.15}$$

The force-length relationship for the passive contribution is

$$f_3 = 1.3 \cdot \arctan\left(0.1(x - 0.22)^{10}\right) \tag{2.16}$$

while for the active contribution CE is

$$f_1 = e^{\left(-40(x-0.95)^4 + (x-0.95)^2\right)} \tag{2.17}$$

The force-velocity relationship is

$$f_2 = 1.6 - 1.6e^{\left(-\frac{1.1}{(1-v)^4} + \frac{0.1}{(1-v)^2}\right)} \tag{2.18}$$

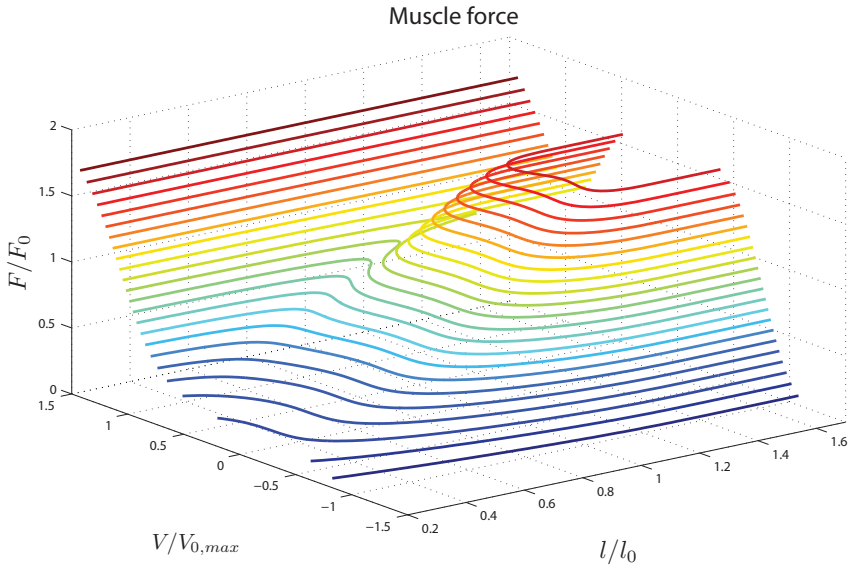

Figure 19: Dimensionless muscle force as a function of muscle length ratio e lengthening velocity.

The variables in functions (2.16 - 2.18) are

$$x = \frac{l}{l_0} \tag{2.19a}$$

$$v = \frac{V}{V_0} \tag{2.19b}$$

The muscle length l is the total muscle length, including tendon.

Activation modifies the curves in Figures 15 and 16 without changing their shape, as shown in Figures 20 and 21.

Figure 19 shows the iso-force curves for the surface of admissible muscle dimensionless force as a function of x and V.

A maximum lengthening velocity of $4L_0s^{-1}$ was set for all the muscles, according to experimental data published by [29].

Table 5: Muscle model parameters for muscle bundles present in the model. Peak isometric force and optimal lengths are taken from [21], pennation angles from [28, 21, 30].

	Muscle	L_0 [mm]	F_0 [N]	α [deg]	P_1 [mm]			P_2 [mm]		
					x	y	z	x	y	z
Muscles connecting humerus to the rest of the body										
1	Coracobrachialis	197	242.5	27	20	30	35	174	21	0
2	Deltoid - Anterior Fascicles	179	1142.6	22	35	25	35	136	-12	10
3	Deltoid - Middle Fascicles	159	1142.6	15	35	-22	20	136	-24	18
4	Deltoid - Posterior Fascicles	148	259.9	18	-35	10	0	136	-24	18
5	Latissimus Dorsi	380	1059.2	21	-65	110	-290	75	25	9
6	Pectoralis Major	147	1270.3	22	45	110	10	36	0	25
7	Supraspinatus	108	487.8	7	-36	80	35	-32	2	-13
8	Infraspinatus	111	1210.8	19	-32	80	-40	-26	0	-20
Muscles connecting radius to the rest of the body										
9	Biceps brachii caput longus	388	624.3	0	0	-15	10	34	16	0
10	Biceps brachii caput brevis	324	435.6	0	20	30	25	3	16	0
Muscles connecting ulna to the rest of the body										
11	Triceps brachii caput longus	290	798.5	12	-35	20	-20	-15	0	-22
Muscles connecting humerus to ulna										
12	Anconeus	55	350	0	300	-5	-12	-14	7	-11
13	Triceps brachii caput laterale/mediale	211	1248.6	9	112	0	-28	-27	0	-6
14	Brachialis	140	987.3	0	196	-8	16	17	15	5

Table 6: Muscle model parameters for muscle bundles present in the model – continuation.

	Muscle	L_0 [mm]	F_0 [N]	α [°]	P_1 [mm]			P_2 [mm]		
				x	y	z	x	y	z	
Muscles connecting humerus to radius										
15	Brachioradialis	306	261.3	2.4 ± 6	246	-7	0	238	-18	13
16	Pronator teres	148	566.2	9.6 ± 8	270	33	-7	55	-18	12
Muscles connecting humerus to hand										
17	Flexor carpi ulnaris	317	128.9	12.1	265	27	-5	5	30	23
18	Extensor carpi ulnaris	290	93.2	3.5	269	-27	-5	5	30	-18
19	Extensor digitorum	387	100.7	3.0	269	-20	-20	8	0	-16
20	Flexor digitorum superficialis	380	226.6	4.9 ± 0.7	275	27	-10	7	18	26
21	Flexor carpi radialis	307	74	3.1	275	27	-7	3	-20	32
22	Extensor carpi radialis	305	405.4	0	245	-20	0	5	-23	-11
Muscles connecting ulna to radius										
23	Pronator quadatrus	33	75.5	9.9 ± 3	200	7	14	236	27	23
24	Supinator	61	476	< 15	13	17	-8	28	13	-24
Muscle connecting ulna to hand										
25	Adbuctor pollicis longus	202	59.5	2.6 ± 6	115	-21	-5	3	-18	23

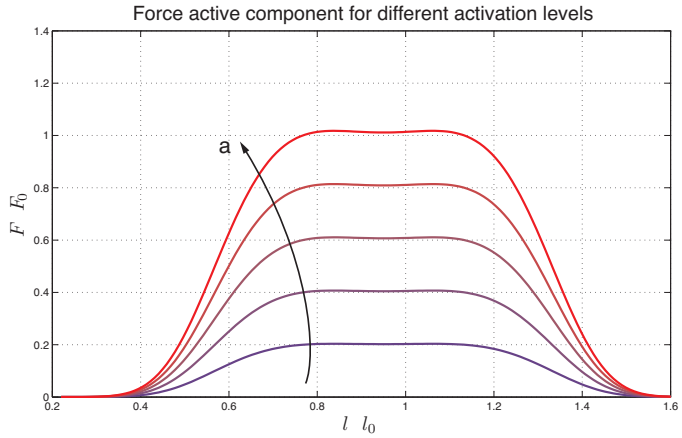

Figure 20: Active contribution of sarcomere force for different activation levels, with null constant contraction velocity. The lower curve corresponds to $a = 0.2$ and the higher one to $a = 1$, with 0.2 steps.

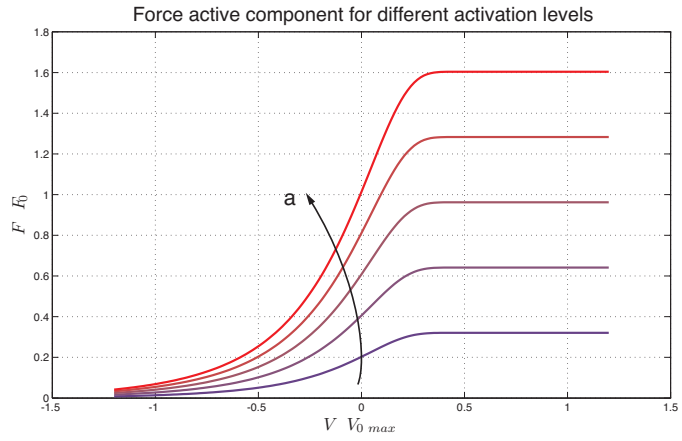

Figure 21: Active contribution of sarcomere force for different activation levels. Sarcomere length is kept constant at l_o. The lower curve corresponds to $a = 0.2$ and the higher one to $a = 1$, with 0.2 steps.

3

INVERSE DYNAMICS

3.1 KINEMATICS INVERSION

3.1.1 *Redundant mechanism*

As thoroughly described above, the model accounts for 7 degrees of freedom of the upper limb. To summarize, they can be identified as

1. arm medial - lateral rotation, i.e. rotation of the humerus about local x-axis
2. arm flexion - extension, i.e. rotation of the about local global y-axis
3. arm abduction - adduction, i.e. rotation of humerus about local z-axis
4. elbow flexion - extension, i.e. rotation of ulna and radius about local y-axis
5. hand prono - supination, i.e. relative rotation of ulna and radius about local x-axis
6. hand radial and ulnar deviation, i.e. rotation of hand about local z-axis
7. hand flexion - extension, i.e. rotation of hand about local y-axis

In order to be able to compute the joint torques needed to perform a task or, equivalently, to follow a known hand trajectory, time histories for all the joint coordinates position, velocity and acceleration must be imposed in an inverse-dynamics problem.

The kinematics of the model is, though, under-constrained, since by imposing the trajectory of the hand a maximum of 6 prescribed motions through rehonomic constraints can be written. The system has thus infinite equivalent solutions, i.e. that result in the same hand trajectory. Since the hand can be considered as the end-effector of the system, the

equivalence means also that the same task is reached.

Four rigid bodies are present in the model, for a total of 24 degrees of freedom, and 17 non-linear algebraic constraint equations approximate the articular joints. Their corresponding equations are summarized in

$$\boldsymbol{\Phi}(\mathbf{q}) = 0, \tag{3.1}$$

alongside to those, rehonomic constraints prescribing the trajectory of the hand are

$$\boldsymbol{\psi}(\mathbf{q}) = \overline{\mathbf{q}}_h(t). \tag{3.2}$$

In fully determined systems, for which the number of constraints is equal to the number of degrees of freedom n, kinematics is often resolved at velocity level, by differentiating the last expression with respect to to time, thus obtaining a linear system of n equations in n unknowns at each time instant

$$[\varphi(\mathbf{q},t)_{/q}]\dot{\mathbf{q}} = \begin{bmatrix} [\Phi_{/q}] \\ [\psi_{/q}]\dot{\mathbf{q}} \end{bmatrix} = \begin{Bmatrix} 0 \\ \dot{\overline{\mathbf{q}}}_h(t) \end{Bmatrix} \tag{3.3}$$

Matrix $[\varphi(\mathbf{q},t)_{/q}]$ is square $n \times n$ and full-rank if constraints are well-posed. It can be therefore inverted, to yield

$$\dot{\mathbf{q}} = -[\varphi(\mathbf{q},t)_{/q}]^{-1}\boldsymbol{\varphi}(\mathbf{q},t)_{/t} \tag{3.4}$$

However, if the system is undetermined, $[\varphi(\mathbf{q},t)_{/q}]$ is not square: if m is the number of constraints, it is an $m \times n$ matrix, and no inverse exists in a classical sense.

One way of avoiding this obstable is to augment the system by imposing some kind of additional conditions, and thus resolving a constrained minimization problem at each timestep. Cost functionals can be task- or problem-specific, or have a more general meaning.
As an example of the last kind, the norm of $\dot{\mathbf{q}}$ yields

$$\begin{aligned}&\min\,(J) = \|\dot{\mathbf{q}}\|^2 = \frac{1}{2}\dot{\mathbf{q}}^T\dot{\mathbf{q}}\\&\text{s.t.}\\&\left[\varphi(\mathbf{q},t)_{/\mathbf{q}}\right]\dot{\mathbf{q}} = \dot{\overline{\mathbf{q}}}_h(t)\end{aligned}$$

general coordinates and time dependence of matrix $[\varphi_{/\mathbf{q}}]$ will be dropped for notation concision. The solution is found using Lagrange multipliers [6]:

$$\dot{\mathbf{q}} = [\varphi_{/\mathbf{q}}]^T\left([\varphi_{/\mathbf{q}}][\varphi_{/\mathbf{q}}]^T\right)^{-1}\dot{\overline{\mathbf{q}}}_h = [\varphi_{/\mathbf{q}}]^+\dot{\overline{\mathbf{q}}}_h \tag{3.5}$$

It can be recognized that matrix $[\varphi_{/\mathbf{q}}]^+$ is the Moore-Penrose pseudoinverse of matrix $[\varphi_{/\mathbf{q}}]$.
Equations 3.1-3.2 can be directly solved, for example, using Newton-Raphson's method, solving iteratively

$$[\varphi_{/\mathbf{q}}]\Delta\mathbf{q} = \overline{\mathbf{q}}_h - \varphi(\mathbf{q},t) \tag{3.6}$$

until $\Delta\mathbf{q}$ is zero.

While the minimization of the norm of the velocities is a viable and sometimes desirable solution, a more specific cost function is frequently needed. In the case of the present work, for example, a physical interpretation and justification of the solution given by $[\varphi_{/\mathbf{q}}]^+$ would be difficult to achieve. It would be more interesting to impose additional constraints that can express the maximization of the level of comfort of the motion performed, or of the energetic cost associated with it, or any other kind of penalty function related to the biomechanic problem.

A number of different techniques are available to do so in an efficient way [20, 24, 35, 19], but the one that was regarded as particularly suited for the scope of this work is the one proposed in [12].

Consider a constrained static system, i.e. one with null inertial properties, subject to n springs that acts on its degrees of freedom. The equilibrium of the system is found as the constraints-admissible configuration that minimizes the elastic potential energy of a set of "dummy" springs

$$\min\ (V) = \frac{1}{2}\Delta\mathbf{q}^T[K]\Delta\mathbf{q}$$
$$\text{s.t.}$$
$$\varphi(\mathbf{q},t) = \overline{\mathbf{q}}_h(t)$$

the constraint equations can be linearized to yield

$$[\varphi(\mathbf{q},t)]_{/\mathbf{q}}\Delta\mathbf{q} = \overline{\mathbf{q}}_h(t) - \varphi(\mathbf{q},t) \tag{3.7}$$

and thus the resolution of the system is written as

$$\begin{bmatrix} [K] & [\varphi_{/\mathbf{q}}]^T \\ [\varphi_{/\mathbf{q}}] & 0 \end{bmatrix} \begin{Bmatrix} \Delta\mathbf{q} \\ \boldsymbol{\lambda} \end{Bmatrix} = \begin{Bmatrix} 0 \\ \overline{\mathbf{q}}_h(t) - \varphi(\mathbf{q},t) \end{Bmatrix}. \tag{3.8}$$

When [K] is isotropic and diagonal, the minimum norm solution is found, as can be shown solving the first block row of 3.8 to obtain $\Delta\mathbf{q}$

$$\Delta\mathbf{q} = -[K]^{-1}[\varphi_{/\mathbf{q}}]\boldsymbol{\lambda} \tag{3.9}$$

that substituted into the second block row yields

$$-[\varphi_{/\mathbf{q}}][K]^{-1}[\varphi_{/\mathbf{q}}]^T\boldsymbol{\lambda} = \overline{\mathbf{q}}_h(t) - \varphi(\mathbf{q},t) \tag{3.10}$$

matrix $[\varphi_{/\mathbf{q}}][K]^{-1}[\varphi_{/\mathbf{q}}]^T$ is square and, if not rank deficient, i.e. if [K] is not singular and the constraints are well-posed, can be inverted to obtain $\boldsymbol{\lambda}$

$$\boldsymbol{\lambda} = -([\varphi_{/\mathbf{q}}][K]^{-1}[\varphi_{/\mathbf{q}}])^T(\overline{\mathbf{q}}_h(t) - \varphi(\mathbf{q},t)) \tag{3.11}$$

and finally $\Delta\mathbf{q}$ can be found by back substituting 3.11 into 3.9 to yield

$$\Delta\mathbf{q} = [K]^{-1}[\varphi_{/\mathbf{q}}]^T([\varphi_{/\mathbf{q}}][K]^{-1}[\varphi_{/\mathbf{q}}])^T(\overline{\mathbf{q}}_h(t) - \varphi(\mathbf{q},t)\mathbf{q}) \tag{3.12}$$

it is easy to recognise that this solution is equivalent to 3.6 when [K] is in the form $\gamma[I]$, with γ scalar of arbitrary value. Otherwise, its elements

penalize the motion of the corresponding degrees of freedom.
This method is simple to use and interpret and allows the resolution of the kinematics directly at position level.

In practice, the method allows to weight the motion of the joints by constraining the system with a set of *dummy* springs and solving a static problem at each time step.
The solution of the kinematics of a redundant mechanism is almost always done, according to literature [20, 24, 35], at the velocity level or, as in the method adopted here, at the position level. It is not always clear, though, if the derivatives and primitives of the resulting solution are obtained by numerical differentiation and integration or through other methods. The complete kinematics, i.e. position, velocity and acceleration of all the involved rigid bodies, is needed for the solution of the inverse dynamics problem, but the quality of the solution achieved by pure numerical differentiation or integration can be unfit to solve the inverse dynamics problem with sufficient accuracy, or give inconsistent results.

In particular, in the case of the work here presented, differentiating the time histories of the positions to obtain the velocites time histories, and then repeating the process on the velocities to obtain accelerations, without any control of the quality of the solutions, may yield unacceptable results, as it will be shown using a simple, planar model (Section 3.3).

To reach a solution of higher quality for the kinematic problem, and thus to be able to reliably solve the inverse dynamics problem, a mixed approach has been developed and applied. It is based on a time-marching optimization algorithm, that is subdivided into three phases, one for each subproblem in kinematics inversion.

Each of the three subproblems is undetermined, in case of a kinematically redundant system, and thus additional constraints must be imposed for each of them. At position level, the additional constraints are the ones explained above, and come from dummy elastic elements that connect the rigid bodies, and represent the ergonomy of the motion, as it will be explained in the next Section. At velocity and acceleration levels, the cost function has been defined to take into account both the distance from the numerical derivatives of the reference solution found at positions level and a parameter related to the *quality* of the solution, in a sense that is shown further on.

3.2 COMPLETE KINEMATICS INVERSION FOR A REDUNDANT SYSTEM

3.2.1 *Positions problem resolution*

As mentioned earlier, the inversion of the kinematics at this level is done by referring to an equivalent static system subjected to springs that act as penalty functions associated with the motion of the joint they act upon. At each time step, the cost function is associated with the elastic energy stored in the springs.

Let E_p be the potential energy of the "dummy" springs; differentiating it yields the elastic force at each time step

$$\frac{\partial E_p}{\partial \mathbf{q}} = [K(\mathbf{q})](\mathbf{q} - \mathbf{q}_0) \tag{3.13}$$

The cost functional can be defined by augmenting E_p with a term proportional to the distance from the solution of the previous time step,

$$J_s = E_p + w_q(\mathbf{q} - \mathbf{q}_{prev})[M](\mathbf{q} - \mathbf{q}_{prev}) \tag{3.14}$$

$\mathbf{q}_{prev}$ is the position at the previous timestep; w_q is a weighting coefficient. A reference solution $\mathbf{q}_0$ can be used, and can be thought, e.g. as a tentative, possibly not constraint-consistent solution. It can also be thought as the solution that minimizes a certain cost function imposed through the stiffness of elastic elements in a static system, in analogy with the 3.12, in a system not subjected to algebraic constraints.

Using Lagrange multipliers the problem becomes

$$([K(\mathbf{q})] + [M]w_q)\mathbf{q} + [\varphi_{/\mathbf{q}}]\lambda^T = [K]\mathbf{q}_0 + w_q[M]\mathbf{q}_{prev} \tag{3.15a}$$

$$\varphi(\mathbf{q}, t) = \overline{q}_h \tag{3.15b}$$

Equations 3.15 constitute a nonlinear algebraic set of equations that can be solved by well-known methods, such as Newton - Raphson's method. Matrix $[K(\mathbf{q})]$ is thus not explicitly defined, but rather extracted from the stiffness characteristics of special elastic elements applied to the relative degrees of freedom of the rigid bodies. In this way, penalty

coefficients related to joint motion can be imposed in a intuitive way, and they can be functions of physical properties of the system.

In the case at focus here, it seems appropriate to relate the choice of the elastic elements to physiological quantities, and to refer their stiffness to some parameter that can represent the likeliness of the solution with respect to actual human motion. In this regard, cost functions found in literature vary greatly, and no general consensus is found: functions used include total joints torque, total joints torque rate of change, minimum hand jerk, hand contact forces combined with muscle's force total rate of change [39], weighted minimization of joint velocities [50].

In the work of Pennestrì et al. [42] it is proposed to solve the kinematic indetermination minimizing the level of discomfort of the instantaneous configuration of the upper limb, using a weighted distance of the joints angular positions from their respective intermediate position, considered the most ergonomic one. The minimum of the cost function

$$H(\theta) = \sum_i w_i \frac{(\theta_i - \theta_{Mi})^n}{\Delta\theta_i{}^n} \tag{3.16}$$

with n even, is souht at each time instant. In the 3.16 θ_i is the i-th joint coordinate, θ_{Mi} its intermediate value considering physiological articulation's reachable angles,

$$\Delta\theta_i = \frac{\theta_{max} - \theta_{min}}{2} \tag{3.17}$$

the amplitude of joint's allowed rotation.

A discomfort cost function of this kind can be indirectly implemented in MBDyn using deformable rotational elements applied to relative rotations of upper limb bones. The stiffness of the elastic elements can be chosen to be in the form of cost function associated to each joint in the 3.16. Since the software requires to define the elastic element's constitutive law, the elastic force as a function of the element strain must be defined, which leads in this case to a constitutive law in the form

$$f_i(\epsilon) = \overline{w}_i(\epsilon - \epsilon_0)^{(n-1)} + c \tag{3.18}$$

being c an arbitrary constant, that in this case can be neglected. The reason to neglet c is that, as noted in Section 3.1, a uniform isotropic system of linear springs does not produce a change in the solution.

Using such a constitutive law is however not possible, since the stiffness of the elastic elements associated, computed as the derivative of the force with respect to the strain, vanishes at $\theta = \theta_0$ or, equivalently, $\epsilon = \epsilon_0$. The addition of a linear term is needed, yielding

$$f_i(\epsilon) = \overline{w}_{1i}(\epsilon - \epsilon_0) + \overline{w}_{2i}(\epsilon - \epsilon_0)^{(n-1)} \tag{3.19}$$

to assure that in every configuration matrix $[K(\mathbf{q})]$ is not singular and can be inverted.

This method is very easy to implement and control. Its interpretation is straightforward, but is not related to physiological quantities, and seems rather arbitrary. To better connect the evalutation of the discomfort level to the biomechanics of the limb, a modification of the criterion has been considered.

According to data published in [25], mean muscular stress possesses the best correlation with the postural configuration indicated by subjets as the most comfortable. Since the inversion of the dynamics of the system is needed to compute the activation coefficients, though, total muscle force is not available at every timestep in the model.

Passive muscular force is, however, only a function of muscular strain, and it is almost zero until the muscle is stretched to a length superior to the one at which it produces the maximum isometric force, after which it shows a steep increase in slope. If several muscles present a relevant passive force component, thus, it is conceivable that the limb is approaching a discomfortable, and therefore less probable, configuration.

3.2.2 *Velocity problem resolution*

The velocity subproblem in the kinematic inversion of a redundant mechanism such as the upper limb, is again undetermined, as noted previously, and cannot be solved in the form of the 3.3. Additional constraints must be imposed, and consistency with the solution found

through system 3.15 must be assured. The derivative with respect to time of the 3.15 is

$$[R](\dot{q} - \dot{q}_0) + [\varphi_{/q}]^T \lambda = 0 \tag{3.20a}$$

$$[\varphi_{/q}]\dot{q} = \dot{\overline{q}}_h \tag{3.20b}$$

equivalent to the minimization of

$$J_s = \frac{1}{2}(\dot{q} - \dot{q}_0^T)[R](\dot{q} - \dot{q}_0)$$

s.t.

$$\varphi(q, t) = \overline{q}_h(t)$$

In this case, $\dot{q}_0$ is the numerical derivative of the solution found in the position step, obtained by numerical differentiation with the first-order approximation

$$\dot{q}_{k+1} = \frac{1 + |\rho_\infty|}{h}(q_{k+1} - q_k) - |\rho_\infty|\dot{q}_k \tag{3.21}$$

With ρ_∞ being the asymptotic spectral radius. Actually, although the more general form is implemented, ρ_∞ was set to zero for algorithmic stability reasons, and thus an implicit Euler's method is used. The cost functional J_s can be aumented as well, in analogy with the position case

$$J_s = \frac{1}{2}(\dot{q} - \dot{q}_0)^T[R](\dot{q} - \dot{q}_0) + w_{\dot{q}}\frac{1}{2}(\dot{q} - \dot{q}_{prev})[M](\dot{q} - \dot{q}_{prev}) \tag{3.22}$$

to weigh the velocity increment (i.e. acceleration) between consecutive timesteps.
The solution of the problem is found by solving the system

$$([R] + w_{\dot{q}}[M])\dot{q} + [\varphi_{/q}]^T \lambda = [R]\dot{q}_0 + w_{\dot{q}}[M]\dot{q}_{prev} \tag{3.23a}$$

$$[\varphi_{/q}]\dot{q} = \dot{\overline{q}}_h \tag{3.23b}$$

that can be put in matrix form as

$$\begin{bmatrix} [R] + w_{\dot{q}}[M] & [\varphi_{/q}]^T \\ [\varphi_{/q}] & [0] \end{bmatrix} \begin{Bmatrix} \dot{q} \\ \lambda \end{Bmatrix} = \begin{Bmatrix} [R]\dot{q}_0 + w_{\dot{q}}[M]\dot{q}_{prev} \\ \dot{\overline{q}}_h \end{Bmatrix} \tag{3.24}$$

In this case, matrix [R] has not a simple and clearly identifiable physical meaning, and can be set equal to the identity matrix, or to an arbitrary diagonal matrix of weights.

3.2.3 *Accelerations problem resolution*

Using the same approach,

$$[M](\ddot{\mathbf{q}} - \ddot{\mathbf{q}}_0) + [\varphi_{/\mathbf{q}}]^T \boldsymbol{\lambda} = \mathbf{0} \tag{3.25a}$$

$$[\varphi_{/\mathbf{q}}]\ddot{\mathbf{q}} = \ddot{\overline{q}}_h - ([\varphi_{/\mathbf{q}}]\dot{\mathbf{q}})_{/\mathbf{q}}\dot{\mathbf{q}} \tag{3.25b}$$

Also in this case the cost functional is made of two terms, one implying minimum distance between the reference solution, computed as in the previous case, with

$$\ddot{\mathbf{q}}_{k+1} = \frac{1 + |\rho_\infty|}{h}(\dot{\mathbf{q}}_{k+1} - \dot{\mathbf{q}}_k) - |\rho_\infty|\ddot{\mathbf{q}}_k \tag{3.26}$$

$$J_s = \frac{1}{2}(\ddot{\mathbf{q}} - \ddot{\mathbf{q}}_0)^T[M](\ddot{\mathbf{q}} - \ddot{\mathbf{q}}_0) + w_{\ddot{\mathbf{q}}}\frac{1}{2}(\ddot{\mathbf{q}} - \ddot{\mathbf{q}}_{prev})^T[M](\ddot{\mathbf{q}} - \ddot{\mathbf{q}}_{prev}) \tag{3.27}$$

that combines the weight of distance from the reference solution together with difference in acceleration between two consecutive timesteps (i.e. a quantity indirectly related to the jerk).
The system that has to be solved becomes

$$(1 + w_{\ddot{\mathbf{q}}})[M]\ddot{\mathbf{q}} + [\varphi_{/\mathbf{q}}]^T\boldsymbol{\lambda} = [M]\ddot{\mathbf{q}}_0 + w_{\ddot{\mathbf{q}}}[M]\ddot{\mathbf{q}}_0 \tag{3.28a}$$

$$[\varphi_{/\mathbf{q}}]\ddot{\mathbf{q}} = \ddot{\mathbf{q}}_{prev} - ([\varphi_{/\mathbf{q}}]\dot{\mathbf{q}})_{/\mathbf{q}}\dot{\mathbf{q}} \tag{3.28b}$$

or, in matrix form

$$\begin{bmatrix} (1 + w_{\ddot{\mathbf{q}}})[M] & [\varphi_{/\mathbf{q}}]^T \\ [\varphi_{/\mathbf{q}}] & [0] \end{bmatrix} \begin{Bmatrix} \ddot{\mathbf{q}} \\ \boldsymbol{\lambda} \end{Bmatrix} = \begin{Bmatrix} [M]\ddot{\mathbf{q}}_0 + w_{\ddot{\mathbf{q}}}[M]\ddot{\mathbf{q}}_{prev} \\ \ddot{\overline{q}}_h - ([\varphi_{/\mathbf{q}}]\dot{\mathbf{q}})_{/\mathbf{q}}\dot{\mathbf{q}} \end{Bmatrix} \tag{3.29}$$

In the following section a simple planar model is presented, to exemplify the functionality of the proposed approach.

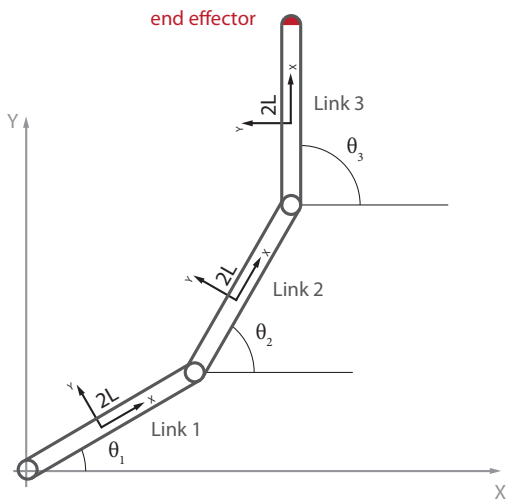

Figure 22: Schematics of the planar manipulator model analyzed in its initial position.

3.3 EXAMPLE: PLANAR 3-LINK ROBOT

A simple planar 3-link manipulator multibody model has been developed, following a redundant set approach. The model is represented in Figure 22 in its initial rest position.
It is constituted by 3 rigid bars, connected with rotational joints at the extremities. The system has 3 degrees of freedom, namely the 3 absolute angles that the bars form with the global x-axis.

Each rigid body carries a reference frame with origin in its center of mass, i.e. its midpoint in this case, and x-axis oriented along its length, defining a node. Their vector of generalized coordinates $\mathbf{q}$ is, thus

$$\mathbf{q}_i = \begin{Bmatrix} x_i \\ y_i \\ \theta_i \end{Bmatrix} \tag{3.30}$$

Each is then assigned inertial parameters, shown in Table 7

Rigid body	2L [m]	M [kg]	J [kg/m^2]	θ_{i0}
Link 1	0.32	1.8	0.015	$\pi/6$
Link 2	0.32	1.6	0.013	$\pi/3$
Link 3	0.32	1.6	0.013	$\pi/2$

Table 7: Planar 3 link mechanism inertial and geometrical parameters. Initial orientation is given by θ_{i0} and is expressed with reference to the global reference system.

The initial configuration of the system is defined by q_{01}, q_{02} and q_{03}

$$\mathbf{q}_{01} = \begin{Bmatrix} L\cos(\pi/6) \\ L\sin(\pi/6) \\ \pi/6 \end{Bmatrix} \tag{3.31a}$$

$$\mathbf{q}_{02} = \begin{Bmatrix} 2L\cos(\pi/6) + L\cos(\pi/3) \\ 2L\sin(\pi/6) + L\sin(\pi/3) \\ \pi/3 \end{Bmatrix} \tag{3.31b}$$

$$\mathbf{q}_{03} = \begin{Bmatrix} 2L\cos(\pi/6) + 2L\cos(\pi/3) \\ 2L\sin(\pi/6) + 2L\sin(\pi/3) + L \\ \pi/2 \end{Bmatrix} \tag{3.31c}$$

3.3.1 *Geometrical constraints*

Rotational joints in a planar system reduce to the coincidence of the points in which they are applied, in the global reference frame. For a joint connecting points P and Q of nodes a and b, whose positions in local reference frames are defined by means of vectors $\tilde{\mathbf{f}}_P$ and $\tilde{\mathbf{f}}_Q$.
They are projected in the global reference frame by means of the rotation matrices associated with the orientation of the nodes

$$\mathbf{f}_P = [R_a]\tilde{\mathbf{f}}_P \tag{3.32a}$$

$$\mathbf{f}_Q = [R_b]\tilde{\mathbf{f}}_Q \tag{3.32b}$$

the rotation matrix in this case is

$$[R] = \begin{bmatrix} \cos\theta & -\sin\theta \\ \sin\theta & \cos\theta \end{bmatrix} \tag{3.33}$$

the constraint equations hence are

$$\phi(\mathbf{q})_{ab} = \mathbf{q}_b + \mathbf{f}_Q - \mathbf{q}_a - \mathbf{f}_P \tag{3.34}$$

that, written in full, become

$$\phi(\mathbf{q}_{ab}) = \begin{Bmatrix} x_a \\ y_a \end{Bmatrix} + \begin{bmatrix} c\theta_a & -s\theta_a \\ s\theta_a & c\theta_a \end{bmatrix} \begin{Bmatrix} L \\ 0 \end{Bmatrix} - \begin{Bmatrix} x_b \\ y_b \end{Bmatrix} - \begin{bmatrix} c\theta_b & -s\theta_b \\ s\theta_b & c\theta_b \end{bmatrix} \begin{Bmatrix} -L \\ 0 \end{Bmatrix} \tag{3.35}$$

For the revolute joint that connects Link 1 to the ground it yields $\mathbf{f}_a = \mathbf{0}$ and $x_a = x_b = 0$.

The trajectory of the end effector is imposed by means of the rehonomic constraint $\varphi(\mathbf{q}, t)$

$$\varphi(\mathbf{q}, t) = \begin{Bmatrix} x_3 \\ y_3 \end{Bmatrix} + \begin{bmatrix} c\theta_3 & -s\theta_3 \\ s\theta_3 & c\theta_3 \end{bmatrix} \begin{Bmatrix} L \\ 0 \end{Bmatrix} = \begin{Bmatrix} \overline{x}_3(t) \\ \overline{y}_3(t) \end{Bmatrix} \tag{3.36}$$

3.3.2 *Position*

The system has 9 degrees of freedom; the algebraic constraint equations $\Phi(\mathbf{q})$ are 6. The trajectory of the endpoint of Link 3 (i.e. the end effector) can be imposed by means of the two equations $\varphi(\mathbf{q}, t)$, making the system 1-dof redundant.
At least an additional condition is therefore needed for its kinematic inversion. It has been chosen to introduce non-linear springs acting on relative rotations between the links, whose force - deformation constitutive law, for a spring connecting nodes a and b, is defined as

$$F(\epsilon) = a\frac{\epsilon}{\theta_{sp}} + b\left(\frac{\epsilon}{\theta_{sp}}\right)^5 \tag{3.37}$$

where θ_{sp} represents the range of motion of the joint, set to π for all three joints, and the angular deformation ϵ is defined with respect to to relative orientation angles, i.e. $\theta_{r,ab} = \theta_b - \theta_a$

$$\epsilon_{ab} = \frac{\theta_{r,ab} - \theta_{ro,ab}}{\theta_{ro,ab}} \tag{3.38}$$

Spring stiffnesses are calculated at each timestep taking the derivative of F with respect to ϵ

$$\frac{\partial F}{\partial \epsilon} = \kappa(\epsilon) = \frac{a}{\theta_{sp}} + \frac{5b}{\theta_{sp}^5}\epsilon^4 \tag{3.39}$$

for each spring. The force as a function of the relative angle is shown in Figure 23

Each elastic element can be seen as a sort of *ergonomic* constraint for the i-th joint relative rotation, and acts to modify the solution by penalizing the motion of the joint it acts upon. This modification takes place in the null space of the Jacobian matrix, as to mantain an equivalent end-effector trajectory.

The total elastic energy is

$$V = \frac{1}{2}\boldsymbol{\epsilon}(\mathbf{q})^T[K]\boldsymbol{\epsilon}(\mathbf{q}) \tag{3.40}$$

In Figure 23 the constitutive law of the rotational springs is shown.

The cost function for the solution of the position subproblem is then composed by the sum of two terms: the total elastic energy of the springs and the distance from the previous step's solution.

$$J_p = V + (\mathbf{q} - \frac{1}{2}\mathbf{q}_{prev})^T[I](\mathbf{q} - \mathbf{q}_{prev}) \tag{3.41}$$

in this case, the identity matrix has been choosen as weight matrix for the cost applied to the distance from the previous step.

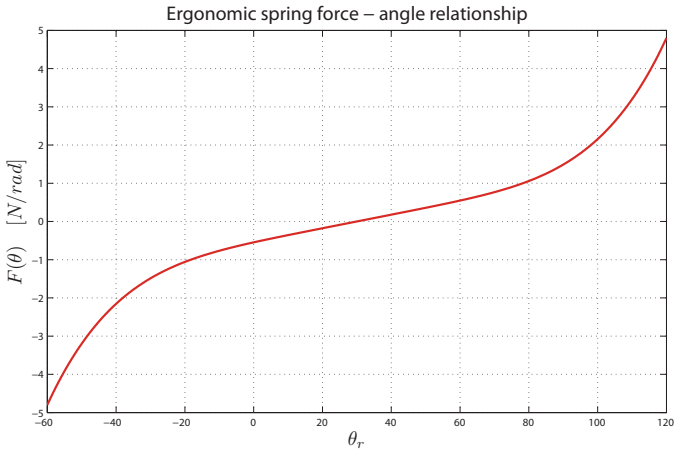

Figure 23: Ergonomic spring force as a function of relative angle between two nodes.

3.3.3 *Velocity*

To solve the velocity subproblem with the approach of Section 3.2.2, the derivatives of the constraints must be computed. Geometrical constraints derivative, i. e. the Jacobian matrix $[\Phi_{/q}]$ block, for a revolute joint connecting nodes a and b is

$$[\Phi_{/q_{ab}}] = \begin{bmatrix} 1 & 0 & -L\sin\theta_a & -1 & 0 & -L\sin\theta_b \\ 0 & 1 & L\cos\theta_a & 0 & -1 & L\cos\theta_b \end{bmatrix} \tag{3.42}$$

The grounded revolute joint situated in global reference frame origin, the block reduces to a 2×3 matrix

$$[\Phi_{/q_0}] = \begin{bmatrix} 1 & 0 & L\sin\theta_1 \\ 0 & 1 & -L\cos\theta_1 \end{bmatrix} \tag{3.43}$$

while for the rehonomic joint imposing the end-effector velocity, the block will be

$$[\varphi_{/q_e}] = \begin{bmatrix} 1 & 0 & -L\sin\theta_3 \\ 0 & 1 & L\cos\theta_3 \end{bmatrix} \tag{3.44}$$

The Jacobian matrix can now be assembled, collocating the blocks in the correct positions regarding the vector of generalized coordinates. A certain arbitrariness is possible in the choice of generalized coordinates and joint ordering, and the simplest approach possible has been chosen here.
The vector of generalize coordinates is thus constructed as

$$q = \left\{ q_1^T \quad q_2^T \quad q_3^T \right\}^T \tag{3.45}$$

with this choice, and ordering the joints in progressive order too, the resulting Jacobian matrix is

$$\Phi_{/q} = \begin{bmatrix} [\ \Phi_{/q_0}\ ]^{2\times3} & [\ 0\ ]^{2\times6} \\ [\ \Phi_{/q_{12}}\ ]^{2\times6} & [\ 0\ ]^{2\times3} \\ [\ 0\ ]^{2\times3} & [\ \Phi_{/q_{23}}\ ]^{2\times6} \\ [\ 0\ ]^{2\times6} & [\ \Phi_{/q_e}\ ]^{2\times3} \end{bmatrix} \tag{3.46}$$

Imposed end effector velocities are contained in vector $\varphi_{/t}$

$$\varphi_{/t} = \left\{ \{0\}^{1\times6} \quad \dot{\bar{x}}_e \quad \dot{\bar{y}}_e \right\}^T \tag{3.47}$$

After computing the reference velocities as numerical derivatives of the positions with the 3.21, the cost function for the velocity subproblem is the one from eq. 3.22, in wich identity matrices have been chosen as weights for the two components of the functiona.

3.3.4 *Acceleration*

Jacobian matrix derivative $([\varphi_{/q}]\dot{q})_{/q}$ is needed to solve the acceleration problem. For the system considered, it reads, changed in sign to match the formulation of the 3.28

$$-([\varphi_{/q}]\dot{q})_{/q} = \begin{Bmatrix} -\dot{\theta}_1^2 L\cos\theta_1 \\ -\dot{\theta}_1^2 L\sin\theta_1 \\ \dot{\theta}_1^2 L\cos\theta_1 + \dot{\theta}_2^2 L\cos\theta_2 \\ \dot{\theta}_1^2 L\sin\theta_1 + \dot{\theta}_2^2 L\sin\theta_2 \\ \dot{\theta}_2^2 L\cos\theta_2 + \dot{\theta}_3^2 L\cos\theta_3 \\ \dot{\theta}_2^2 L\sin\theta_2 + \dot{\theta}_3^2 L\sin\theta_3 \\ \dot{\theta}_3^2 L\cos\theta_1 + \ddot{x}_e \\ \dot{\theta}_3^2 L\sin\theta_1 + \ddot{y}_e \end{Bmatrix} \tag{3.48}$$

The acceleration problem is solved with the formulation of Section 3.2.3

Also in this case it is necessary to the compute numerical derivatives of the solution at the previous step, with the 3.26. The cost functional is the analogous to the one of eq.3.27, and again the identity matrix has been chosen to weigh its two terms.

3.3.5 *Tracking example*

To show the aspects of the kinematic inversion related to the choice of the deformable element's stiffness, a simulation has been carried out, imposing to the end effector of Link 3 to follow the trajectory shown in Figure 24. For a complete kinematics inversion, also the components of the velocity and acceleration of the end effector must be given. The imposed position, velocity and acceleration components are shown in Figure 25.

Initially, a prestrain $\epsilon_0 = \pi/6$ is given to all three springs, so that the system is initially in its static equilibrium position, and the system evolves from it.

If the prestrain is instead set to 0, the initial configuration is not an equilibrium position anymore, and the system reacts by modifying it in the first few time steps (2, in case of a time step of 10^{-3} s , changing

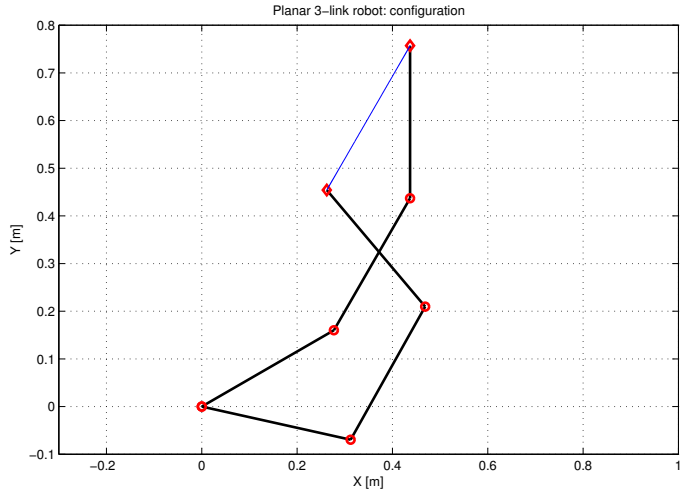

Figure 24: Imposed trajectory of the end effector of Link 3 in the X-Y plane.

relative angles between the links. Also the trajectories vary, to find the minimum of the potential energy of the springs at each time step.

MBDyn allows the user to set a prestrain parametrized with time, and by using such a prestrain that starts from a null value, to get to $\pi/6$ as the end-effector gets to its final position, with a continuous progress, one would expect to find a solution that starts from the one found with $\epsilon_0 = 0$ and evolves with continuity to reach the one found with $\epsilon_0 = \pi/6$. This expectation is indeed confirmed. To exemplify it the trajectory of the node of Link 2 is plotted in the three cases, in Figure 27.

The simple planar model will be used further on to demostrate in a simple environment other aspects related to the various phases of the dynamic inversion and muscle forces identification of the human upper limb model.

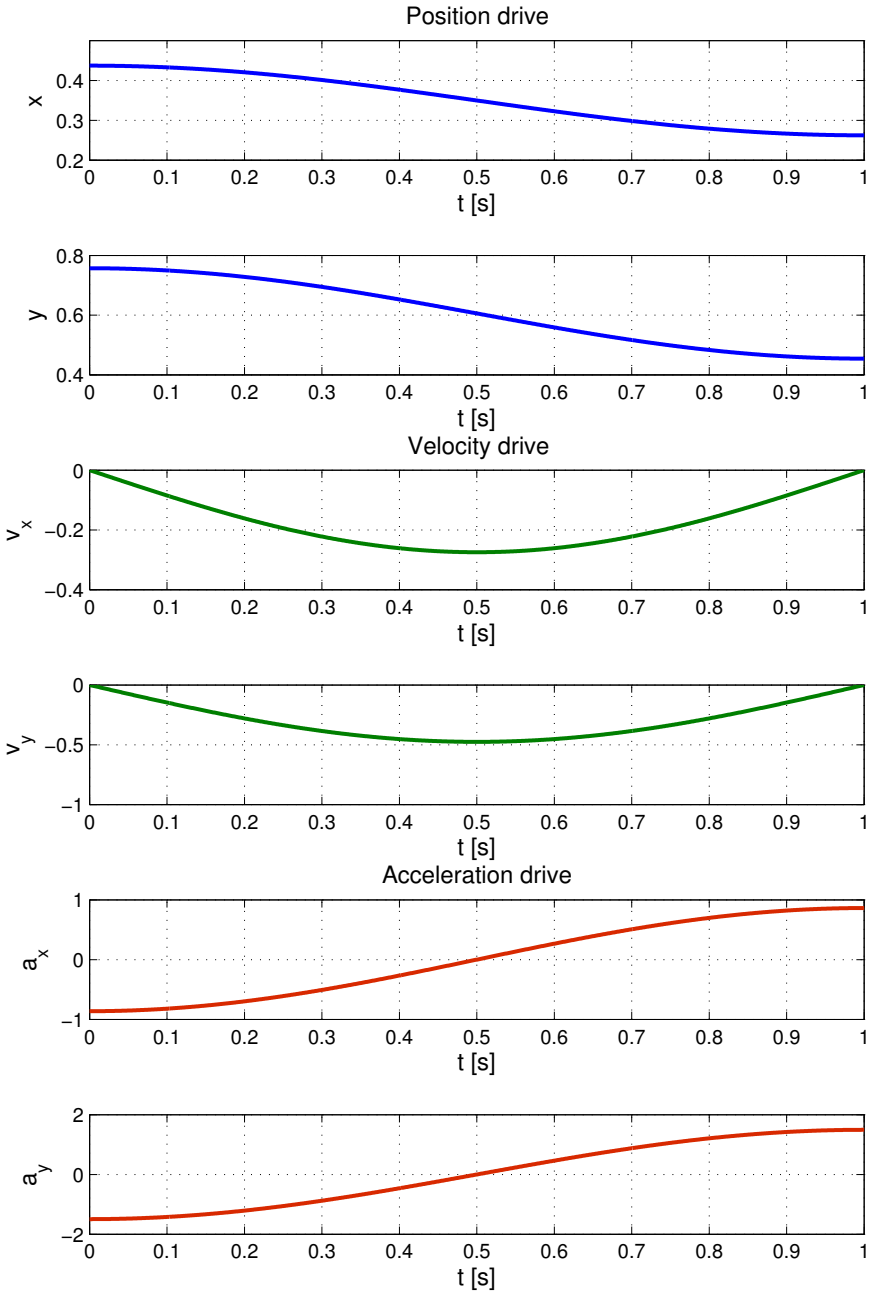

Figure 25: Imposed position, velocity and acceleration components of the end effector of Link 3.

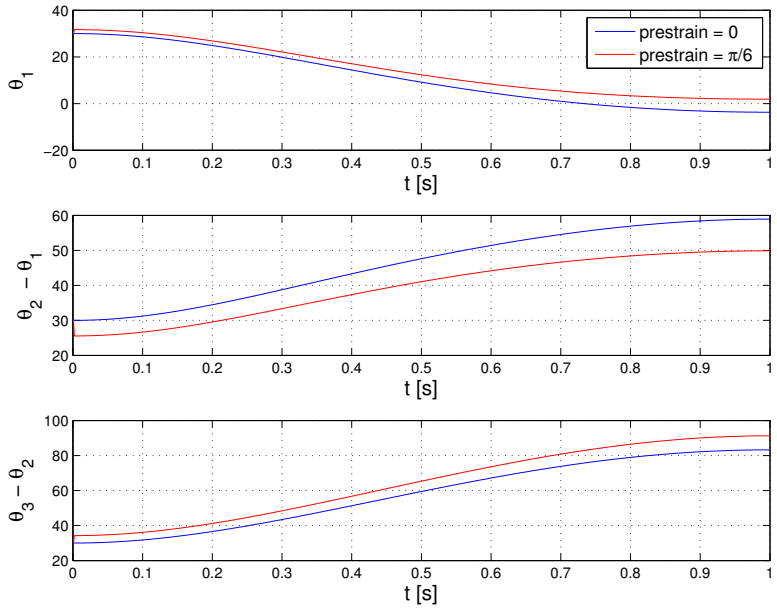

Figure 26: Relative angles between the links, with different initial prestrain applied to the non - linear elastic elements that represent the discomfort functions. The solution changes to find the new local minimum of the potential energy stored in the springs.

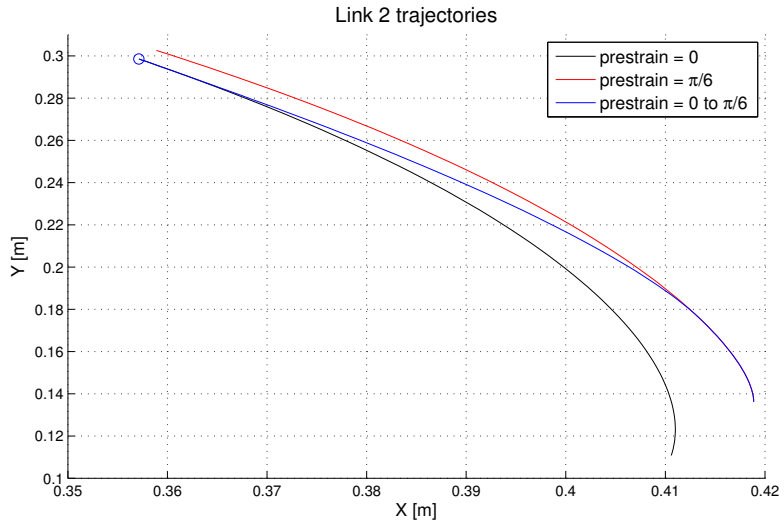

Figure 27: Solutions comparison for the planar 3 link robot, subjected to the action of rotational springs with different initial prestrain.

3.4 INVERSE DYNAMICS

Once the complete kinematics of the system is known, the solution can be used to invert the system dynamics. This process is needed to find the actions, i.e. the joint couples, that are needed to perform the prescribed task.

These torques are imposed in joint-space coordinates, defined by means of the non linear transformation

$$\vartheta(\mathbf{q}) = \theta \tag{3.49}$$

The problem can be posed, in a general way, as the solution of the system

$$[M]\ddot{\mathbf{q}} + [\Phi_{/\mathbf{q}}]^T\boldsymbol{\lambda} + [\vartheta_{/\mathbf{q}}]^T\mathbf{c} = \mathbf{f} \tag{3.50}$$

where matrix $[\vartheta_{/\mathbf{q}}]$ is the Jacobian matrix of the joint space coordinates, and also represents the Jacobian matrix of the joint torques. By definition

$$[\Phi_{/\mathbf{q}}][\vartheta_{/\mathbf{q}}]^+ = [0] \tag{3.51}$$

When the joint coordinates are directly prescribed, $[\vartheta_{/\mathbf{q}}] \equiv [\varphi_{/\mathbf{q}}]$. In this case, though, as in general only hand trajectory and its derivatives can be imposed, the equality does not hold.

In the system 3.50, accelerations are known from the solution of the inverse kinematics problem, and so vector $[M]\ddot{\mathbf{q}}$ can be brought to the right side, yielding

$$\begin{bmatrix} \Phi_{/\mathbf{q}} \\ \vartheta_{/\mathbf{q}} \end{bmatrix}^T \begin{Bmatrix} \boldsymbol{\lambda} \\ \mathbf{c} \end{Bmatrix} = \mathbf{f} - [M]\ddot{\mathbf{q}} \tag{3.52}$$

the solution of the system yields the vector $\mathbf{c}$ representing the instantaneous torques acting on the system, expressed by means of the joint coordinates θ.

The torques $\mathbf{c}$ are thus the actions needed to obtain the motion prescribed by the imposed hand trajectory, with the arm subjected to external forces and, optionally, muscle passive forces.

Vector $\mathbf{c}$ is $(n - r) \times 1$ dimensional, n being the total generalized coordinates number, and r the total number of constraints. Calling ϕ the constraints' Jacobian matrix, this means that $rank(\phi) = r$. In this case $r = 7$.

3.5 MUSCLE FORCES IDENTIFICATION

The muscle fascicula are 25, and so 25 individual muscular forces are to be found, that together reproduce the 7 components of $\mathbf{c}$. The problem is therefore overactuated, and can be resolved by minimizing some norm of the muscles's activations.

The goal of this phase is to find the activation patterns required to produce joint couples so that

$$\mathbf{c} = [\vartheta^{+}_{/\mathbf{q}}]^{T}[B(\mathbf{q})]\mathbf{f}_{m} \tag{3.53}$$

Matrix $[\vartheta^{+}_{/\mathbf{q}}]^{T}$ represents the transpose of the Moore-Penrose pseudoinverse of joint space coordinates' Jacobian matrix $[\vartheta_{/x}]$, and projects muscle forces' moments into joint-space coordinates, while matrix $[B]$ represents the effect of muscle forces on the system's generalized coordinates. Since all of the muscles are modeled as one-dimensional deformable elements, its columns basically contain the arms of the forces with respect to the nodes.

Muscle forces are, as seen in Chapter 2 are functions of the state of the system, and of the activation parameters. Since the state of the system is known at each instant of time, the only free parameters are the a_i activation coefficients.

The forces can be separated into a passive and an active component, in which the dependency from the voluntary coefficients resides

$$\mathbf{f} = [F_{0m}](\mathbf{f}_0(\mathbf{q}) + [F_a(\mathbf{q}, \dot{\mathbf{q}})]\mathbf{a}) \tag{3.54}$$

with $[F_{0m}]$ and $[F_a]$ diagonal matrices

$$[F_{0m}] = F_0 \begin{bmatrix} f_{31} & & & \\ & f_{32} & & \\ & & \ddots & \\ & & & f_{3n} \end{bmatrix} \tag{3.55a}$$

$$[F_a] = F_0 \begin{bmatrix} f_{11}f_{21} & & & \\ & f_{12}f_{22} & & \\ & & \ddots & \\ & & & f_{12}f_{2n} \end{bmatrix} \tag{3.55b}$$

functions $_{1i}$, f_{3i} and f_{3i} are the 2.17, 2.18 and 2.16 equations for the $i-th$ muscle.

As a consequence, the contribution of the muscle forces to the joint torques vector is separable in two distinct components, one depending only on the state of the system, and therefore known, and a second one depending on muscle activation

$$\begin{aligned} \mathbf{c} = \mathbf{c}_0 + \mathbf{c}_a \quad &= [\vartheta^+_{/\mathbf{q}}]^T[B(\mathbf{q})][F_{0m}]\mathbf{f}_0 + [\vartheta^+_{/\mathbf{q}}]^T[B(\mathbf{q})][F_a(\mathbf{q},\dot{\mathbf{q}})]\mathbf{a} \\ &= [B_0(\mathbf{q})]\mathbf{f}_0 + [B_a(\mathbf{q},\dot{\mathbf{q}})]\mathbf{a} \end{aligned} \tag{3.56}$$

The minimization problem can be stated with respect to the total activation given by vector $\mathbf{a}$ and three kind of constraint conditions are to be imposed:

- muscle forces, projected in the joint coordinates space, must produce the desired joint torques;
- the torques resulting from muscle forces must be consistent with geometrical constraints;
- Activation parameter a_i value is bounded between 0 and 1.

The second condition is already satisfied by the position of the problem in joint-space coordinates, and so only the first and the last one remain.

The problem can be stated as

$$\begin{aligned} &\min\ (J_s) \\ &\text{s.t.} \end{aligned}$$

$$[B_a(\mathbf{q}, \dot{\mathbf{q}})]\mathbf{a} - \mathbf{c_a} = 0 \tag{3.57a}$$

$$\phi^T_{/\mathbf{q}}\mu = 0 \tag{3.57b}$$

$$0 \leqslant a \leqslant 1 \tag{3.57c}$$

Many different choices are possible for the definition of J_s, ranging from total activation, total muscle force and total muscle fatigue, to more complex functions describing the instantaneous variation of metabolic cost.[40]

In this work, a simple cost function representing the total activation has been chosen. The cost functional therefore has been defined as

$$J_s = \frac{1}{2}\mathbf{a}^T[W]\mathbf{a} \tag{3.58}$$

where [W] is an optional weight matrix, that can be set to give more importance during the minimization to some muscular bundles with respect to the others. It was initially set to the identity matrix, and is always diagonal.

Not considering the bounding condition 3.57c for a moment, the new functional for constrained minimization becomes, using Lagrange multipliers

$$J = \frac{1}{2}\mathbf{a}^T[W]\mathbf{a} + \boldsymbol{\mu}^T([B_a]\mathbf{a} - \mathbf{c}_a) \tag{3.59}$$

the vector $\mathbf{a}_{min}$ that minimizes J is found via the solution of the system

$$\begin{bmatrix} W & B_a^T \\ B_a & 0 \end{bmatrix} \begin{Bmatrix} \mathbf{a} \\ \boldsymbol{\mu} \end{Bmatrix} = \begin{bmatrix} 0 \\ \mathbf{c}_a \end{bmatrix} \tag{3.60}$$

solving the first block row for $\mathbf{a}$

$$\mathbf{a} = [W]^{-1}[B_a]\boldsymbol{\mu} \tag{3.61}$$

and substituting into the second block row to find $\boldsymbol{\mu}$

$$\boldsymbol{\mu} = -([B_a][W]^{-1}[B_a])^{-1}\mathbf{c_a} \tag{3.62}$$

that brings to

$$\boldsymbol{a}_{min} = [W]^{-1}[B_a]^T(-[B_a][W]^{-1}[B_a])^{-1}\mathbf{c_a} \tag{3.63}$$

It is easy to notice that if $[W]$ is chosen to be the identity, the 3.63 becomes really simple

$$\boldsymbol{a}_{min} = [B_a]^{\dagger}\mathbf{c}_a \tag{3.64}$$

that is the least-squares solution on the total activation.
This is not the actual method that was used to find the activation coefficients, since it does not take into account the restriction 3.57c. The system could be solved by computing the residual of the i-th equation in which a is out of the boundaries, associated with the quota of a_i that exceeds 1 or is less than zero. However, to find activation coefficients, a generic non-linear constrained minimization solver implemented in *MATLAB*® has been used in this work.

To be able to solve system 3.57, the projector $[\varphi^{+}_{/\mathbf{q}}]^T$ and matrix $[B]$ need to be built for the model.

3.5.1 *Matrix [B]*

The single $j-th$ muscle bundle force has an influence on the component of torque relative to the $i-th$ generalized coordinate quantified by the b_{ij} element of $[B]$. So the elements of $[B]$ are the relative arms of the muscle bundles' forces, projected in the global reference frame. They can be easily derived from the definition of the deformable joint with which the muscle are modeled.

Let $\mathbf{x}_a$ and $\mathbf{x}_b$ be the positions of the nodes connected by the muscle, and $\mathbf{f}_P$ and $\mathbf{f}_Q$ the relative offsets of the attach points, in the local reference frame of node a and b, respectively. The distance that separates these two points is

$$\mathbf{l} = \mathbf{x}_b + \mathbf{f}_Q - \mathbf{x}_a - \mathbf{f}_P \tag{3.65}$$

the norm of it being $l = \sqrt{\mathbf{l}^T\mathbf{l}}$. The scalar force that the two nodes exchange is $f = f(\epsilon, \dot{\epsilon})$, so that the vector force becomes

$$\mathbf{F} = \frac{\mathbf{l}}{l} f \tag{3.66}$$

The virtual work of the force is

$$\delta L = \delta \mathbf{l}^T \frac{\mathbf{l}}{l} f = (\delta \mathbf{x}_b - \mathbf{f}_Q \times \boldsymbol{\theta}_{b\delta} - \delta \mathbf{x}_a + \mathbf{f}_P \times \boldsymbol{\theta}_{a\delta}) \frac{\mathbf{l}}{l} f \tag{3.67}$$

so the forces and moments on the nodes are

$$\delta \mathbf{F}_a = -\delta \mathbf{F} \tag{3.68a}$$
$$\delta \mathbf{M}_a = -\mathbf{f}_P \times \delta \mathbf{F} - \mathbf{F} \times \mathbf{f}_P \times \boldsymbol{\theta}_{a\delta} \tag{3.68b}$$
$$\delta \mathbf{F}_b = \delta \mathbf{F} \tag{3.68c}$$
$$\delta \mathbf{M}_b = \mathbf{f}_Q \times \delta \mathbf{F} + \mathbf{F} \times \mathbf{f}_Q \times \boldsymbol{\theta}_{b\delta} \tag{3.68d}$$

and the linearized force

$$\delta \mathbf{F} = \frac{f}{l} \left([I] - \frac{\mathbf{l}\mathbf{l}^T}{l^2} \right) \delta \mathbf{l} + \frac{\mathbf{l}}{l} \delta f \tag{3.69}$$

in this case the only dependence of f is the activation parameter, so

$$\delta \mathbf{F} = \frac{\mathbf{l}}{l} f_{/a} \delta a \tag{3.70}$$

and finally the 3.68 can be rewritten as

$$\delta \mathbf{F}_a = -\frac{\mathbf{l}}{l} f_{/a} \delta a \tag{3.71a}$$
$$\delta \mathbf{M}_a = -\mathbf{f}_P \times \frac{\mathbf{l}}{l} f_{/a} \delta a \tag{3.71b}$$
$$\delta \mathbf{F}_b = \frac{\mathbf{l}}{l} f_{/a} \delta a \tag{3.71c}$$
$$\delta \mathbf{M}_b = \mathbf{f}_Q \times \frac{\mathbf{l}}{l} f_{/a} \delta a \tag{3.71d}$$

so the generic column of matrix $[B]$ is

$$\left[-\frac{\mathbf{l}}{l} \;\vdots\; -\mathbf{f}_P \times \frac{\mathbf{l}}{l} \;\vdots\; \frac{\mathbf{l}}{l} \;\vdots\; \mathbf{f}_Q \times \frac{\mathbf{l}}{l} \right]^T \tag{3.72}$$

3.5.2 *Joint space projection matrix*

The model has been built using a particularly flexible joint element that MBDyn offers, called `total joint`. It is a scalable element that can impose the desired number of constraint equations to the relative motion of two nodes, and can also be used to impose components of their relative displacement, velocity and acceleration.

So all the rehonomic constraints in the model are `total` joints, and matrix $[\vartheta^{+}_{/q}]^{T}$ can be derived from the joint's equations. [1]

Let's consider the joint acting on nodes a and b, whose positions in the global reference frame are x_a and x_b, on reference frames rigidly attached to the nodes, with origins in points P and Q, with offsets with respect to the nodes, in the global reference frame

$$f_P = [R_a]\tilde{f}_P \tag{3.73a}$$
$$f_Q = [R_b]\tilde{f}_Q \tag{3.73b}$$

It is possible to express the position constraint in a reference frame connected to node a and having orientation defined by matrix $[\tilde{R}_{ah}]$ in the local reference frame, so that in the global reference frame it becomes

$$[R_{ah}] = [R_a][\tilde{R}_{ah}] \tag{3.74}$$

Orientation constraint can be expressed in a reference frame rigidly connected to both nodes, having orientation in the global reference frame

$$[R_{ahr}] = [R_a][\tilde{R}_{ahr}] \tag{3.75a}$$
$$[R_{bhr}] = [R_b][\tilde{R}_{bhr}] \tag{3.75b}$$

matrices $[\tilde{R}_{ahr}]$ and $[\tilde{R}_{bhr}]$ are constant, so differentiation of constraint equations does not affect them.

The relative position between the nodes is therefore expressed as

$$[R_{rel}] = [R_{ahr}]^{T}[R_{bhr}] \tag{3.76}$$

1 This section refers extensively to MBDyn's tecnical manual, available at http://www.aero.polimi.it/mbdyn.

and the imposed relative orientation can be indicated by means of Euler's vector $\boldsymbol{\varphi}_0$, that is related to its corresponding rotation matrix by the relation

$$\boldsymbol{\varphi}_0 = ax\left(exp^{-1}([R_0])\right) \tag{3.77}$$

imposing $\boldsymbol{\varphi}_0$ as the relative orientation means constraining $[R_{rel}]$ and $[R_0]$ to be equal

$$[R_{rel}][R_0]^T = [I] \tag{3.78}$$

and so, the difference between the desired rotation and the current relative orientation can be written as

$$[R_{rel}][R_0]^T = [R^\delta] \tag{3.79}$$

and requiring $[R^\delta] = [I]$ implies requiring

$$\boldsymbol{\varphi}^\delta = ax\left(exp^{-1}([R^T_{ahr}][R_{bhr}][R^T_0])\right) = 0 \tag{3.80}$$

The position constraint can, on the other hand, be expressed as

$$\boldsymbol{x} = [R_{ah}]^T\left(\boldsymbol{x}_b + \mathbf{f}_Q - \boldsymbol{x}_a - \mathbf{f}_P\right) \tag{3.81}$$

and the difference between the desired relative position and the actual relative position is

$$\boldsymbol{x}^\delta = \boldsymbol{x} - \boldsymbol{x}_0 \tag{3.82}$$

The constraint equations will thus be written in the simple form

$$\boldsymbol{x}^\delta = 0 \tag{3.83a}$$
$$\boldsymbol{\varphi}^\delta = 0 \tag{3.83b}$$

Any component of the constraint equations can be individually set to zero, and the imposed relative rotations can be set with the use of vectors $\boldsymbol{\varphi}_0$ and $\boldsymbol{x}_0$

The perturbation of the 3.83a yields

$$\delta \boldsymbol{x}^{\delta} = [R_{ah}]^T \left(\delta \boldsymbol{x}_b - \boldsymbol{f}_Q \times \delta \boldsymbol{\theta}_b - \delta \boldsymbol{x}_a + (\boldsymbol{x}_b + \boldsymbol{f}_Q - \boldsymbol{x}_a) \times \delta \boldsymbol{\theta}_a \right) \quad (3.84)$$

Perturbation of $\boldsymbol{\varphi}^{\delta}$ brings to

$$\delta \boldsymbol{\varphi}^{\delta} = [R_{ahr}]^T \left(\delta \boldsymbol{\theta}_b - \delta \boldsymbol{\theta}_a \right) \times [R_{ahr}] \quad (3.85)$$

thus, redefining

$$\boldsymbol{b}_1 = \boldsymbol{x}_b + \boldsymbol{f}_Q - \boldsymbol{x}_a \quad (3.86)$$

and so the joint contribute to the Jacobian matrix $[\vartheta_{/q}]^T$ is

$$[\vartheta_{/q}]_i^T = \begin{bmatrix} -[R_{ah}]^T & [R_{ah}]^T \boldsymbol{b}_{1\times} & [R_{ah}]^T & -[R_{ah}]^T \boldsymbol{f}_{Q\times} \\ [0] & -[R_{ahr}]^T & [0] & [R_{ahr}]^T \end{bmatrix} \quad (3.87)$$

3.6 MODEL VALIDATION

To validate the multibody model and the muscle forces' identification method, two kinds of simulations have been performed.

The first one aims at estimating the maximum moment in isometric conditions that the appropriate set of muscles can generate, with respect to a given joint rotation; the subsequent one evaluates the activation patterns of muscles in case of an imposed trajectory of the hand. Both of the two phases refer to experimental data from the literature to compare results, and highlight the model's limits.

3.6.1 *Maximum joint moments*

Each joint motion is actuated by a small group of muscles acting together in one direction, and a complementary group of *antagonist* muscles that act to generate a moment in the opposite direction. Activating only the first group while the joint motion is prescribed and at a very

slow rate, gives a good approximation of the moment that the muscles can generate with respect to the joint motion in isometric conditions, since the velocity of contraction or lengthening of the fibers is negligible. Moreover, the joint couple, estimated as reaction moment applied to the corresponding joint, in absence of a gravity field and with a sufficiently small angular velocity, depend almost exclusively on the muscular force.

The results in this phase are compared with experimental and numerical data from literature, and refer mostly to the work published by Holzbaur et Al. in 2005 [21], which reports data from a vast literature to perform an analogous validation.

Investigated joint motions are

1. shoulder abduction
2. shoulder flexion
3. elbow flexion
4. forearm prono-supination
5. wrist flexion
6. wrist deviation

For each motion, the associated rotation of the joint has been imposed, with a small angular velocity, $\omega = 0.12217$ rad/s, corresponding to 7 deg/s.

3.6.1.1 *Shoulder abduction - adduction moment*

The first joint moment estimated is the one associated with the abduction of the shoulder. The arm is set in a rest position, alongside the body, and thus the humerus is extended with a positive rotation of 90° about its local y-axis, referring to Figure 13. The prescribed rotation is a 90° adbuction of the shoulder, i.e. a negative rotation of 90° of the humerus about the global x-axis.

The abduction moment is the reaction moment in the shoulder joint, about the global x-axis.

The active muscles for the abduction and the adduction of the shoulder are showed in Table 8. The maximum moment estimated, 71 Nm,

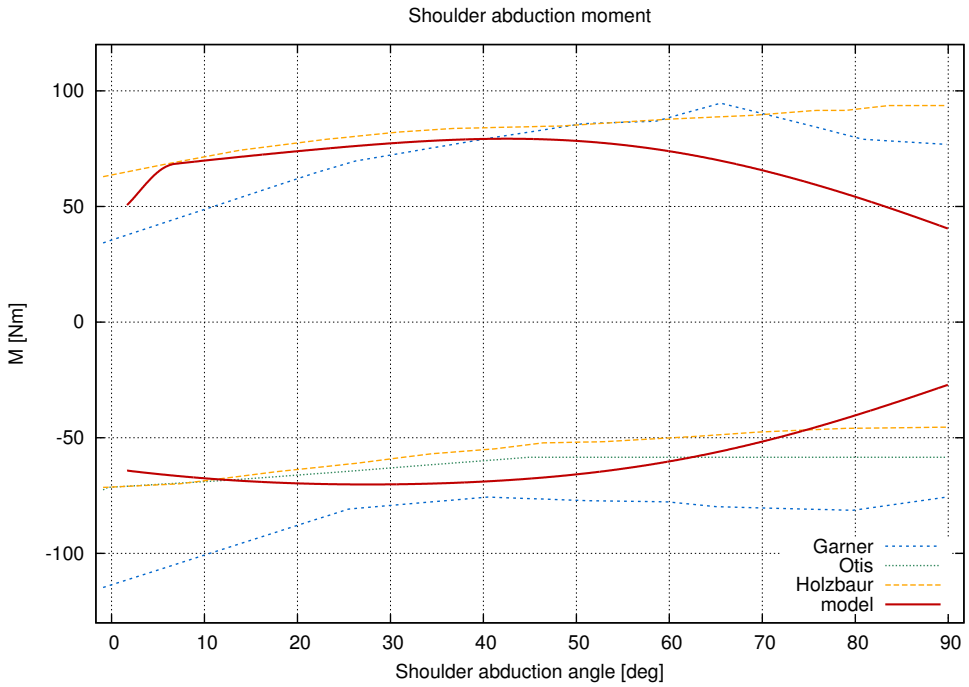

Figure 28: Shoulder abduction isometric moment estimated by the model, in comparison to data published Holzbaur [21], Garner and Pandy [13] and Otis [41]. The abduction angle is reported here considering the arm rest position alongside the body corresponding to 0°, and the full flexion position to an angle of 90°.

compares favorably with the results published by Garner and Pandy [13], Otis et al. [41] and Holzbaur et al. [21], and so does the maximum adduction moment of 82 Nm. The model also correctly reproduce the increase of abduction and adduction moment with abduction angle, up to an angle of abduction of approximately 70°.

The accuracy of the model is lower for higher abduction angles, but this is expected since the movements of scapula and clavicle are neglected, and thus the moment arms of the muscles involved in this kind of motion decrease with a higher rate than in reality when the arm is abducted significantly.
This aspect is though of relative importance for the context in which the model has been utilized: during vehicle control, the arm is generally lowly abducted.

Table 8: Muscle bundles in the model, that act on abduction and adduction of the shoulder.

Muscles that act to adduce the humerus
Deltoid, middle fibers
Infraspinatus
Supraspinatus
Muscles that act to adduce the humerus
Deltoid, anterior fibers
Pectoralis Major
Latissimus dorsi

3.6.1.2 *Shoulder Flexion*

In this case, starting from the same rest position of the previous simulation, the arm is flexed to bring the humerus parallel to the ground, with the palm facing forward, in anterior direction. A 0° flexion angle means that the arm is in vertical position, and thus a 90° flexion means that the arm is pointing anteriorly.

Muscles involved with the flexion of the shoulder are reported in Table 9.

The flexion and extension moments are reproduced with good accuracy, as compared to results published by previously mentioned authors, and by Winters [52]. The peak flexion moment, 107 Nm, is higher that the ones found in the literature in the range 30-50° flexion, but it is also to be noted that the variability of the experimental results is quite important. Conversely, the extension moment is only 1.4 Nm underestimated at 50° if compared with results ftom Garner [13], and the shape of the curve is correctly reproduced throughout the articular range here considered.

Again, it can be noted that the model loses accuracy for high flexion angles, but this is expected for the same reasons explained in the previous section, and can be accepted since the range of flexion angles 70-90° is very rarely used in vehicle control.

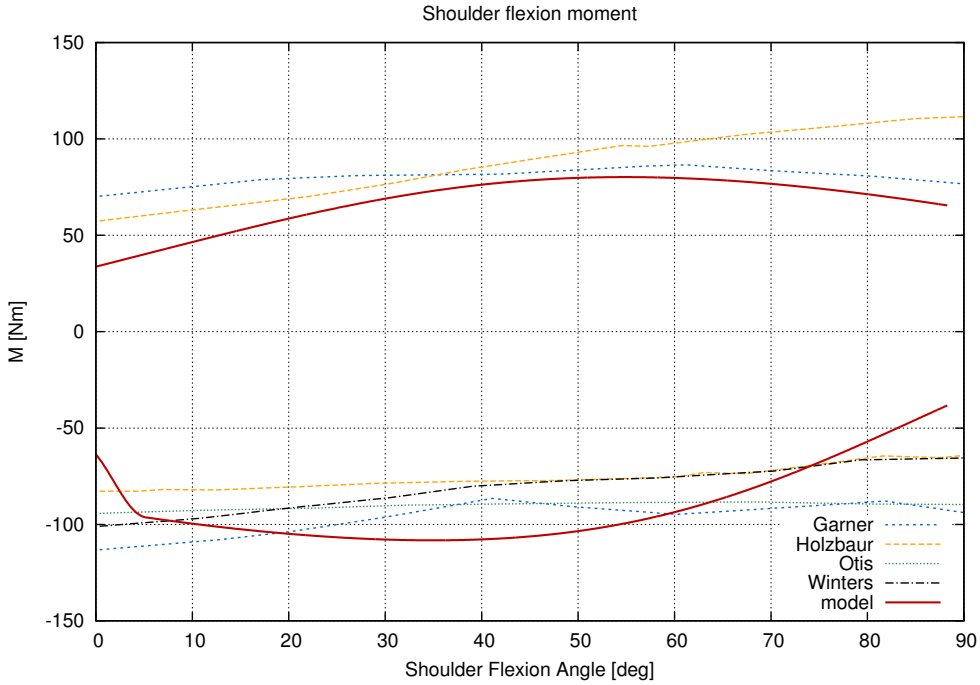

Figure 29: Shoulder flexion isometric moment estimated by the model, in comparison to data published Holzbaur [21], Garner and Pandy [13] and Otis [41] and Winters [52]. The flexion angle is reported here considering the arm rest position alongside the body corresponding to 0°, and the full flexion position to an angle of 90°.

Table 9: Muscle bundles in the model, that act on the flexion and the extension of the shoulder.

Muscles that act to flex the humerus
Deltoid, anterior and middle fascicles
Pectoralis Major
Muscles that act to extend the humerus
Deltoid, posterior fibers
Latissimus dorsi

3.6.1.3 *Elbow Flexion*

In this simulation, the the upper arm is held close to its rest position alongside the body, at an angle of 10° flexion, and the forearm is flexed

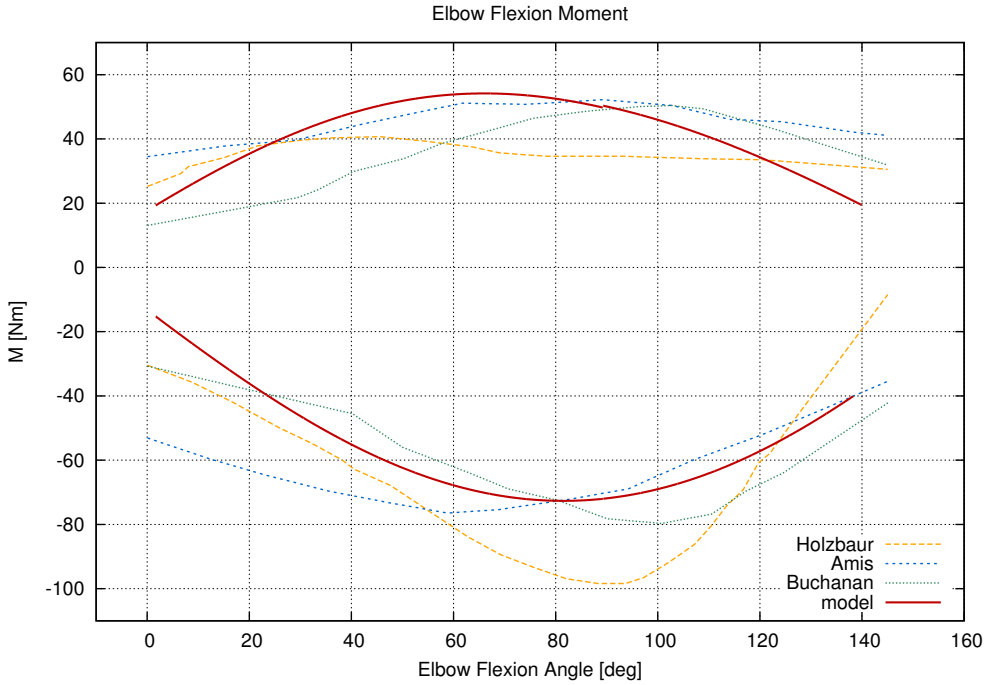

Figure 30: Elbow flexion isometric moment estimated by the model, in comparison to data published Holzbaur [21], Amis [2] and Buchanan [4]. The flexion angle is reported here considering the 0° angle corresponding to the forearm completely extended, while the maximum flexion occurs for an angle of 140°.

from the fully extended position to a relative angle between the ulna and the humerus of -140°, about the humerus y-axis of Figure 13.

The elbow flexors are more vigorous that the elbow extensors, and the model correctly capture this characteristic, as can be seen in Figure 30. The maximum flexion moment is 73 Nm, while published results range from 75 to 80 [2, 4]. The extension moment is within the range of the published data, and matches the trend observed experimentally.

3.6.1.4 *Forearm Pronation*

The arm starts in this case from the fully flexed position, with the humerus oriented horizontally and pointing anteriorly, the elbow fully extended and the palm of the hand facing upward. The hand is then rotated about its x-axis, pronating the forearm to reach a pronation angle of slightly less than 20°.

Table 10: Muscle bundles in the model, that act on the flexion and the extension of the forearm.

Muscles that act to flex the forearm
Brachialis
Brachioradialis
Biceps (both heads)
Pronator Teres
Muscles that act to extend the forearm
Triceps, all the heads

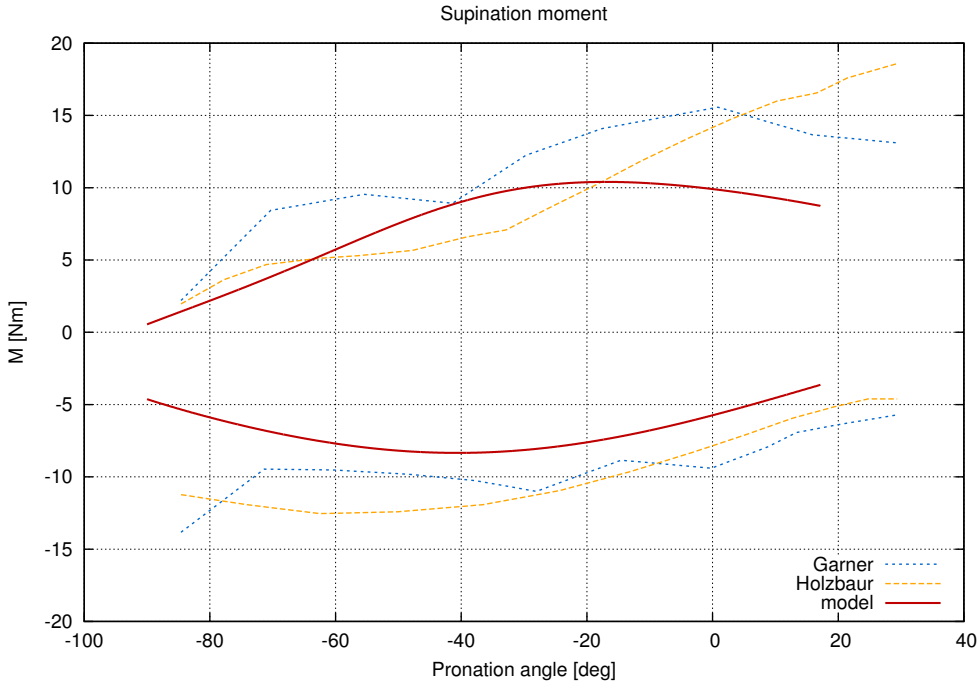

Figure 31: Forearm supination isometric moment estimated by the model, in comparison to data published Holzbaur [21] and Garner [13]. The pronation angle is reported here considering the -90° angle corresponding to the forearm completely supinated, while positive angles correspond to a pronated forearm.

During prono-supination, the major actors are three muscles especially devoted to this kind of joint motion: the *pronator teres*, the *pronator*

quadratus and the *supinator brevis*. The other bundles interested are shown in Table 11

Compared with experimental data, pronation and supination moment seems to be slightly underestimated by the model. Particularly the supination moment is below the range of experimental data. The limitation is thought to be non-restrictive of the capabilities of the model, though, for the reason that prono-supination moment is generally very small in the applications considered.

Table 11: Muscle bundles in the model, that act on the pronation and the supination of the forearm.

Muscles that act on foream pronation
Brachioradialis
Pronator Quadratus
Pronator Teres
Muscles that act on forearm supination
Supinator Brevis
Biceps

3.6.1.5 *Wrist Flexion*

In order to estimate moments related to wrist flexion and extension, the arm is set up with the humerus parallel to the ground an pointing forward. The hand starts from a flexion angle of -50° and reaches an extension angle of 50°.

Seven muscle bundles act on this kind of motion, almost all connecting the humerus to the hand. They are summed in table 12.

Experimental data from Delp et al. [9] and numerical data from the biomechanical model developed from Holzbaur et at. [21] is compared to the model results in Figure 32. Both trend and absolute values are reproduced with good accordance, even though the model seem to slightly underestimate the extension moment, with respect to experimental values.

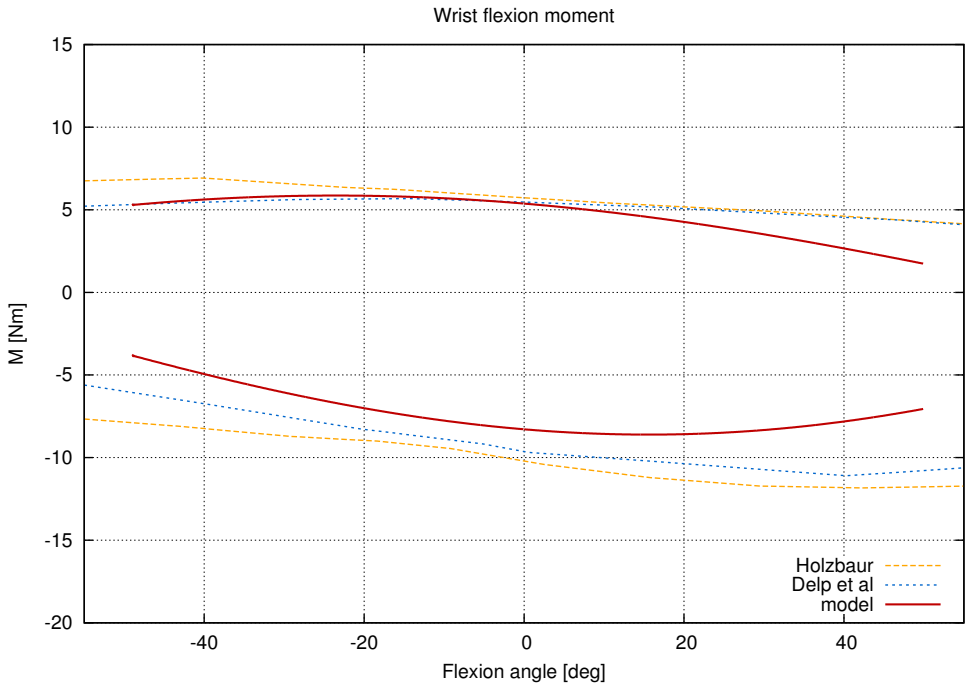

Figure 32: Wrist flexion isometric moment estimated by the model, in comparison to data published Holzbaur [21] and Delp [9]. Negative angles corresponds to the wrist completely flexed, while positive angles correspond to a wrist extension.

Table 12: Muscle bundles in the model, that act on the flexion and the extension of the wrist.

Muscles that act on wrist flexion
Flexor Carpi Radialis
Flexor Carpi Ulnaris
Flexor Digitorum
Abductor Pollicis Longus
Muscles that act on wrist extension
Extensor Carpi Radialis
Extensor Carpi Ulnaris
Extensor Digitorum

3.6.1.6 *Wrist Deviation*

Wrist ulnar and radial deviation are rotations about the hand z-axis that bring the hand toward the medial plane (ulnar deviation) or away from

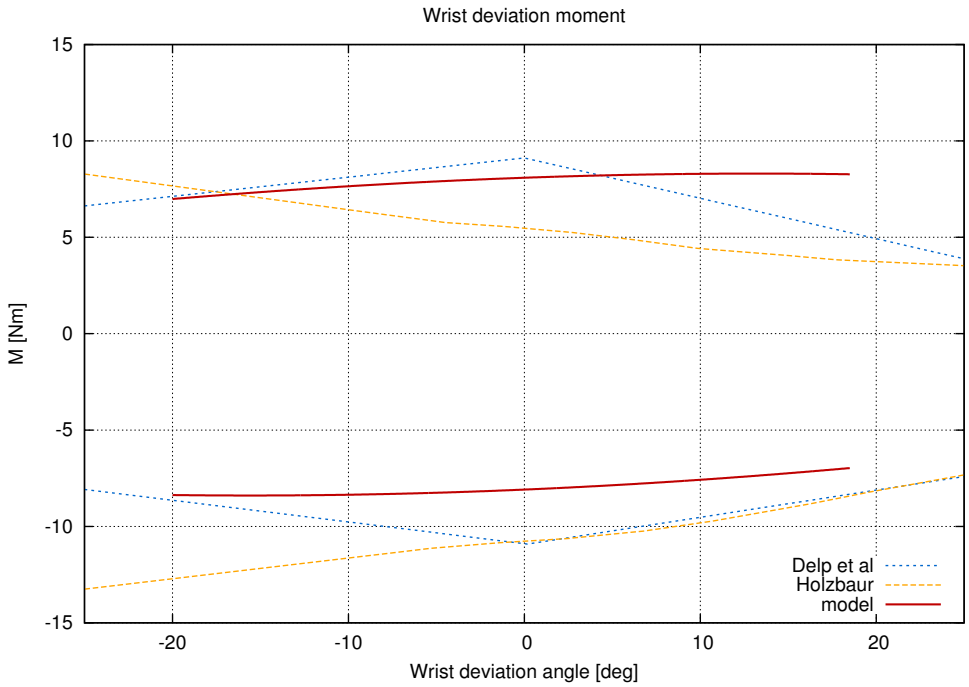

Figure 33: Wrist deviation isometric moment estimated by the model, in comparison to data published Holzbaur [21] and Delp [9]. A -90° angle corresponds to the wrist completely flexed, while positive angles correspond to a wrist extension.

it (radial deviation). The hand in this simulation performs a -20° - +20° rotation about its z-axis.

The same muscles that perform the flexion and extension of the wrist are responsible for its deviation, as showed in Table 13.

The absolute value of ulnar and radial deviation moments estimated compare favorably to experimental data from Delp et al [9] with regard to ulnar deviation (positive curve of Figure 33, while it appears to be slightly underestimated for radial deviation.

In all the interested results in the validation, it has to be taken into account the great variability of human musculoskeletal parameters involved, and the simplifications made with regard to upper limb geometry and constraints. Moreover, many of the moment trends could be better approximated by subdividing large muscle bundles (e.g. the pectoralis major muscle) into multiple elastic elements in parallel, with different attach points and lengths.

Given the scope of this work, this was judged to be as an unnecessary complication of the model, since very accurate reproduction of muscular forces is not sought here.

Table 13: Muscle bundles in the model, that act on the deviation the wrist.

Muscles that act on wrist ulnar deviation
Flexor Carpi Ulnaris
Extensor Carpi Ulnaris
Extensor Digitorum
Flexor Digitorum
Muscles that act on radial deviation
Extensor Carpi Radialis
Flexor Carpi Radialis
Abductor Pollicis Longus

3.6.2 *Muscular activation*

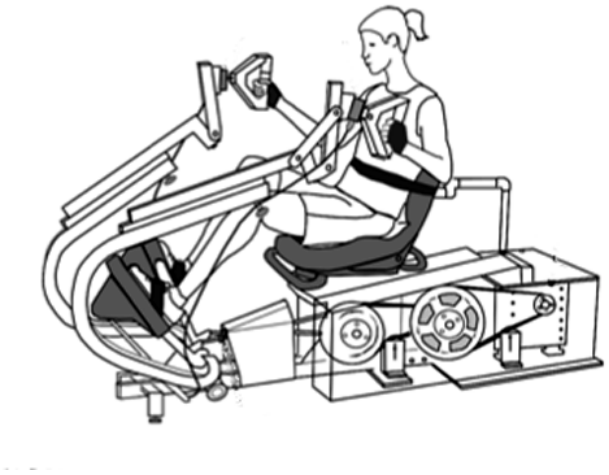

Figure 34: The experimental setup used by Huang et al to measure EMG activity of upper limb muscles during physical exercise. Source: [23]

To examine the model's capability to correctly reproduce the activation patterns of muscles in a given task, a comparison with experimental

surface electromyography (EMG) data collected from Huang et al. is presented [23]. The experimental setup used by these authors is a stepper machine, modified to induce a prescribed hand motion.

A moment proportional to the error between the prescribed motion and the actual one is introduced in the handlebars, so that the subject is restrained from deviating in an important way from the desired trajectory.

EMG signals are collected from four muscle bundles in the upper limb: the deltoid anterior fascicles, deltoid posterior fascicles, biceps and triceps. Sixteen subjects in the age range 18-29 years were involved in the study, and data from the electromyographs was extracted to represent the single stepping cycle, filtered and averaged.

A similar setup was simulated with the multibody model. In the absence of precise geometrical data for the setup used by Huang, a compatible geometry was used.
The hand grasps the handlebar grip with the palm facing the medial plane, and the initial position of the grips was set at 350 mm from the shoulder glenoid fossa, in x-direction, 100 mm in negative y-direction and in the $z = 0$ plane. The handlebars are schematized as 1200 mm bars, hinged to rotate only about an axis parallel to the global y-axis and passing through a point 1200 mm in negative z-direction from the handlebar manipulator position.

The motion is imposed to the handlebars, that perform a sinusoidal rotation about the hinge axis, with amplitude of 8° in both directions, and frequency of 1.25 Hz. This translates into a range of motion of approximately $\pm 170mm$ in the global x direction. In Figure 35 the results found by Huang et al. are shown in comparison to estimated activation coefficients. In the first part of the cycle, i.e. with the hand pulling toward the body, the Deltoid Anterior and the Triceps activate to flex the shoulder and the elbow, while in the second part, as the hand pushes the handle forward, the Biceps and the Deltoid Posterior activate to perform the opposite joint rotations.

The model captures the general tendencies in the activation patterns. The correct muscle groups activate, and activate in the right sequence. Activation patterns of the Deltoid Anterior and of the Biceps are caught with good accuracy, while the patterns relative to the Triceps Brachii and the Deltoid Posterior differ in shape from the ones found by Huang. This behavior may be caused from the cost function used to compute muscle forces: the minimization of the total activation is generally

regarded as hold better validity in conditions in which the dynamics of muscle activation does not play an important role, i.e. in static or quasi-static situations [46].

Other plausible causes for the discrepancy include: geometry of the model, anthropometrical and biomechanical parameters of the subjects, coupled contraction dynamics between muscles of the upper and the lower limb.

Taking all of the limitations of this comparison into consideration, and noting that a comparison between the absolute values of the activation coefficients and the experimental EMG data is not possible in absence of EMG measurement of the activity related to maximum isometric force production of the muscles, is it possible to note that the model capturesthe general shape of the activation patterns in an acceptable manner, especially, especially considering its purpose.

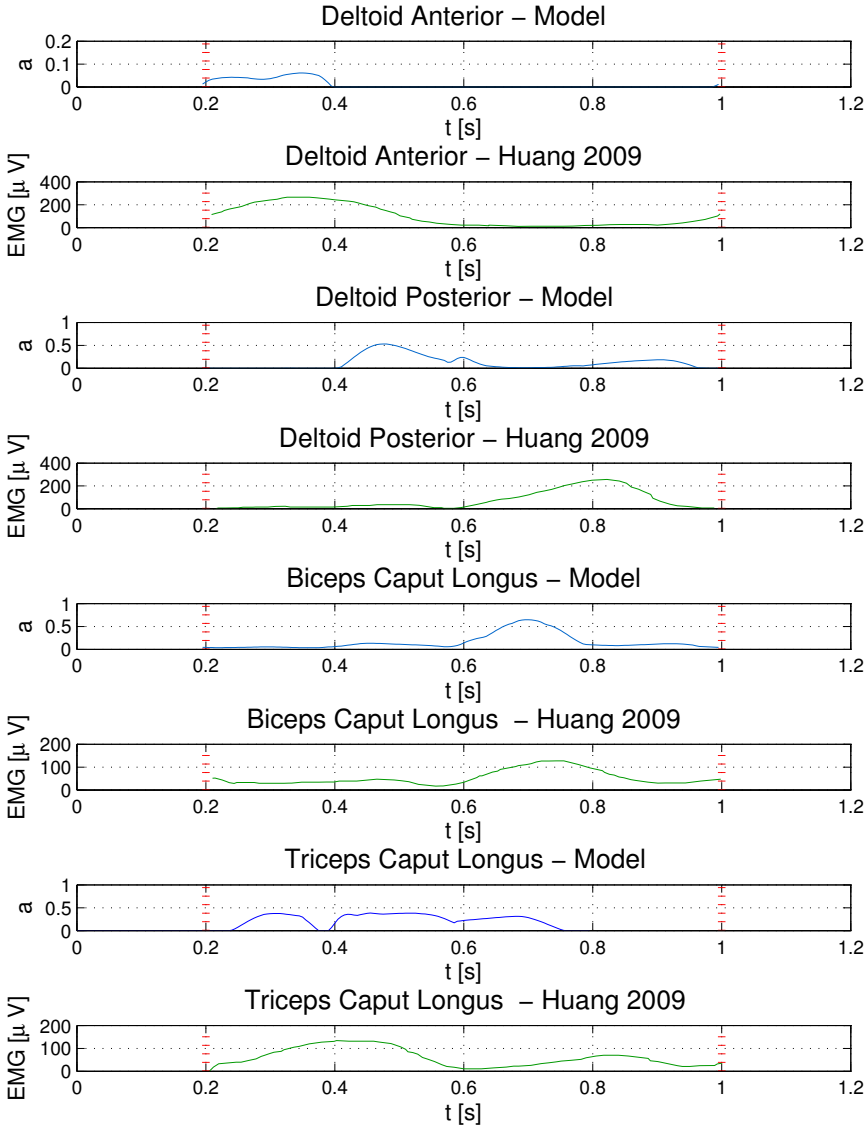

Figure 35: EMG activity of the four muscle bundles measured by Huang et al. [23] compared with activation coefficients estimated by the model. The level of accuracy is not even between the muscles, but the general tendencies are captured. Without indications on EMG activity corresponding to maximum isometric force, it is not possible to confront the absolute values of the quantities.

4

UPPER LIMB IMPEDANCE

4.1 METHODOLOGY

The final goal of the simulation is to find the equivalent mechanical impedance of the upper limb in the dynamical conditions. It would be possible to set up a numerical experiment, applying a random force/torque disturbance to the arm in the desired control position and perform an equivalent stiffness and damping identification on the estimated transfer functions.

A more analytical approach was followed in this work, to eliminate the problems related to the purely numerical approach mentioned above.

When equilibrium conditions are reached,

$$[\phi_{/q}]^T\lambda + [\psi_{/q}]^T\mu = [B]f_m(q, \dot{q}, a) \tag{4.1a}$$

$$\psi(q) = \alpha(t) \tag{4.1b}$$

$$\phi(q) = 0 \tag{4.1c}$$

with μ the generalized forces that the hand applies to the manipulator and $\psi(q)$ the vector of nonlinear relationships between the generalized coordinates and the imposed motion. Linearization of the single muscular force brings to

$$\delta f_m(q, \dot{q}, a) = \frac{\partial f}{\partial x} \cdot \frac{1}{l_0}\frac{\partial l}{\partial q}\delta q + \frac{\partial f}{\partial v} \cdot \frac{1}{v_0}\left(\frac{\partial \dot{l}}{\partial q}\delta q + \frac{\partial \dot{l}}{\partial \dot{q}}\delta \dot{q}\right) \tag{4.2}$$

x and v are the dimensionless parameters defined in Section 2.3.1, while l is the unit vector defining the muscle's element axis. The equation can be rewritten, separating the terms related to δq from the ones related to $\delta \dot{q}$

$$f_m = \left(f_{/x}\frac{1}{l_0}l^T[l_{/q}] + f_{/v}\frac{1}{v_0}\dot{l}^T([I] - ll^T)[l_{/q}]\right)\delta q + \frac{1}{v_0}l^T[l_{/\dot{q}}]\delta \dot{q} \tag{4.3}$$

with $[\mathbf{l}_{/q}]$ and $[\mathbf{l}_{/\dot{q}}]$ containing the derivatives of vector $\mathbf{l}$ with respect to the generalized coordinates.

The 4.3 define the rows of two matrices $[\mathbf{f}_{\delta q}]$ and $[\mathbf{f}_{\delta \dot{q}}]$: the rows of the first are the sum of the row vectors that are multiplied by $\delta\mathbf{q}$ in the last equation, while the rows of the second are constituted by the row vectors that multiply $\delta\dot{\mathbf{q}}$.

It is now possible to perturb the 4.1, with respect to θ and μ, and to rewrite the problem in joint coordinates, to eliminate the third block of the 4.1

$$[\vartheta^{+}_{/q}]^{T}[\psi_{/q}]^{T}\delta\boldsymbol{\mu} = [\vartheta^{+}_{/q}]^{T}[B][\mathbf{f}_{\delta q}][\vartheta^{+}_{/q}]\delta\boldsymbol{\theta} \tag{4.4a}$$

$$[\psi_{/q}][\vartheta^{+}_{/q}]\delta\boldsymbol{\theta} = \delta\boldsymbol{\alpha} \tag{4.4b}$$

or,

$$\begin{bmatrix} -[\vartheta^{+}_{/q}]^{T}[B][\mathbf{f}_{\delta q}][\vartheta^{+}_{/q}] & [\vartheta^{+}_{/q}]^{T}[\psi_{/q}]^{T} \\ [\psi_{/q}][\vartheta^{+}_{/q}] & [0] \end{bmatrix} \begin{Bmatrix} \delta\boldsymbol{\theta} \\ \delta\boldsymbol{\mu} \end{Bmatrix} = \begin{Bmatrix} 0 \\ [I]\delta\boldsymbol{\alpha} \end{Bmatrix} \tag{4.5}$$

Indicating with $[T]$ the relationship between $\delta\boldsymbol{\alpha}$ and $\delta\boldsymbol{\theta}$, and with $[K]$ the sought stiffness matrix,

$$\delta\boldsymbol{\theta} = [T]\delta\boldsymbol{\alpha} \tag{4.6a}$$

$$\delta\boldsymbol{\mu} = [K]\delta\boldsymbol{\alpha} \tag{4.6b}$$

$$\tag{4.6c}$$

thus, the previous system can be rewritten as

$$\begin{bmatrix} -[\vartheta^{+}_{q}]^{T}[B][\mathbf{f}_{\delta q}][\vartheta^{+}_{/q}] & [\vartheta^{+}_{/q}]^{T}[\psi_{/q}]^{T} \\ [\psi_{/q}][\vartheta^{+}_{/q}] & [0] \end{bmatrix} \begin{bmatrix} [T] \\ [K] \end{bmatrix} \delta\boldsymbol{\alpha} = \begin{bmatrix} [0] \\ [I] \end{bmatrix} \delta\boldsymbol{\alpha} \tag{4.7}$$

being $\delta\boldsymbol{\alpha}$ arbitrary, it can be eliminated on both sides, and the system can be solved to find $[K]$, the equivalent stiffness matrix of the biomechanical system.

Perturbing the 4.1 with respect to $\dot{\theta}$ and μ with a similar procedure, another linear system can be written

$$\begin{bmatrix} -[\vartheta_q^+]^T[B][f_{\delta\dot{q}}][\vartheta_{/q}^+] & [\vartheta_{/q}^+]^T[\psi_{/q}]^T \\ [\psi_{/q}][\vartheta_{/q}^+] & [0] \end{bmatrix} \begin{bmatrix} [T] \\ [R] \end{bmatrix} \delta\dot{\boldsymbol{\alpha}} = \begin{bmatrix} [0] \\ [I] \end{bmatrix} \delta\dot{\boldsymbol{\alpha}} \tag{4.8}$$

this time, matrix [R], the equivalent damping matrix of the system, if found by solving the system. It is to be highlighted that for the above mentioned method to return the correct value of the mechanical impedance of the system, a true equilibrium condition has to be reached by the system. This is seldom the case in the situations here analyzed, but if the dynamics of the system is sufficiently slow, the impedance calculated with this method will be very close to the actual one.

In essence, is is not possible to claim that matrices [K] and [R] represent the "true" stiffness and damping matrices of the biomechanical system, but can be rather thought as a performance index. [1]

1 As a notable possible development, it can be shown that an equivalent second-order quasi-static approximation of the biomechanical system about the reference configuration could be obtained by computing its mass matrix, alongside with the stiffness and damping matrices already defined.
The mass matrix is obtainable by solving a linear system analogous to the ones used for [K] and [R], aside from the contribution of the muscular forces

$$[M]\delta\ddot{\mathbf{q}} + [\phi_{/q}]^T\delta\boldsymbol{\lambda} + [\psi_{/q}]^T\delta\boldsymbol{\mu} = \mathbf{0} \tag{4.9a}$$

$$[\phi_{/q}]\delta\ddot{\mathbf{q}} = \mathbf{0} \tag{4.9b}$$

$$[\psi_{/q}]\delta\ddot{\mathbf{q}} = \delta\ddot{\boldsymbol{\alpha}} \tag{4.9c}$$

projecting into joint space

$$[\vartheta_q^+]^T[M][\vartheta_{/q}^+]\delta\ddot{\mathbf{q}} + [\vartheta_{/q}^+]^T[\psi_{/q}]^T\delta\boldsymbol{\mu} = \mathbf{0} \tag{4.10a}$$

$$[\psi_{/q}][\vartheta_{/q}^+]\delta\ddot{\mathbf{q}} = \delta\ddot{\boldsymbol{\alpha}} \tag{4.10b}$$

The system can be solved with steps analogous to the ones shown for the stiffness and the damping matrix.

4.2 TORQUE - LESS MODES OF ACTIVATION

Since an articular motion is almost always performed by a combination of more than two synergistic and antagonistic muscles, the upper limb is essentially an over-actuated mechanism, and this redundancy can be at the root of the contemporary activation of some muscular bundles, that does not produce a variation of the total torque applied to the joint.

We will call such a combination of activations a *torque-less activation mode* (TLAM). It is interesting to evaluate the potential contribution of TLAMs to the mechanical impedance of the limb in the configurations associated with vehicle control for the reason that they are not measurable directly from the human response in the control loop, but can alter significantly the arm impedance.

By knowing the relative importance of TLAMs, an estimation of the possible range of the dangerous conditions in coupled vehicle-pilot dynamics can be evaluated, and correlation with the experimental data can be enhanced.

If the limb is in an equilibrium position, the activation patterns of the muscles associated must be such as to provide the joint's torque

$$\mathbf{c} = [\vartheta^{+}_{/\mathbf{q}}]^{T}[B(\mathbf{q})]\mathbf{f}_{m}(\mathbf{q}, \dot{\mathbf{q}}, \mathbf{a}). \tag{4.11}$$

This equilibrium condition holds any time the limb is producing a steady-state torque.

By linearizing the constitutive law of the muscles the passive contribution is separated from the active one

$$\mathbf{f} = \mathbf{f}_{0}(\mathbf{q}) + \mathbf{f}_{/a}(\mathbf{q}, \dot{\mathbf{q}})a \tag{4.12}$$

Joint couple can be divided into several contributions

$$C_{/\mathbf{q}} = [\vartheta^{+}_{/\mathbf{q}}]^{T}[B](f_{0/\mathbf{q}} + f_{a/\mathbf{q}}\mathbf{a}) \tag{4.13a}$$

$$C_{/\dot{\mathbf{q}}} = [\vartheta^{+}_{/\mathbf{q}}]^{T}[B]f_{a/\dot{\mathbf{q}}}\mathbf{a} \tag{4.13b}$$

where $f_{0/\mathbf{q}}$ is the passive contribution of muscular force. Considering now a perturbation with respect to the activation coefficients of the 4.11

$$[\vartheta^{+}_{/\mathbf{q}}]^{T}[B]\mathbf{f}_{/\mathbf{a}}\delta\mathbf{a} = [A]\delta\mathbf{a} = \delta\mathbf{c} \tag{4.14}$$

matrix $[\vartheta^{+}_{/q}]^{T}$, as noted in section 3.4 is rectangular, $m \times n$ with m being the number of generalized coordinates and n the number of joint coordinates, and has a full rank.

By applying a singular value decomposition (SVD), matrix $[A]$ is represented by the product

$$[U][\Sigma][V]^{T} = [A] \tag{4.15}$$

where matrix $[U]$ contains the left singular vectors of $[A]$, and matrix $[V]$ the right singular vectors, while $[\Sigma]$ is a rectangular matrix, with the singular values of $[A]$ on the diagonal. Since $[A]$ is a 7×25 matrix, the null-space of $[A]$ is defined by the 18 columns of $[V]$ that do not have a corresponding singular value thus defines a linear combination of activation coefficients that does not produce a torque variation, and it is therefore a TLAM. Since matrix $[A]$ can be written as

$$[A] = [U][\Sigma][V] = [U]\begin{bmatrix} [\Sigma] & [0] \end{bmatrix} \begin{bmatrix} [V_1]^{T} \\ [V_2]^{T} \end{bmatrix} \tag{4.16}$$

matrix $[V_2]$ contains the TLAMs.

If the total activation is now separated into a minimal contribution aside to possible the contribution of all the TLAMs,

$$\mathbf{a} = \mathbf{a}_{min} + \sum \boldsymbol{\nu}_{i0}\mathbf{a}_{TLAM} \tag{4.17}$$

now the 4.13b can be expressed as

$$C_{/q} = [A]\left[f_{0/q} + f_{a/q}\left(\mathbf{a}_{min} + \sum \boldsymbol{\nu}_{i0}\mathbf{a}_{TLAM}\right)\right] \tag{4.18a}$$

$$C_{/\dot{q}} = [A]\left[f_{a/\dot{q}}\left(\mathbf{a}_{min} + \sum \boldsymbol{\nu}_{i0}\mathbf{a}_{TLAM}\right)\right] \tag{4.18b}$$

separating the contribution associated with minimum activation and the one coming from TLAMs.

4.3 ROTORCRAFT PILOT'S ARM IMPEDANCE IDENTIFICATION

4.3.1 *PAO testing at University of Liverpool*

Data collected by the research group on rotorcraft aeroservoelasticity, Department of Aerospace Engineering, Politecnico di Milano in July 2011 with the help of a 2 Degrees of Freedom aeroelastic rotorcraft model specifically implemented in the Bibby Flight Simulation Laboratory at The University of Liverpool, Flight Science and Technology (FST) Research Group, in the framework of the ARISTOTEL project [33] were used to feed realistic data into the model kinematics.

The tests considered were aimed at the evaluation of PAO (Pilot Induced Oscillations - See 1.2) in rotorcraft-pilot coupling phenomena. The two degrees of freedom are: the vertical displacement of the rotorcraft, subjected to aerodynamic damping, and the vertical displacement of the pilot's seat.

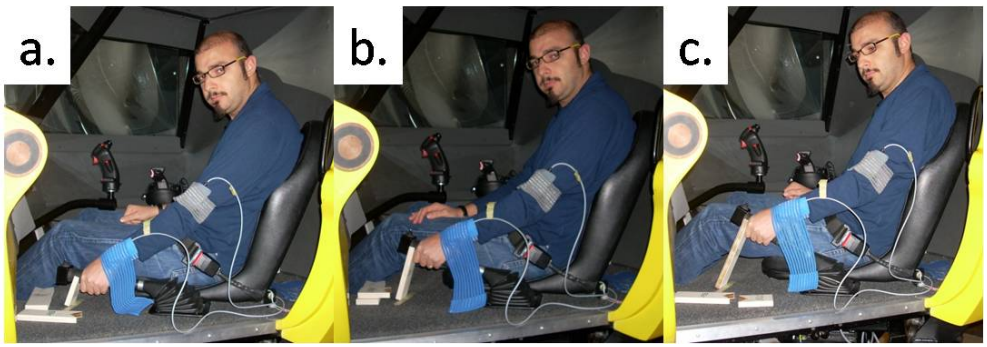

Figure 36: Picture of the rotorcraft simulator of the Bibby Flight Simulation Laboratory, University of Liverpool (UK). The pilot is showing the 0%, 50% and 90% collective control positions, in a., b. and c., respectively. Source: [32]

The pilot was asked to repeatedly change the altitude of the aircraft, using a visual target, while the aircraft is subjected to a disturbance force in the vertical direction. The rotorcraft is initially in steady state conditions at a constant altitude, with the collective handle at 50% of its range of motion, which is about 35 degrees. The initial position of the handle has been used as the reference position, and the variation, in percent, of the inceptor's angular position is acquired.

In the tests performed at University of Liverpool, the transfer function of the pilot was experimentally identified and used in conjunction with a simplified aircraft numerical model to compute the parameters that may introduce instability.

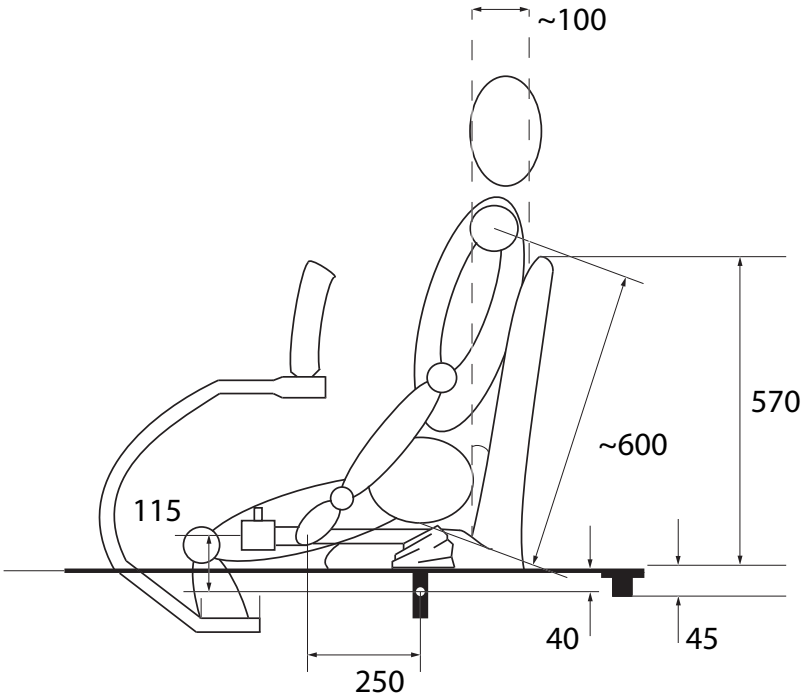

Figure 37: Cockpit geometry in the multibody model.

The geometrical configuration of the simulator cockpit was reproduced in the multibody model, and some assumptions had to be made. Since the pilot acts on the collective inceptor with his left arm, a specular configuration to the one represented in Figure 13 has to be considered. The x-axis of the single bone is still coincident with the bone's mechanical axis, and the z-axis still points upward, but the y-axis in this case points away from the medial plane. The pilot is considered as having the back rested on the seat, and in this position the sagittal axis is assumed to form a 10 degrees angle with the global z-axis. The length of the collective handle is 275 mm, and its horizontal projection is 250 mm.

Anthropometric data and regression analyses from [7, 8] were used to model a 170 cm, 70 kg pilot, whose parameters are collected in Table 14.

Element	Properties				
	Mass [kg]	Height [cm]			
Body	70	170			
	Length [mm]	Mass [kg]	$J_{xx}[kgmm^2]$	$J_{yy}[kgmm^2]$	$J_{zz}[kgmm^2]$
Humerus	297	2.02	2555.2	14411.2	16228.9
Radius	261	0.61	388.2	2662	2717
Ulna	261	0.59	582.2	3994	4076
Hand	68	0.43	195.4	724	724

Table 14: Pilot parameters used in the simulations.

The hand of the pilot grasps firmly the collective control's inceptor, so no degrees of freedom were allowed between the hand and the handle's nodes. This is probably an oversimplification, as a relatively stiff elastic element could be inserted to represent the deformable characteristics of the hand-handle connection, but in absence of experimental data the choice was to simplify this aspect as well.

The motion of the airframe was disregarded, as the focus here is on the model's abilities to reproduce the upper limb's impedance characteristics, and so all the external perturbations were kept to a minimum.

Time histories of collective control inceptor's angular position has been imposed as the prescribed motion of a driving node in the multibody model. The one that will be presented here is shown in Figure 38.

The data was low-pass filtered with a Butterworth filter of order 2 and cutoff frequency of 5 Hz and resampled to a time step of 10^{-4}s. Since also velocity and acceleration of the handle must be imposed, numerical derivatives of the angular displacement were used. Each derivative is filtered with the same low-pass filter, to eliminate higher frequency contributionss that can lead to numerical instabilities. The time history, as noted above, represents the collective handle's position with respect to the 50 % position, or 17.5 degrees position with respect to the horizontal.

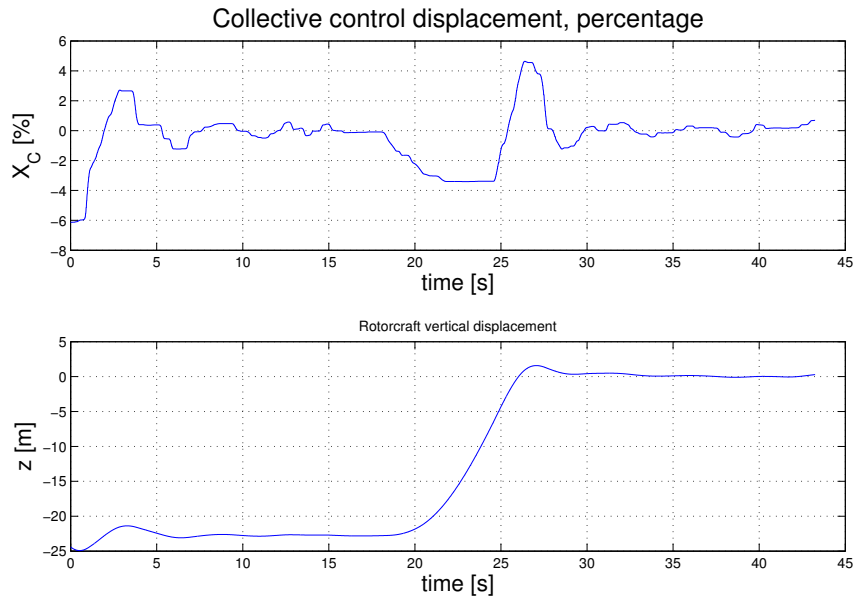

Figure 38: Collective control inceptor's angular position time history used for the prescribed motion of the handle in the multibody model (above), and vertical displacement of the rotorcraft (below). The z-axis is assumed positive in the upward direction.

The kinematics of the upper limb is determined time-marching using the method of Section 3.2.1, i.e. by constraining an equivalent static system with several "dummy" springs, that impose configuration-dependent penalty coefficients to the relative positions of the rigid bodies, accounting for both the joint articular limits and comfort level. In the resulting discomfort penalty coefficient applied, that in this case is equivalent to the total elastic potential energy stored in the springs, the effect of articular joints angular positions and of muscular passive forces is summed.

The model in its initial position is depicted in Figure 39. The upper arm rests almost alongside the body, and the forearm is slightly flexed, as this position corresponds approximately to the 50 % position of the collective control inceptor. Though the hand is not visible in the figure, its position can be guessed by referring to Figure 36. Using the reference systems mentioned above, it can be noted that the hand's y-axis is aligned with the collective handle's axis, and its z-axis points toward the medial plane.

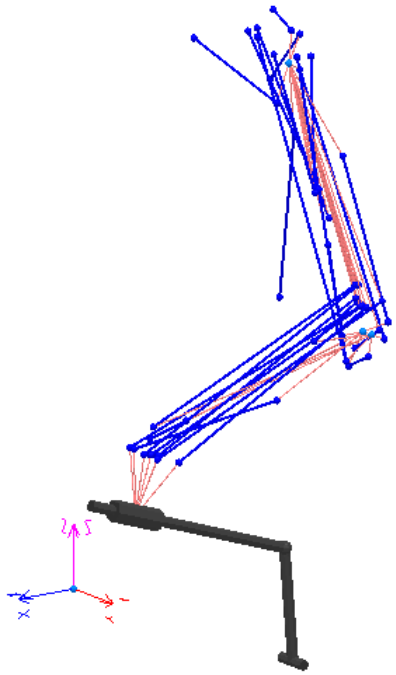

Figure 39: Model in its initial position. Thick lines correspond to elements representing the muscles, while thin lines represent their offests with respecto to the nodes.

Referring to the time history of Figure 38, it can be noted that the angular displacement of the handle is quite small compared to its range of motion: it is comprised approximately from -6 % to 5%, corresponding to -2.1 deg to +2 deg.

The only external force field acting on the limb, in the multibody simulation, is the gravity field, so a predominant part of the joint torques is devoted to the compensation of the gravity forces acting on the limb. In the real case, the accelerations of the simulator's airframe act on the body of the pilot as intertial forces, but were disregarded in this phase to be able to isolate the effects related of the limb action on the collective inceptor.

Muscular activation is, therefore, also expected to be largely dominated by the contribution needed to compensate gravity, and the impedance of the arm in this test is expected to vary in a limited way during the maneuver, making this simulation an adequate testing bed for the potential of the model.

4.3.2 *Activation coefficients*

Running the inverse dynamics simulation yields the joint torques shown in Figure 40: as expected, an essentially constant contribution is present, while the motion of the limb causes small variation of the torques about the steady state configuration.

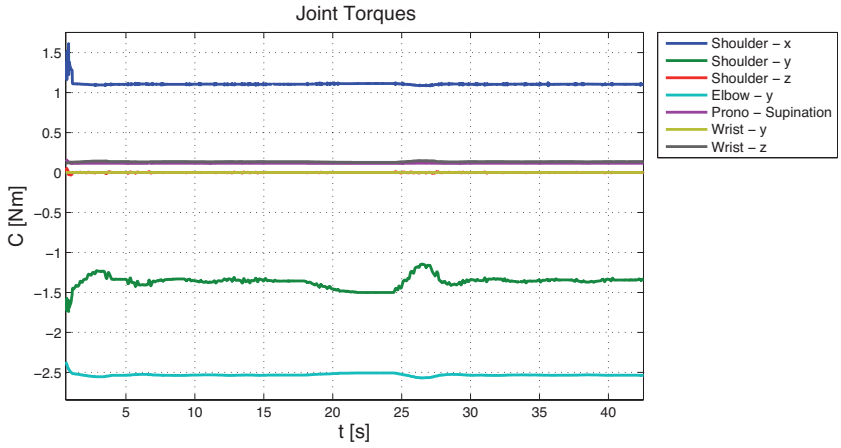

Figure 40: Joint torques of the pilot's upper limb, obtained by dynamics inversion of the multibody model, fed with the time history of the collective control's inceptor.

Using the method presented in Section 3.4, the activation parameters of the muscular bundles in the upper limb is computed, and the results are shown in Figure 41 and Figure 42. The more active shoulder muscles are the Coracobrachialis, the Deltoid Anterior, the Pectoralis Major, the Infraspinatus and the Latissimus Dorsi. and the Infraspinatus: their action is needed to counteract gravity, that tends to rotate the arm in positive y-direction, i.e. to flex the shoulder. Since the action of the first three also causes an internal rotation of the arm, the latter three provide stabilization.

In the forearm, the most active muscles are the Brachialis, the Brachioradialis, the Flexor Carpi Radialis and the Flexor Carpi Ulnaris. The first three are elbow flexors, and thus activate to keep the forearm in the correct position, against gravity. Again, correct activation patterns are found: for example, shortly after 25 s an increase in elbow flexion torque (Elbow - y torque in Figure 40 is requested, and the Brachialis, Brachioradialis and Biceps all concour to provide it. The activation of

the latter two provides stabilization to the wrist in the flexed position required to grasp the collective handle.

4.3.3 *Musculoskeletal system impedance*

The method outlined in Section 4.1 has been applied to identify the mechanical impedance of the pilot's upper limb throughout the simulated maneuver.

An important clarification has to be made here: the method is capable of identifing only the impedance that derives from the *intrinsic* properties of the muscles, and not from the muscular activation caused by reflexive system response [44]. The impedance of the active musculoskeletal system depends on the voluntary activation of the muscles both from a non reflexive standpoint, i.e. the contribution that does not depend on the voluntary action of the subject to maintain the reference configuration about which the system is linearized. To be able to account also for this second contribution of the impedance, the multibody model would have to include a feedback control system, capable of activating the muscles required to perform the reference task.

Such a control system is not implemented yet, but an attempt to evaluate, at least partially, the contribution of such component will be made through the consideration of TLAMs in the next section.

The intrinsic impedance contribution related to the collective handle rotation, when minimum activation conditions are considered, is depicted in Figure 43.

It has been calculated *freezing* the system motion every 5 s, starting from the instant of time $t = 2.5$ s.

As expected, the intrinsic impedance of the limb is small, and presents limited variation during the task. It also shows a dependence from the activation of the muscles, and this dependence is nonlinear. As an evidence, the equivalent stiffness and damping decrease around $t = 27.5$ s, when the activation of several muscles in the arm and forearm is decreasing, and the pilot is performing a maneuver. This effect is due to the strongly non-linear constitutive law of the muscles, and to the fact that they act in non symmetric way on the single joint, i.e. there are always more than two muscles acting on the joint, have

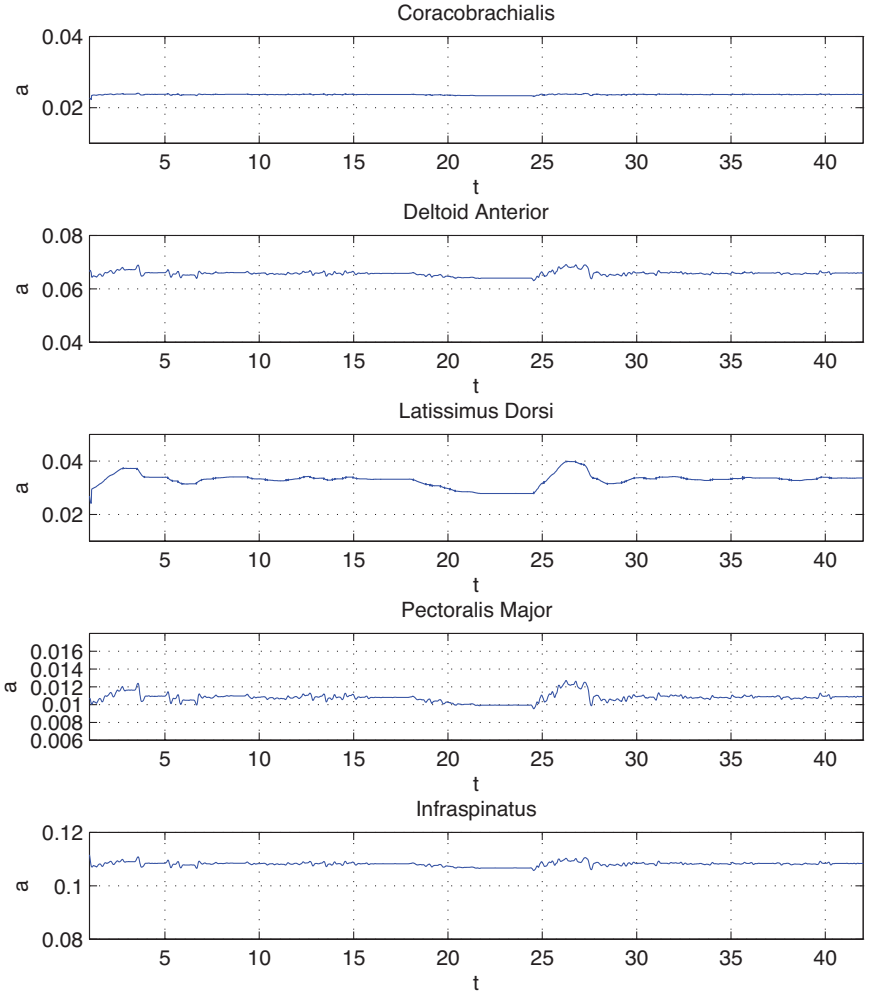

Figure 41: Activation parameters of the muscles of shoulder during the maneuver. Only the most active muscles are shown. It can be noted that the correct bundles are active, and that to a modification of the joint torque corresponds a modification of the activation patterns of the muscles acting on the joint itself.

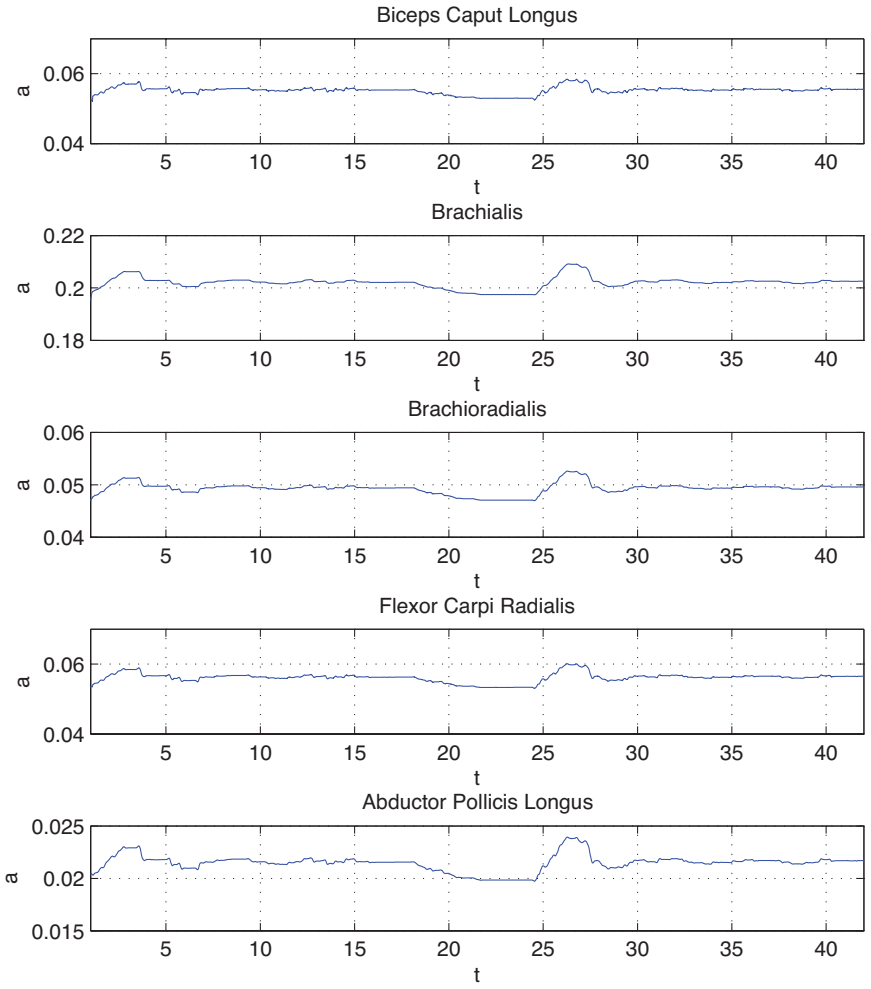

Figure 42: Activation parameters of the muscles of the forearm during the maneuver.

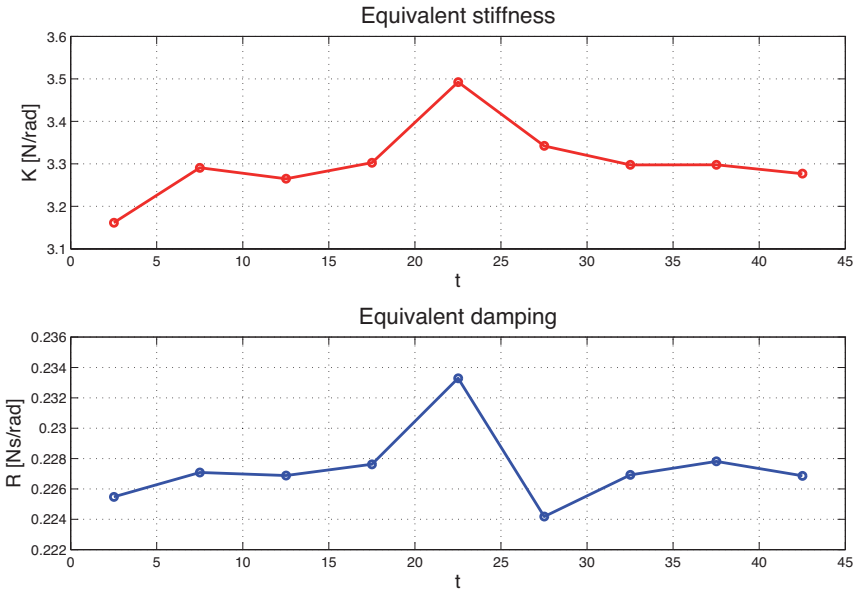

Figure 43: Intrinsic impedance of the upper limb, calculated every 5 s starting from $t = 2.5$ s

different force-production characteristics and different moment arms with respect to the joint.

Thus, some muscle bundles can be activated more and generate less equivalent stiffness with respect to certain degrees of freedom of the hand.

Considering the generic body's generalized coordinates vector to be
Considering the generic body generalize coordinates vector to be

$$q = \begin{Bmatrix} x & y & z & \theta_x & \theta_y & \theta_z \end{Bmatrix} \tag{4.19}$$

the complete stiffness and damping matrices for $t = 22.5$s are,

$$[K_{eq}] = \begin{bmatrix} 26.62 & 9.67 & -15.97 & -1.17 & 8.94 & 1.38 \\ 9.67 & 24.91 & -9.77 & -4.90 & 3.82 & 4.05 \\ -15.96 & -9.77 & 21.40 & 1.54 & -7.61 & -1.51 \\ -1.16 & -4.91 & 1.54 & 1.29 & -0.62 & -0.95 \\ 8.94 & 3.83 & -7.61 & -0.62 & 3.49 & 0.61 \\ 1.38 & 4.05 & -1.51 & -0.95 & 0.61 & 0.75 \end{bmatrix}$$

$$[R_{eq}] = \begin{bmatrix} 2.9446 & 1.5491 & -1.0319 & -0.0223 & 0.7632 & 0.1074 \\ 1.5491 & 2.7134 & -0.2382 & -0.2747 & 0.2863 & 0.3068 \\ -1.0319 & -0.2382 & 1.4555 & -0.1100 & -0.4497 & 0.0352 \\ -0.0223 & -0.2747 & -0.1100 & 0.0593 & 0.0152 & -0.0470 \\ 0.7632 & 0.2863 & -0.4497 & 0.0152 & 0.2333 & 0.0114 \\ 0.1074 & 0.3068 & 0.0352 & -0.0470 & 0.0114 & 0.0453 \end{bmatrix}$$

The only relevant terms for the present case, since the only allowed degree of freedom of the hand is the one related to the collective control, are $k(5,5)$ and $r(5,5)$, since the rotation of the handle is about the global y-axis.

The singular values of the matrices assure that they are definite positive

$$\sigma_k = \begin{Bmatrix} 80.65 & 29.52 & 10.91 & 0.63 & 0.04 & 0.01 \end{Bmatrix} \tag{4.20}$$

$$\sigma_r = \begin{Bmatrix} 20.20 & 10.06 & 4.69 & 0.20 & 0.01 & 0.01 \end{Bmatrix} \tag{4.21}$$

4.3.4 *Effect of Torque Less Activation Modes*

With the singular value decomposition presented in Section 4.2, it is possible to isolate the linear combinations of activation coefficients that do not produce a variation in joint torque, but can significantly alter the equivalent stiffness and damping properties of the limb. An example of the contribution of Torque Less Activation Modes in real life, the different psychological conditions in which a pilot has to operate can be considered: if relaxed, he will grasp the controls gently, and thus the related impedance is probably relatively small. By contrast, if for some reason his nervous tension rises, he will probably tighten the grip on the commands, causing the impedance to raise. The position of the commands does not change, and so the total joint torque does not change, but the equivalent stiffness and damping properties do change.

In Figure 44 three TLAMs for the upper limb, extracted at $t = 27.5$ s are shown. Each component has been scaled such that the maximum

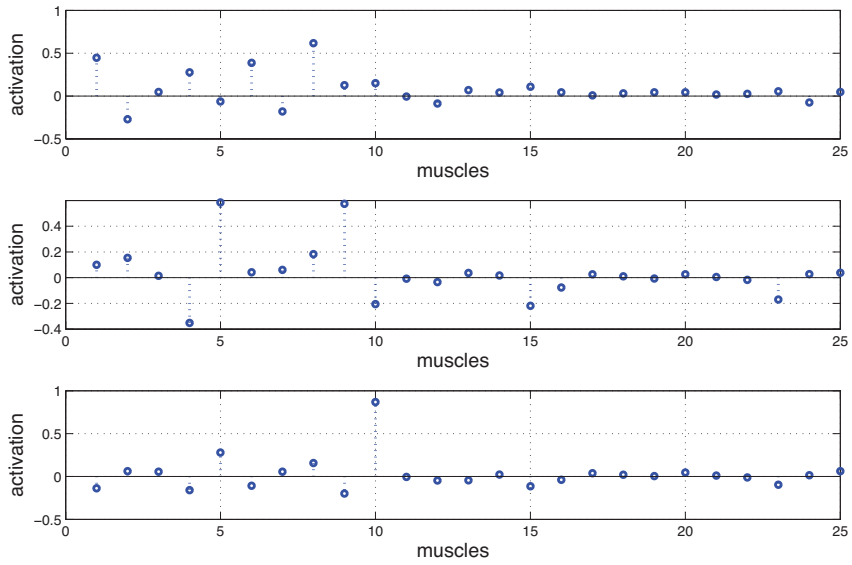

Figure 44: Torque Less Activation Modes for the pilot upper limb's muscles, in the reference configuration of the instant of time $t = 27.5$ s. The numbering of the muscles follows that of Tables 5 and 6

component of each singular vector is 1. Given a reference configuration, it is possible to augment the activation vector $\mathbf{a}$ with a small component, product of a single TLAM (or a linear combination of TLAMs) and an arbitrary, small, scalar parameter

$$\mathbf{a} = \mathbf{a}_{\min} + \sum \mathbf{v}_{i0} a_{\text{TLAM}} \tag{4.22}$$

The TLAMs can contain negative terms, and thus they cannot be added to the activation pattern in one system's configuration if they cause an activation parameter to become negative. Moreover, care has to be taken to avoid that the sum of the minimal contribution of the activation and the additional term depending on TLAMs does not exceed muscle saturation. In other words, $\mathbf{a}$ coming from the 4.22 must still satisfy $0 \leqslant a \leqslant 1$.

In practical terms, to add a compatible contribution of the TLAMs to the minimal activation, a suitable linear combination of TLAMs, such to produce only positive activation coefficients, is found by solving

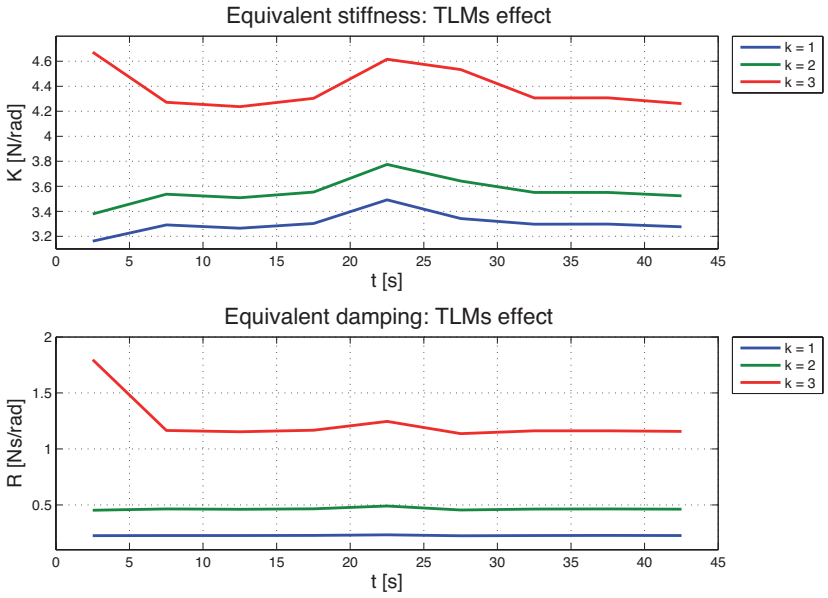

Figure 45: Torque Less Activation Modes effect on the impedance of the biomechanical system.

$$\min(J) = \|\mathbf{b}\|^2 = \frac{1}{2}\mathbf{b}^T\mathbf{b}$$

s.t.

$$[V] \cdot \mathbf{b} > 0 \qquad (\text{component} - \text{wise})$$

where $[V]$ is the matrix whose columns are the TLAMs. It is now possible to find the perturbed activation with

$$\mathbf{a} = \mathbf{a}_{min} + [V]\mathbf{b} \cdot k \tag{4.23}$$

with k being a scalar value, whose absolute value is such to not cause any muscle's saturation. It is now possible to recompute the muscular forces' derivatives needed to extract the limb impedance.

In Figure 45 the effect of the linear combination of TLAMs is showed, for different values of k. The expected increase of stiffness and damping of the limb is found, with the mean value of the equivalent stiffness increasing up to 30 %, and mean damping showing a 4 times higher mean value upon the activation of the TLAMs to the maximum values here considered.

4.3.5 *Pilot's body type effect*

To further highlight the possibilities offered by this approach: a comparison between the computed impedance of the upper limbs of two pilots, with body types different from the one used for the above simulations, has been performed.

The first pilot considered simulates an *ectomorphic* body type (i.e. possesses a smaller frame than the average): parameters of the upper limb are computed with a reference stature of 1.60 m and a body weight of 60 kg. The second pilot, conversely, possesses an *endomorphic* body type: his reference stature is 1.90 m and his reference body weight 90 kg. Parameters used for the previous simulations, collected in Table 14, will be considered to have an *mesomorphic* body type, i.e. a frame that is within the average values (or the 50% percentile) for a young adult human male.
The complete inertial parameters for the upper limb of the two pilots are collected in Table 15

Element	Properties				
	Mass [kg]	Height [cm]			
Body	70	170			
Pilot A: ectomorphic					
	Length [mm]	Mass [kg]	$J_{xx}[kgmm^2]$	$J_{yy}[kgmm^2]$	$J_{zz}[kgmm^2]$
Humerus	278	1.81	1984	13059	14133
Radius	244	0.56	296	2372	2454
Ulna	244	0.71	444	3557	3680
Hand	66	0.38	167.4	508	642
Pilot B: endomorphic					
	Length [mm]	Mass [kg]	$J_{xx}[kgmm^2]$	$J_{yy}[kgmm^2]$	$J_{zz}[kgmm^2]$
Humerus	334	2.47	3686	17112	20420
Radius	293	0.72	572	3244	3244
Ulna	293	0.95	858	4866	4866
Hand	73	0.53	251	808	890

Table 15: Parameters of pilots of different body types, used in the simulation.

Muscle lengths and peak isometric forces were scaled linearly on body weight and stature. This solution probably is to be considered an over-simplification, however, these parameters can vary greatly from an individual to another, and have to be identified specifically for a subject if his behavior has to be estimated. In a preliminary analysis's context, this method was judged to be viable.

The possible contribution of the TLAMs was disregarded in this analysis.

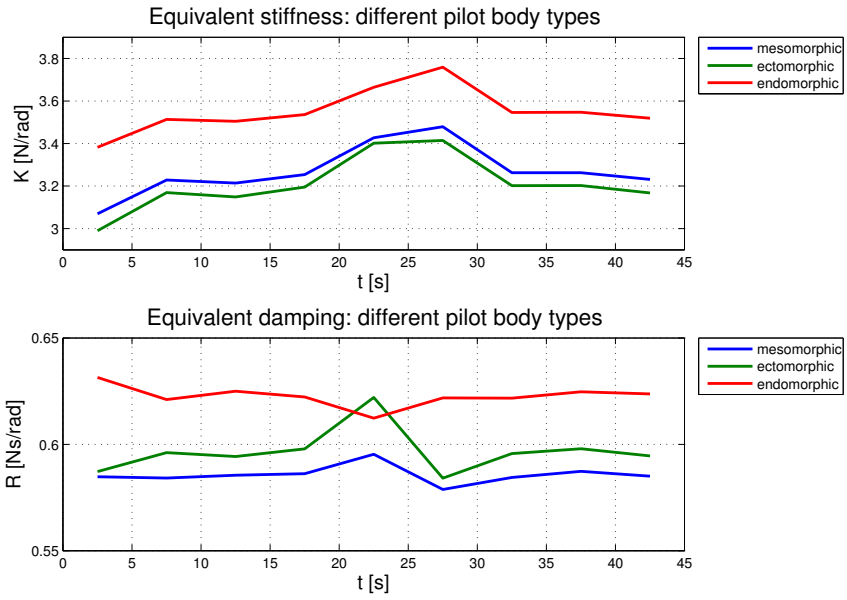

Figure 46: Impedance parameters for pilots of three different body types: the

Figure 46 shows the computed impedance parameters for the three pilots' body type considered. An appreciable difference is evidenced between the different values is observed: the mean equivalent stiffness of the endomorphic pilot is approximately 10% higher than the one of the mesomorphic one, and conversely the ectomorphic pilot shows an an average value approximately 5% less than the one relative to the mesomorphic one. The stiffness shows the same trends across the pilot body type. When the pilot performs a maneuver, the stiffness tends to raise, while it is approximately constant in the other phases.

Damping coefficients exhibit a smaller range of variability across the simulated subjects: the average value for the endomorphic pilot is 6% higher than the one attributed to the mesomorphic one, and the ecto-

morphic pilot shows a damping coefficient 3% smaller in average with respecto to the mesomorphic pilot. It can be noted that the ectomorphic pilot shows an opposite trend in damping coefficients' values in time, as his damping ratio reduces as he is in the act of performing a maneuver.

The origin of this behavior is not yet completely understood, and currently subject to verification and interpretation.

5

CONCLUSIONS AND FUTURE DEVELOPMENTS

The purpose of this work was to define a general methodology able to estimate the human upper limb's mechanical impedance in vehicle control tasks, exploiting multibody and optimization techniques, that was applicable to a wide range of cockpit geometries, pilot's geometrical, biomechanical and physiological paramers, and was able to deal with both the kinematic redundancy of the human upper limb system, and the muscular forces redundancy.

A 4 rigid bodies, 7 degrees of freedom multibody model was designed and developed specifically for this intent. It accounts for the motion of the humerus, radius, ulna and the hand, and the action of 25 muscles of the shoulder, arm and forearm, modeled as non linear viscoelastic elements that can be actuated.

The kinematics of the model has been inverted at all three levels: positions, velocities and accelerations, with a procedure capable of resolving the redundancy at the first level. The quality of the solution is then checked constantly at the successive levels, by means of subsequent constrained optimizations.

The dynamics of the system has been inverted to find joint torques needed to follow the kinematics found at the previous step, and constrained minimization of the total activation has been performed to find the associated muscular activity.
The results of the model were compared with experimental data published in literature.

An analytical approach has been developed to estimate the equivalent impedance characteristics of the upper limb in dynamical, *frozen* conditions, i.e. in conditions in which the system can be linearized without a significant loss of information.
The method has been used to identify the pilot's upper limb impedance using data collected by the research group on rotorcraft aeroservoelas-

ticity, Department of Aerospace Engineering, Politecnico di Milano at the Bibby Flight Simulation Laboratory, University of Liverpool.

The concept of Torque-Less Activation Modes, i.e. linear combinations of activation coefficients that does not produce a variation in joint torque, but capable of varying the equivalent impedance, was introduced and the possible relative importance the TLAMs activity was analyzed.

5.1 FUTURE DEVELOPMENTS

This work represents an initial attempt to deal with the issue of identifying the biomechanical impedance of the human upper limb from first principles, and it is meant to be exploratory. Thus, many further developments are possible and desirable:

1. An experimental confirmation of the results obtained by the methods proposed in the present work is needed to assess their actual performance. The related experimental campaign will have to include EMG measurements of the relevant muscle bundles of the pilot's upper limb in a controlled testing environment.

2. The actual transfer function of the pilot passive behavior with respect to known accelerations of the vehicle chassis will need to be extracted from the model, by performing numerical experiments. This process would allow to test and evaluate critically different cockpit solutions, a process that will be very useful expecially in the case of rotorcraft. It would be possible to assess the performance of a solution in terms of pilot's response to potentially hazardous dynamical conditions of new and untested (either not yet conceived or with too high associated costs) cockpit configurations.

3. The model of the upper limb will be inserted in a multibody model representing the vehicle behavior, to directly investigate the coupled pilot-vehicle dynamics

4. The upper limb impedance will be estimated not only as a total equivalent impedance of the limb itself, but as the combination of the single impedances relative to the joint coordinates, to make the adaptation of the model to different subjects easier

5. A control system, capable of activating the correct muscles to perform a given task, will need be developed to provide the ability to reproduce the impedance of the upper limb related to the neurological system response.

The actual realization of these developments is currently being planned by the research group on rotorcraft aeroelasticity at Politecnico di Milano.

BIBLIOGRAPHY

[1] J. Ambrôsio, C. Quental, B. Pilarczyk, J. Folgado, and J. Monteiro. Multibody biomechanical models of the upper limb. *IUTAM Symposium on Human Body Dynamics*, 2:4–17, 2011.

[2] A. A. Amis, D. Dowson, and V. Wright. Analysis of elbow forces due to high-speed forearm movements. *Journal of Biomechanics*, 13: 825–831, 1980.

[3] R. Barry Walden. A retrospective survey of pilot-structural coupling instabilities in naval rotorcraft. *Proceedings of 63rd AHS Annual Forum*, 2007.

[4] S. Buchanan, T., L. Delp, and J. A. Solbeck. Muscular resistance to valgous loads at the elbow. *Journal of Biomechanical Engineering*, 120:634–639, 1998.

[5] S.K. Charles and N. Hogan. Dynamics of wrist rotations. *Journal of Biomechanics*, 44:614–621, 2001.

[6] F. Cheli and E. Pennestrì. *Cinematica e Dinamica dei Sistemi Multibody*, volume 1 - Ch. 15. C.E.A., 2006.

[7] J. Cheverud, C.C. Gordon, R.A. Walker, C. Jacquish, L. Kohn, A. Moore, and N. Yamashita. 1988 anthropometric survey of us army personnel: correlation coefficients and regression equations. *Development and Engineering Center*, Part 1: Statistical Techniques, Landmark, and Mesurement Definitions, 1989.

[8] J. Cheverud, C.C. Gordon, R.A. Walker, C. Jacquish, L. Kohn, A. Moore, and N. Yamashita. 1988 anthropometric survey of us army personnel: correlation coefficients and regression equations. *Development and Engineering Center*, Part 4: Bivariate Regression Tables, 1989.

[9] S. L. Delp, A. E. Grierson, and T. S. Buchanan. Maximum isometric moments generated by the wrist muscles in flexion-extension and radial-ulnar deviation. *Journal of Biomechanics*, 29:1371–1375, 1996.

[10] O. Dieterich, J. Götz, D.B. Vu, H. Haverdings, P. Masarati, M. Pavel, M. Jump, and M. Gennaretti. Adverse rotorcraft-pilot coupling: Recent research activities in europe. *Proceeding of 34th European Rotorcraft Forum*, pages 1–13, September 16-19 2008.

[11] M. Foumani, L. Blankevoort, C. Stekelemburg, S.D. Strackee, B. Carelsen, R. Jonges, and G.J. Streekstra. The effect of tendon loading on in-vitro carpal kinematics of the wrist joint. *Journal of Biomechanics*, 43:1799–1805, 2010.

[12] A. Fumagalli, G. Gaias, and P. Masarati. A simple approach to kinematic inversion of redundant mechanisms. *Proceedings of IDETC/-CIE*, September 4-7 2007.

[13] B. A. Garner and M. G. Pandy. Musculoskeletal model of the upper limb based on the visible human male dataset. *Computer Methods in Biomechanical and Biomedical Engineering*, 3:96–126, 2001.

[14] B.A. Garner and M.G. Pandy. Estimation of musculotendon properties in the human upper limb. *Annals of Biomechanical Engineering*, 31:207–220, 2003.

[15] D. Gattamelata, E. Pezzuti, and P.P. Valentini. Accurate geometrical constraints for the computer aided modelling of the human upper limb. *Computer Aided Design*, 39:540–457, 2007.

[16] S.K. Gollapudi and D.C. Lin. Experimental determination of sarcomere force-length relationship in type-i human skeletal muscle fibers. *Journal of Biomechanics*, 42:2011–2016, 2009.

[17] T. Groot, H.J. Damveld, M. Mulder, and M.M. van Paassen. Effects of aeroelasticity on the pilot's phsychomoto behavior. *Proceedings of Atmospheric Flight Mechanics Conference and Exhibit*, August 21-24 2006.

[18] D. Hamel. Rotorcraft-pilot coupling: A critical issue for highly augmented helicopters. *AGARD*, CP-592, May 1996.

[19] H. Hashiguchi, S. Arimoto, and R. Ozawa. Control of a handwriting robot with dof redundancy based on feedback in task coordinates. *Journal of Robotics and Mechatronics*, 16, 2004.

[20] J. Hollerbach and K. Suh. Redundancy resolution of manipulators through torque optimization. *IEEE Journal of Robotics and Automation*, 3:308–316, 1987.

[21] K.R.S. Holzbaur, W.M. Murray, and S.L. Delp. A model of the upper extremity for simulating muscoloskeletal surgery and analyzing neuromuscular control. *Annals of Biomechanical Engineering*, 33: 829–840, 2005.

[22] G. Höne. Computer aided development of biomechanical pilot models. *Aerospatial Science and Technology*, 4:57–69, 2000.

[23] H. J. Huang and D. P. Ferris. Upper and lower limb muscle activation is bidirectionally and ipsilaterally coupled. *Medicine & Science in Sports & Exercise*, 41:1778–1789, 2009.

[24] Baillieul John. A constraint oriented approach to inverse problems for kinematically redundant manipulators. *IEEE International Conference on Robotics and Automation*, pages 1827–1833, March 31 - April 3 1987.

[25] M. Katayama and H. Hasuura. Optimization principle determines human arm postures and "comfort". *SICE Proceedings of Annual Conference*, pages 1000–1005, August 4-6 2003.

[26] A. Keckeméthy and A. Weinberg. An improved elasto-kinematic model of the human forearm for biofidelic medical diagnosis. *Multibody System Dynamics*, 14:1–21, 2005.

[27] D. Knudson. *Foundamentals of Biomechanics*. Springer, 2nd edition, 2007.

[28] M.A. Lemay and P.E. Crago. A dynamic model for simulating movement of the elbow, forearm and wrist. *Journal of Biomechanics*, 29:1319–1330, 1996.

[29] G.A. Lichtwark and A.M. Wilson. A modified hill muscle model that predicts muscle power output and efficiency during sinusoidal length changes. *Journal of Experimental Biology*, 208:2831–2843, 2005.

[30] L.R. Lieber and T.J. Burkholder. *Biomechanics: Principles and Applications*. CRC Press, 2008.

[31] C.C. MacAdam. Understanding and modeling the human driver. *Vehicle System Dynamics*, 40:101–134, 2003.

[32] P. Masarati, G. Quaranta, and M. Jump. Experimental and numerical helicopter pilot characterization for aeroelastic rotorcraft-pilot couplings analysis. *Proceedings of IMechE Part G: Journal of Aerospace Engineering*, (not yet published).

[33] P. Masarati, L. Quaranta, M. Lu, and M. Jump. Theoretical and experimental investigation of aeroelastic rotorcraft-pilot coupling. *to be presented at the 68th AHS Forum*, May 1-3 2012.

[34] J.R. Mayo. The involuntari participation of a human pilot in a helicopter collective control loop. *Proceedings of 15th European Rotorcraft Forum*, pages 81.001–012, 1989.

[35] R.V. Mayorga and A.K.C. Wong. A singularities avoidance method for the trajectory planning of redundant and nonredundant robot manipulators. *IEEE International Conference on Robotics and Automation*, pages 1707–1712, March 31 - April 3 1987.

[36] D.T. McRuer and H.R. Jex. A review of quasi-linear pilot models. *Human Factors in Electronics*, 8:231–249, 1967.

[37] D.T. McRuer and R.E. Smith. Pio - a historical perspective. *AGARD*, AR-335, 1995.

[38] C.P. Neu, J.J. Crisco, and S.W. Wolfe. In vivo kinematic behaviour of the radio-capitate joint during wrist flexion-extension and radioulnar deviation. *Journal of Biomechanics*, 34:1429–1438, 2001.

[39] K. Ohta, M.M. Svinin, Z.W. Luo, and S. Hosoe. On the trajectory formation of the human arm constrained by the external environment. *Proceedings of the 2003 IEEE International Conference on Robotics & Automation*, pages 2884–2891, September 14-19 2003.

[40] J. Ojeda, J. Mayo, and J. Martínez-Reina. Cost function in muscle redundancy problems: computational aspects. *Mechanics Based Design of Structures and Machines*, 39:268–284, 2011.

[41] J. C. Otis, R. F. Warren, S. I. Backus, and T.J. Santner. Torque production in the shoulder of the normal young adult male. the interaction of function, dominance, joint angle, and angular velocity. *American Journal of Sport Medicine*, 18:119–123, 1990.

[42] E. Pennestrì, R. Stefanelli, P.P. Valentini, and L. Vita. Virtual musculo-skeletal model for the biomechanical analysis of the upper limb. *Journal of Biomechanics*, 40:1350–1361, 2007.

[43] R.S. Sharp. On steering wobble oscillations of motorcicles. *Proceedings of Institution of Mechanical Engineers*, 218 Part C: Journal of Mechanical Engineering Science:1449–1456, 2004.

[44] S. Stroeve. Impedance characteristics of a neuromusculoskeletal model of the human arm i. posture control. *Biological Cybernetics*, 81:475–494, 1999.

[45] S. Sullivan, N.A. Langrana, and S.A. Sisto. Multibody computational biomechanical model of the upper body. *Proceedings of IDETC/CIE*, pages 1–6, March 31 - April 3 2005.

[46] B.M. van Bolhuis and C.C.A.M. Gielen. A comparison of models explaining muscle attivation patterns for isometric contractions. *Biological Cybernetics*, 81:149–261, 1999.

[47] M.M. van Paassen. *Biophisics in aircraft control*. PhD thesis, Delt University of Technology, 1994.

[48] J. Venrooij, D. A. Abbink, M. Mulder, M. M. van Paassen, and M. Mulder. Method to measure the relationships between biodynamic feedthrough and neuromuscular admittance. *IEEE Transactions on Systems, Man. and cybernetics — Part B*, 41:1158–1169, 2011.

[49] J. M. Wakeling and S. S. M. Lee. Modeling muscle forces: from scaled fibres to physiological task-groups. *Symposium on Human Body Dynamics proceedings*, 2:317–326, 2011.

[50] X. Wang. A behavior-based inverse kinematics algorithm to predict arm prehension postures for computer-aided ergonomic evaluation. *Journal of Biomechanics*, 5:453–460, 1999.

[51] P.L. Williams, R. Warwick, M. Dyson, and L.H. Bannister, editors. *Anatomia del Gray*, volume 1. Zanichelli, 3rd edition, 2000. In Italian.

[52] J. M. Winters and D. G. Kleweno. Effect of initial upper limb alignment on muscle contributions to isometric strenght curves. *Journal of Biomechanics*, 26:143–153, 1993.

[53] F.E. Zajac. Muscle and tendon: properties, models, scaling, and application to biomechanics and motor control. *CRC Critical Reviews in Biomedical Engineering*, 17(4):359–410, 1989.